Thesis

Kondo Effect and Topological Phenomena in Ultracold Atoms

Masaya Nakagawa

Department of Physics, Kyoto University

January, 2017

Abstract

The rapid development of laser-cooling technique in past a few decades has enabled us to cool the atomic gases down to a nano-Kelvin scale and observe numerous intriguing quantum many-body phenomena. The significant feature of this system is that the Hamiltonian of the atomic cloud is described by simple models with high accuracy and the parameters of the system can be controlled almost perfectly by using the laser or magnetic fields. By highlighting this feature, ultracold atoms are often called "quantum simulators", which reproduce the behavior of the prototypical models of condensed matter physics using table-top experiments. In addition to these features, ultracold atoms can also realize intriguing models which are hardly realized in solid-state systems. Thus one of the fascinating aspects of cold atoms is to discover new quantum many-body phenomena which are difficult to find in the ordinary models in solid state physics. Once the emergence of the new phenomena is established, it certainly helps our understanding of the quantum many-body systems and also provides a starting point to realize such new phenomena in solid-state setups.

In this thesis, we propose several setups to realize intriguing quantum many-body phenomena in ultracold atoms, and thereby investigate their properties in details. Our setups utilize the peculiar properties of cold atoms, but have a close connection with the phenomena in solid-state physics. First, we propose that ultracold atoms offer a novel platform to study the Kondo effect, which is a prototypical example of strong correlation effects in condensed matter physics. We demonstrate that intense laser application to atoms can coherently induce a novel Kondo effect in ultracold atomic gases. In this setup, a long-lived electronic excited state of alkaline-earth-like atoms play a central role, and the Kondo effect is induced by optical transitions between the electronic ground state and the excited state. One of the highlighted features here is that we can investigate the Kondo effect in nonequilibrium situations under the laser irradiation. Thus we address whether the Kondo effect survives or not in the nonequilibrium situations. We demonstrate that the optically coupled two internal states are dynamically entangled to form the Kondo singlet state, and they actually overcome the heating effect caused by the irradiation. Furthermore, it is shown that the laser-induced Kondo effect has several peculiar properties which cannot be realized in ordinary solid-state systems. For example, a lack of SU(N) symmetry in the optical coupling gives spin-selective heavy fermion liquids in which higher spin components have larger effective masses in the Kondo lattice system. We further found that the laser-induced Kondo effect has unusual spin states different from the well-known Kondo singlet. This unusual Kondo state is certainly distinct from the ordinary Kondo singlet state, if we assume the spin π-rotational symmetry around a particular axis.

Next, we show that the cold-atom realization of the Kondo lattice can host a topological phase protected by symmetries in one-dimensional optical lattice. This phase is reminiscent of the celebrated Haldane phase in spin chains, but here the charge degrees of freedom play a key role on the fate of the topological phase. We uncover the role of various symmetries on the phase diagram

of the one-dimensional Kondo lattice using bosonization methods and strong-coupling pictures of the ground states. As a result, the one-dimensional Kondo lattice provides a typical example of a crossover from a fermionic topological phase in weakly interacting regime to a bosonic topological phase in the strong coupling limit. Ultracold alkaline-earth-like atoms are therefore a promising candidate to realize the symmetry-protected topological phase with strong correlations.

Furthermore, we consider a phenomenon called topological pumping, which is a manifestation of topological nature of quantum states in transport phenomena. Although the topological pumping was theoretically predicted almost 30 years ago, it was realized only recently using the controllability of cold atoms in optical lattices. Here we focus on the fact that the topological pumping is composed of non-interacting particles and has a strong relationship with the integer quantum Hall effect. Since the quantum Hall effect has more fascinating properties in interacting systems, such as the fractional quantum Hall effect, it is natural to ask whether the connection between the topological pumping and the quantum Hall effect also holds in interacting systems. In this thesis, based on a quasi-one-dimensional limit of quantum Hall states on a thin torus, we propose a systematic scheme to construct interaction-induced topological pumping which is possibly realized in cold-atom setups.

Contents

Abstract **1**

List of publications **5**

1 Introduction and Backgrounds **6**
1 Overview of this thesis . . . 6
2 Kondo effect . . . 7
2.1 Kondo effect . . . 7
2.2 Renormalization group approach . . . 8
2.3 Slave boson theory . . . 11
2.4 Kondo lattice . . . 13
3 Topological phase . . . 16
3.1 Concept of topological phases: classification of gapped ground states . . . 16
3.2 Topological order and fractional quantum Hall effect . . . 18
3.3 One-dimensional SPT phase and Haldane phase . . . 20
3.4 Two-dimensional SPT phase and bosonic integer quantum Hall effect . . . 24
3.5 Fermionic SPT phase . . . 27
4 Ultracold Atoms . . . 30
4.1 Basics of ultracold atoms . . . 30
4.2 Realization of topological phases in ultracold atoms . . . 30
4.3 Ultracold alkaline-earth atoms . . . 32

2 Laser-Induced Kondo Effect in Ultracold Alkaline-Earth Atoms **34**
1 Setup . . . 34
2 Slave boson theory . . . 35
3 Laser-induced Kondo effect . . . 39
4 Spin-selective renormalization . . . 41
5 Effect of spin-exchange interactions . . . 42
6 Summary of this chapter . . . 45

3 Topological Phase Transition in One-Dimensional Kondo Lattice **46**
1 1D Kondo impurity . . . 46
2 Bosonization of 1D Kondo lattice . . . 48
2.1 Bosonization identities . . . 48
2.2 RG equations . . . 50
3 Phase diagram . . . 51

3.1 Kondo insulator . . . 52
3.2 Laser-induced Kondo insulator . . . 54
3.3 Topological phase . . . 54
3.4 Néel order . . . 55
4 Symmetry protection . . . 55
4.1 SPT phase in one dimension: a bosonization viewpoint . . . 55
4.2 Protection by spin π rotation symmetries around the x or y axis . . . 56
4.3 Protection by spatial inversion symmetry: role of the charge degrees of freedom 58
5 Fate of edge states and experimental detection . . . 60
6 Summary of this chapter . . . 61

4 Topological Pumping in Interacting Systems 62
1 Introduction . . . 62
2 Topological pumping as flux insertion through a thin torus . . . 63
3 Fractional charge pumping in the thin-torus limit of FQH states . . . 64
4 Thin-torus limit of the bosonic integer quantum Hall state . . . 65
5 Off-diagonal topological pumping in the thin-torus limit . . . 69
6 Summary of this chapter . . . 74

5 Conclusion 75

Bibliography 77

Acknowledgment 90

List of publications

Papers related to the thesis

1. Masaya Nakagawa and Norio Kawakami
Laser-Induced Kondo Effect in Ultracold Alkaline-Earth Fermions
Phys. Rev. Lett. **115**, 165303 (2015).

2. Masaya Nakagawa and Norio Kawakami
Symmetry-protected topological phase transition in one-dimensional Kondo lattice and its realization with ultracold atoms
arXiv: 1612.09028. (submitted)

3. Masaya Nakagawa and Shunsuke Furukawa
Bosonic integer quantum Hall effect as topological pumping
arXiv: 1701.01127. (submitted)

Papers not included in the thesis

4. Masaya Nakagawa and Norio Kawakami
Nonequilibrium topological phase transitions in two-dimensional optical lattices
Phys. Rev. A **89**, 013627 (2014).

5. Masaya Nakagawa and Norio Kawakami
Dynamically Induced Topological Properties in Two-Dimensional Optical Lattices
JPS Conf. Proc. **3**, 016003 (2014).

6. Kazuaki Takasan, Masaya Nakagawa, and Norio Kawakami
Laser-induced phase transitions of topological Kondo insulators
Physics Procedia **75**, 447 (2015).

Chapter 1

Introduction and Backgrounds

1 Overview of this thesis

First of all, we explain the organization of this thesis. This thesis consists of five chapters, and Chaps. 2, 3, and 4 present our results. In this chapter, we describe the theoretical and experimental backgrounds of the topics addressed in this thesis. We focus on two aspects of quantum many-body systems: the Kondo effect and topological phases. In Sec. 2, we explain the basics of the Kondo effect focusing on several methods used in this thesis. In Sec. 3, we review the concept of topological phases and present several examples. Among them, the Haldane phase in Sec. 3.3 plays an important role in Chaps. 3 and 4. Also, the fractional quantum Hall effect in Sec. 3.2 and the bosonic integer quantum Hall effect in Sec. 3.4 are focused on in Chap. 4. Section 3.5 is a description of fermionic topological phases related to Chap. 3. After reviewing these theoretical backgrounds, Sec. 4 presents the basic properties of ultracold atoms as an experimental platform. In Sec. 4.1, we briefly review the basics of cold atoms. Next, in Sec. 4.2, we describe a current status of the realization of topological phases in cold atoms. Sec. 4.3 is devoted to explanation of the specific properties of alkaline-earth-like atoms (AEA). We utilize the properties of AEA to realize the Kondo effect in Chaps. 2 and 3.

In Chap. 2, we propose that optical transitions between internal states of AEA enable us to realize the Kondo effect using laser irradiation. The analysis is performed using the slave boson theory explained in Sec. 2.3 of this chapter. We show that the optical coupling dynamically entangles localized spins with the atomic cloud due to the Kondo effect, and thereby realizes a heavy-fermion liquid. A possible drawback in this scheme is the heating effect caused by the application of the laser. Here we find that the dynamically induced heavy-fermion liquid indeed persists under the irradiation, even if there is a substantial heating effect. Furthermore, we demonstrate that the laser-induced Kondo has several peculiar properties which are different from the ordinary Kondo effect, focusing on the laser-spin coupling and the spin state of the Kondo singlet.

In Chap. 3, we continue the analysis of the Kondo lattice in AEA, and then focus on its topological properties when the system is confined in one dimension (1D). Based on a bosonization method and renormalization group analysis, it is demonstrated that the cold-atom realization of the Kondo lattice shows a topological phase and an associated quantum phase transition. Moreover, we show that the laser-induced Kondo state is certainly distinct from the ordinary Kondo state if we assume the spin π rotation symmetry around the x or y axis. Finally, we elucidate how the charge degrees of freedom of the Kondo lattice change the nature of the topological phase from a weak coupling

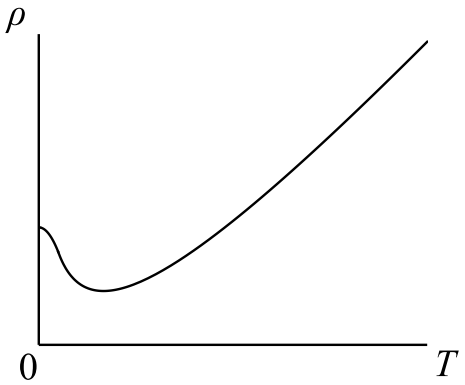

Figure 1.1: Typical temperature dependence of electrical resistivity ρ in the Kondo effect. The resistivity has a minimum at a low temperature and is finally saturated to a finite value of residual resistivity.

regime to a strong coupling limit. Since it approaches the Haldane phase explained in Sec, 3.3 of this chapter at the strong coupling limit, the Kondo lattice clearly exemplifies a crossover from a fermionic SPT phase to a bosonic SPT phase.

In Chap. 4, we move to a somewhat different phenomenon called topological pumping. After introducing the concept of topological pumping, we explain that this phenomenon is tightly connected to the integer quantum Hall effect. In this study, we propose a systematic scheme to construct the topological pumping in interacting systems from two-dimensional quantum Hall states created by strong interactions. A key idea here is a quasi-one-dimensional limit of quantum Hall states on a thin torus. As a concrete example, we first consider the case of the fractional quantum Hall effect and corresponding topological pumping. Next, we focus on an interaction-induced topological pump which corresponds to the bosonic integer quantum Hall state.

Finally, we conclude this thesis in Chap. 5.

2 Kondo effect

2.1 Kondo effect

Electrical resistivity is a fundamental physical quantity in metals. There are several origins of the electrical resistivity, such as impurities, electron-phonon interactions, and electron-electron interactions. Since the scattering rates by various interactions are suppressed at low temperatures due to the formation of Fermi surface, electrical resistivity usually decreases as the temperature is lowered. However, in 1930s, it was experimentally discovered that some alloys containing magnetic elements show *increase* of resistivity at low temperatures (Fig. 1.1). A breakthrough for understanding this behavior was made by Jun Kondo [1] in 1964, and thus this phenomenon is called Kondo effect (for reviews and textbooks, see [2, 3, 4]).

One of essential ingredients for the mechanism of the Kondo effect is magnetic impurities in metals. Kondo [1] showed that the scattering amplitude between conduction electrons and a magnetic impurity is strongly enhanced at low temperatures, when the interaction between them is an antiferromagnetic exchange interaction. This enhancement arises from the existence of Fermi surface of the conduction electrons and a quantum nature of the impurity spin. However, the calculation by

Kondo was based on perturbation theory in terms of the exchange coupling and included unphysical divergence of the resistivity. To overcome the difficulty, many studies had been performed and the low-temperature properties of the Kondo effect had been gradually uncovered. Yosida [5] proposed that the ground state of the Kondo effect is a many-body spin-singlet bound state between the conduction electrons and the impurity. Anderson *et al.* [6, 7] performed a renormalization group calculation for Kondo's model and demonstrated that the antiferromagnetic interaction is enhanced and finally diverges at low temperatures. Based on the Anderson's result, Nozières [8] constructed a phenomenological local Fermi-liquid theory for the Kondo effect, and this picture was also supported by perturbative expansion in terms of Coulomb interactions at the impurity site [9, 10, 11, 12]. Finally, the low-temperature behavior of the Kondo effect was solved by Wilson's numerical renormalization group [13] and exact solutions using Bethe ansatz [14, 15, 16, 17, 18, 19]. After some years, the Kondo effect and its multichannel generalizations were also solved by using techniques of boundary conformal field theory [20, 21, 22, 23].

From these tremendous theoretical efforts and developments, the basic properties of the original Kondo problem are now well understood. At high temperatures, the magnetic impurity is disturbed by thermal fluctuations and is almost decoupled from the conduction electrons. In this region, the resistivity decreases with lowering the temperature as ordinary metals. However, when the temperature approaches a characteristic temperature scale, called the Kondo temperature, the impurity gradually starts to interact with the conduction electrons, and the interaction is more enhanced at lower temperatures. This leads to the increase of resistivity. Corresponding to the enhancement of the antiferromagnetic interaction, the impurity spin is gradually screened by the conduction electrons and the many-body spin-singlet bound state (Kondo-Yosida singlet) is formed. The formation of the singlet bound state means that the spin of the magnetic impurity completely disappears. As a result, when the temperature is sufficiently lower than the Kondo temperature, the system is described by the local Fermi liquid, in which the conduction electrons interacting with a nonmagnetic impurity only shows finite residual resistivity at zero temperature instead of the divergence.

In the following subsections, we describe theoretical details of the Kondo effect, focusing on several methods which will be used in later chapters.

2.2 Renormalization group approach

To capture the essence of the Kondo effect, let us consider a single magnetic impurity inserted in a metal. This situation is described by the following model:

$$H = \sum_{\boldsymbol{k},\sigma} \varepsilon(\boldsymbol{k}) c^\dagger_{\boldsymbol{k}\sigma} c_{\boldsymbol{k}\sigma} + \sum_{\sigma} \varepsilon_f f^\dagger_\sigma f_\sigma + U n_{f\uparrow} n_{f\downarrow} + \sum_{\boldsymbol{k},\sigma} (V f^\dagger_\sigma c_{\boldsymbol{k}\sigma} + \text{h.c.}), \tag{1.2.1}$$

which is called Anderson model [24]. $c_{\boldsymbol{k}\sigma}$ and f_σ denote the annihilation operators of conduction electrons and electrons at the impurity site, respectively. $n_{f\sigma} = f^\dagger_\sigma f_\sigma$ is the number of electrons at the impurity site. $\varepsilon(\boldsymbol{k})$ is the three-dimensional band structure of the conduction electrons. For simplicity, the interactions between conduction electrons are neglected. The second term is the energy level of the impurity. The third term is the most important term which means that the electrons feel strong Coulomb interaction $U > 0$ at the impurity site. The last term expresses a hybridization between the itinerant orbital and the localized f-orbital. The hybridization mixes the conduction electrons with the impurity state, leading to a virtual bound state at the impurity site.

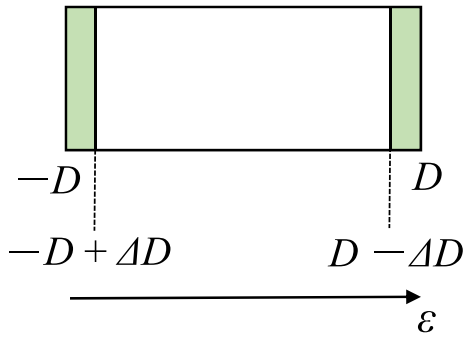

Figure 1.2: Schematic picture of the Anderson's poor-man's scaling method. The shaded regions mean the high-energy degrees of freedom (measured from the Fermi energy located at $\varepsilon = 0$) with the energy window ΔD. Here $2D$ denotes the bandwidth of conduction electrons. By projecting out the high-energy degrees of freedom, we can obtain a low-energy effective theory composed of electrons at $-D + \Delta D \leq \varepsilon \leq D - \Delta D$.

Due to the presence of the Coulomb interaction at the impurity, the Anderson model (1.2.1) cannot be reduced to free electrons and therefore cannot be easily solved. At this stage, let us extract essential ingredients of the model and derive a low-energy effective theory using the Schrieffer-Wolff transformation [25]. We assume that a "Kondo limit" $\varepsilon_f \ll \mu \ll \varepsilon_f + U$ is achieved. In this case, the occupation number of the impurity site is frozen to unity. Then the low-energy effective Hamiltonian restricted in $n_{f\uparrow} + n_{f\downarrow} = 1$ is

$$H = \sum_{\boldsymbol{k},\sigma} \varepsilon(\boldsymbol{k}) c^\dagger_{\boldsymbol{k}\sigma} c_{\boldsymbol{k}\sigma} - J \boldsymbol{S}_{c0} \cdot \boldsymbol{S}_f \tag{1.2.2}$$

where $\boldsymbol{S}_{c0} = \frac{1}{2N_s} \sum_{\boldsymbol{k},\boldsymbol{k}',\sigma,\sigma'} c^\dagger_{\boldsymbol{k}\sigma} \boldsymbol{\sigma}_{\sigma\sigma'} c_{\boldsymbol{k}'\sigma'}$, $\boldsymbol{S}_f = \frac{1}{2} \sum_{\sigma,\sigma'} f^\dagger_\sigma \boldsymbol{\sigma}_{\sigma\sigma'} f_{\sigma'}$ and $J = -2|V|^2 (\frac{1}{|\varepsilon_f - \mu|} + \frac{1}{\varepsilon_f + \mu + U}) < 0$. Here N_s is the number of sites of the system and $\boldsymbol{\sigma}$ is the three-component Pauli matrices. This model is called the *s-d* model or Kondo model. In the Kondo limit, the charge degree of freedom at the impurity site is completely frozen and the impurity behaves as a quantum spin. The second term in Eq. (1.2.2) leads to an antiferromagnetic exchange interaction between the conduction electrons and the impurity spin. The mechanism of the antiferromagnetic interaction is similar to that of the Hubbard model. The strong Coulomb repulsion and the virtual hopping between itinerant orbitals and the f-orbitals decrease the energies of antiferromagnetic configurations.

Let us extract the low-energy behavior of the model (1.2.2) employing Anderson's poor-man's scaling method [7]. We consider the T-matrix at energy ω defined by

$$T(\omega) = V + V \frac{1}{\omega - H_0} T(\omega). \tag{1.2.3}$$

Here we have divided the Kondo Hamiltonian (1.2.2) into $H = H_0 + V$, where

$$H_0 = \sum_{\boldsymbol{k},\sigma} \varepsilon(\boldsymbol{k}) c^\dagger_{\boldsymbol{k}\sigma} c_{\boldsymbol{k}\sigma}, \tag{1.2.4}$$

$$V = -\frac{J_\perp}{2N_s} \sum_{\boldsymbol{k},\boldsymbol{k}'} (c^\dagger_{\boldsymbol{k}\uparrow} c_{\boldsymbol{k}'\downarrow} S^-_f + c^\dagger_{\boldsymbol{k}\downarrow} c_{\boldsymbol{k}'\uparrow} S^+_f) - \frac{J_z}{2N_s} \sum_{\boldsymbol{k},\boldsymbol{k}'} (c^\dagger_{\boldsymbol{k}\uparrow} c_{\boldsymbol{k}'\uparrow} - c^\dagger_{\boldsymbol{k}\downarrow} c_{\boldsymbol{k}'\downarrow}) S^z_f. \tag{1.2.5}$$

In the above expression, we generalize the Kondo exchange couping to the anisotropic case. Then, we integrate out the high-energy degrees of freedom within $-D \le \varepsilon(\boldsymbol{k}) \le -D+\Delta D$ and $D-\Delta D \le \varepsilon \le D$, where $\pm D$ denotes the band edges of the conduction electrons (Fig. 1.2). The heart of the Anderson's poor-man's scaling method is to examine the change of the T-matrix when we project out the high-energy electrons and thereby construct an effective low-energy theory. When we denote the projection onto the Hilbert space of the high-energy window with width ΔD as $\mathcal{P}_{\Delta D}$, the T-matrix is written as

$$\begin{aligned}
T(\omega) =& V + V\mathcal{P}_{\Delta D}\frac{1}{\omega - H_0}T(\omega) + V(1-\mathcal{P}_{\Delta D})\frac{1}{\omega - H_0}T(\omega) \\
=& V + \mathcal{P}_{\Delta D}\frac{1}{\omega - H_0}(V + V\frac{1}{\omega - H_0}T(\omega)) + V(1-\mathcal{P}_{\Delta D})\frac{1}{\omega - H_0}T(\omega) \\
=& V + \mathcal{P}_{\Delta D}\frac{1}{\omega - H_0}V + (V + V\mathcal{P}_{\Delta D}\frac{1}{\omega - H_0}V)(1-\mathcal{P}_{\Delta D})\frac{1}{\omega - H_0}T(\omega) \\
&+ V\mathcal{P}_{\Delta D}\frac{1}{\omega - H_0}V\mathcal{P}_{\Delta D}\frac{1}{\omega - H_0}T(\omega) \\
=& V' + V'(1-\mathcal{P}_{\Delta D})\frac{1}{\omega - H_0}T(\omega) + \mathcal{O}((\Delta D)^2)
\end{aligned} \tag{1.2.6}$$

where we define

$$\begin{aligned}
V' &\equiv V + V\mathcal{P}_{\Delta D}\frac{1}{\omega - H_0}V \\
&= V + \Delta V.
\end{aligned} \tag{1.2.7}$$

From these equations, we find that integrating out the high-energy degrees of freedom is equivalent to changing the Kondo interaction from V to $V + \Delta V$. The change of the interaction can be calculated as

$$\Delta V = \Delta V_1 + \Delta V_2, \tag{1.2.8}$$

$$\begin{aligned}
\Delta V_1 = \frac{1}{4N_s}\sum_{\boldsymbol{k}_1,\sigma_1}{}'\sum_{\boldsymbol{k}_2,\sigma_2}{}'\frac{\rho_0\Delta D}{\omega - D}\Big[c^\dagger_{\boldsymbol{k}_1\sigma_1}c_{\boldsymbol{k}_2\sigma_2}\Big\{\delta_{\sigma_1\sigma_2}(\frac{J_z^2}{4}+\frac{J_\perp^2}{2}) \\
- J_\perp^2\sigma^z_{\sigma_1\sigma_2}S^z_f - J_\perp J_z(\sigma^-_{\sigma_1\sigma_2}S^+_f + \sigma^+_{\sigma_1\sigma_2}S^-_f)\Big\}\Big],
\end{aligned} \tag{1.2.9}$$

$$\begin{aligned}
\Delta V_2 = \frac{1}{4N_s}\sum_{\boldsymbol{k}_1,\sigma_1}{}'\sum_{\boldsymbol{k}_2,\sigma_2}{}'\frac{\rho_0\Delta D}{\omega - D}\Big[c^\dagger_{\boldsymbol{k}_1\sigma_1}c_{\boldsymbol{k}_2\sigma_2}\Big\{\delta_{\sigma_1\sigma_2}(\frac{J_z^2}{4}+\frac{J_\perp^2}{2}) \\
+ J_\perp^2\sigma^z_{\sigma_1\sigma_2}S^z_f + J_\perp J_z(\sigma^-_{\sigma_1\sigma_2}S^+_f + \sigma^+_{\sigma_1\sigma_2}S^-_f)\Big\}\Big].
\end{aligned} \tag{1.2.10}$$

Each component ΔV_1 and ΔV_2 corresponds to the process (a) and (b) in Fig. 1.3, respectively. ρ_0 denotes the density of states at Fermi energy. The summation $\sum'$ means a restriction to $-D+\Delta D \le \varepsilon(\boldsymbol{k}) \le D - \Delta D$. Then, we obtain

$$\Delta V = \Delta V_0 + \frac{\rho_0\Delta D}{\omega - D}\frac{1}{2N_s}\sum_{\boldsymbol{k},\boldsymbol{k}',\sigma,\sigma'}c^\dagger_{\boldsymbol{k}\sigma}c_{\boldsymbol{k}'\sigma'}\Big\{-J_\perp^2\sigma^z_{\sigma\sigma'}S^z_f - J_\perp J_z(\sigma^-_{\sigma\sigma'}S^+_f + \sigma^+_{\sigma\sigma'}S^-_f)\Big\}. \tag{1.2.11}$$

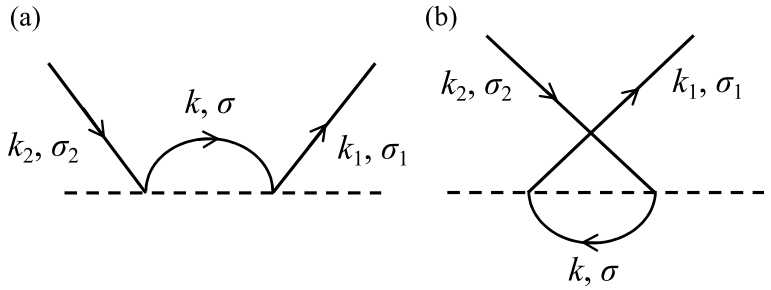

Figure 1.3: Feynman diagrams which correspond to the effective interactions ΔV_1 (Eq. (1.2.9)) and ΔV_2 (Eq. (1.2.10)). The solid lines mean the trajectories of the conduction electrons with the momentum $\boldsymbol{k}$ and the spin σ, and the broken lines mean those of the impurity. The time flows from the left to the right of the diagram. In the intermediate states, the electrons belong to the high-energy Hilbert space. Each diagram (a) and (b) expresses the process corresponding ΔV_1 and ΔV_2, respectively.

In Eq. (1.2.11), the second, third, and forth terms have the same form of the original interaction (1.2.5), while ΔV_0 denotes a spin-independent potential scattering. Hence, the change of the exchange interaction is summarized into the following differential equations by taking $\Delta D \to 0$:

$$\frac{dJ_\perp}{dD} = -\frac{\rho_0}{\omega - D} J_\perp J_z, \tag{1.2.12}$$

$$\frac{dJ_z}{dD} = -\frac{\rho_0}{\omega - D} J_\perp^2, \tag{1.2.13}$$

which is the renormalization group equations for the Kondo model. Particularly, when we set $\omega = 0$ and $J_\perp = J_z = J$, the above equations are reduced to

$$\frac{dJ}{dD} = \frac{\rho_0}{D} J^2, \tag{1.2.14}$$

and the solution is

$$\frac{1}{J} = \frac{1}{J_0} - \rho_0 \log \frac{D}{D_0} \tag{1.2.15}$$

where we set the initial value $J(D_0) = J_0$. Thus, if the interaction is antiferromagnetic $J_0 < 0$, the effective interaction J grows as lowering the energy scale D, and finally diverges at $D = T_K$ with

$$T_K = D_0 \exp\Big[\frac{1}{\rho_0 J_0}\Big]. \tag{1.2.16}$$

The energy scale (1.2.16) is called the Kondo temperature. As inferred from the expression of T_K, the Kondo effect is a nonperturbative effect in terms of the exchange coupling J_0. This situation is similar to that of the BCS theory of superconductivity. Although this perturbative calculation cannot be applicable at $D \lesssim T_K$, we can expect that the low-energy fixed point of the Kondo effect is located at $J = -\infty$ when the bare exchange coupling is antiferromagnetic $J_0 < 0$.

2.3 Slave boson theory

The Kondo effect is essentially a many-body phenomenon. Thus the standard mean-field theory by Hartree-Fock approximation cannot describe the Kondo effect and only gives rise to a shift of the

impurity level. However, a useful viewpoint is obtained from a kind of mean field theory by focusing on a more subtle saddle point. The mean-field description of the Kondo effect was developed by Read, Newns [26], and Coleman [27, 28]. Let us consider a generalized version of the Anderson model (SU(N) Anderson model):

$$H = \sum_{\boldsymbol{k}} \sum_{\sigma=1}^{N} \varepsilon(\boldsymbol{k}) c^{\dagger}_{\boldsymbol{k}\sigma} c_{\boldsymbol{k}\sigma} + \sum_{\sigma=1}^{N} \varepsilon_f f^{\dagger}_{\sigma} f_{\sigma} + U \sum_{\sigma<\sigma'} n_{f\sigma} n_{f\sigma'} + \sum_{\boldsymbol{k}} \sum_{\sigma=1}^{N} (V f^{\dagger}_{\sigma} c_{\boldsymbol{k}\sigma} + \text{h.c.}). \tag{1.2.17}$$

In the above model, we have generalized the number of spin components to N. The mean-field theory starts from taking a strong correlation limit $U \to \infty$. In this case, the occupation number at the impurity site is less than one, since the double occupancy is forbidden. Based on this property, we can split the f-fermion operator by introducing a "slave boson" b, as

$$f^{\dagger}_{\sigma} = \tilde{f}^{\dagger}_{\sigma} b. \tag{1.2.18}$$

The new fermion operator $\tilde{f}_{\sigma}$ satisfies the standard anticommuation relation. Furthermore, for the slave boson and the new fermion, a constraint

$$b^{\dagger} b + \sum_{\sigma=1}^{N} \tilde{f}^{\dagger}_{\sigma} \tilde{f}_{\sigma} = 1. \tag{1.2.19}$$

is imposed. One can check the left-hand side and the right-hand side of Eq. (1.2.18) give the same matrix elements under the constraint. Intuitively, the slave-boson operator $b^{\dagger}$ creates a "hole" at the impurity site. By replacing the f-fermion with the composite object (1.2.18), we obtain

$$H = \sum_{\boldsymbol{k}} \sum_{\sigma=1}^{N} \varepsilon(\boldsymbol{k}) c^{\dagger}_{\boldsymbol{k}\sigma} c_{\boldsymbol{k}\sigma} + \sum_{\sigma=1}^{N} \varepsilon_f \tilde{f}^{\dagger}_{\sigma} \tilde{f}_{\sigma} + \sum_{\boldsymbol{k}} \sum_{\sigma=1}^{N} (V b \tilde{f}^{\dagger}_{\sigma} c_{\boldsymbol{k}\sigma} + \text{h.c.}). \tag{1.2.20}$$

To proceed, let us express the partition function of the system using a path-integral formalism. The partition function is

$$Z = \int \mathcal{D}c \mathcal{D}\tilde{f} \mathcal{D}b \mathcal{D}\lambda e^{-S}, \tag{1.2.21}$$

where

$$\begin{aligned} S = \int_0^{\beta} d\tau \sum_{\boldsymbol{k}} \sum_{\sigma=1}^{N} c^{\dagger}_{\boldsymbol{k}\sigma} (\partial_{\tau} - \varepsilon(\boldsymbol{k})) c_{\boldsymbol{k}\sigma} + \sum_{\sigma=1}^{N} \tilde{f}^{\dagger}_{\sigma} (\partial_{\tau} - \varepsilon_f) \tilde{f}_{\sigma} + b^{\dagger} \partial_{\tau} b \\ - \sum_{\boldsymbol{k}} \sum_{\sigma=1}^{N} (V b \tilde{f}^{\dagger}_{\sigma} c_{\boldsymbol{k}\sigma} + \text{h.c.}) - \lambda (b^{\dagger} b + \sum_{\sigma=1}^{N} \tilde{f}^{\dagger}_{\sigma} \tilde{f}_{\sigma} - 1). \end{aligned} \tag{1.2.22}$$

τ is the imaginary time and β is the inverse temperature. In the path-integral representation, we have introduced a bosonic field λ which stands for a Langrange multiplier of the constraint (1.2.19) by using an identity

$$\delta\Big(b^{\dagger} b + \sum_{\sigma=1}^{N} \tilde{f}^{\dagger}_{\sigma} \tilde{f}_{\sigma} - 1\Big) = \int_{-\infty}^{\infty} d\lambda \exp\Big[-i\lambda (b^{\dagger} b + \sum_{\sigma=1}^{N} \tilde{f}^{\dagger}_{\sigma} \tilde{f}_{\sigma} - 1)\Big] \tag{1.2.23}$$

with redefinition of λ by $i\lambda$. Next, we formally integrate out fermions and define an effective action containing only bosons b, λ:

$$\begin{aligned} Z &\equiv \int \mathcal{D}b\mathcal{D}\lambda e^{-S_{\text{eff}}} \\ &= \int \mathcal{D}b\mathcal{D}\lambda e^{-N\tilde{S}_{\text{eff}}} \end{aligned} \tag{1.2.24}$$

In the second line, we have extracted an overall factor N, since the action (1.2.22) is proportional to N. Then, the partition function is evaluated by a saddle point of the effective action in the $N \to \infty$ limit. The saddle point is obtained by a condition

$$\frac{\delta S_{\text{eff}}}{\delta b(\tau)} = \frac{\delta S_{\text{eff}}}{\delta \lambda(\tau)} = 0. \tag{1.2.25}$$

Since $S_{\text{eff}} = -\ln \int \mathcal{D}c\mathcal{D}\tilde{f}e^{-S}$, the saddle-point condition can be rewritten as

$$\frac{\delta S_{\text{eff}}}{\delta b(\tau)} = \Big\langle \frac{\delta S}{\delta b(\tau)} \Big\rangle = 0, \tag{1.2.26}$$

$$\frac{\delta S_{\text{eff}}}{\delta \lambda(\tau)} = \Big\langle \frac{\delta S}{\delta \lambda(\tau)} \Big\rangle = 0, \tag{1.2.27}$$

where $\langle \cdots \rangle \equiv \Big(\int \mathcal{D}c\mathcal{D}\tilde{f}[\cdots]e^{-S}\Big) / \Big(\int \mathcal{D}c\mathcal{D}\tilde{f}e^{-S}\Big)$ denotes an expectation value with fixed b and λ. Hence, we obtain

$$-\lambda b - V^* \sum_{\boldsymbol{k},\sigma} \langle c^\dagger_{\boldsymbol{k}\sigma}(\tau)\tilde{f}_\sigma(\tau)\rangle = 0, \tag{1.2.28}$$

$$b^\dagger b + \sum_\sigma \langle \tilde{f}^\dagger_\sigma(\tau)\tilde{f}_\sigma(\tau)\rangle - 1 = 0. \tag{1.2.29}$$

We note that the expectation values are evaluated by a Hamiltonian

$$H_{\text{MF}} = \sum_{\boldsymbol{k}} \sum_{\sigma=1}^{N} \varepsilon(\boldsymbol{k}) c^\dagger_{\boldsymbol{k}\sigma} c_{\boldsymbol{k}\sigma} + \sum_{\sigma=1}^{N} \tilde{\varepsilon}_f \tilde{f}^\dagger_\sigma \tilde{f}_\sigma + \sum_{\boldsymbol{k}} \sum_{\sigma=1}^{N} (\tilde{V} \tilde{f}^\dagger_\sigma c_{\boldsymbol{k}\sigma} + \text{h.c.}), \tag{1.2.30}$$

where $\tilde{V} \equiv bV, \tilde{\varepsilon}_f \equiv \varepsilon_f + \lambda$ are c-numbers, not operators. Notably, Eq. (1.2.30) is equivalent to the Anderson model (1.2.17) with $U = 0$. Thus the saddle-point condition is nothing but a mean field theory by replacing the slave boson and the Lagrange multiplier with their expectation values. The mean values of b, λ effectively renormalize the hybridization strength and the f-level energy. Thus, the slave boson theory describes the local Fermi liquid, which is the low-temperature state of the Kondo effect.

2.4 Kondo lattice

In the Kondo effect discussed so far, the f-electron is assumed to be a single impurity. In materials composed of rare-earth elements, or rare-earth alloys, the f-orbitals are periodically aligned. In this

case the f-electrons are no longer impurities but participate in the band structure of the system. This situation is described by a model

$$H = \sum_{\boldsymbol{k},\sigma} \varepsilon(\boldsymbol{k}) c^\dagger_{\boldsymbol{k}\sigma} c_{\boldsymbol{k}\sigma} + \sum_{j,\sigma} \varepsilon_f f^\dagger_{j\sigma} f_{j\sigma} + U \sum_j n_{fj\uparrow} n_{fj\downarrow} + \sum_{j,\sigma} (V f^\dagger_{j\sigma} c_{j\sigma} + \text{h.c.}), \tag{1.2.31}$$

which is a gereralization of the impurity model (1.2.1) and called periodic Anderson (or Anderson lattice) model. At low energies, the model (1.2.31) is reduced to Kondo lattice model

$$H = \sum_{\boldsymbol{k},\sigma} \varepsilon(\boldsymbol{k}) c^\dagger_{\boldsymbol{k}\sigma} c_{\boldsymbol{k}\sigma} - J \sum_j \boldsymbol{S}_{cj} \cdot \boldsymbol{S}_{fj} \tag{1.2.32}$$

using the Schrieffer-Wolff transformation. In the Anderson (or Kondo) lattice systems, the Kondo effect takes place at every lattice site (Fig. 1.4). The periodically aligned Kondo singlets form a coherent band structure, and the effective mass of electrons is highly renormalized due to the strong correlation. The enhancement factor of the effective mass m^*/m_0 is typically from 100 to 1000. Thus these systems are often called "heavy fermion" systems.

Let us illustrate the physics of the Kondo lattice using the slave boson theory. By taking $U \to \infty$ limit in Eq. (1.2.31), we can introduce the slave boson in a similar way of the impurity case, as

$$f^\dagger_{j\sigma} = \tilde{f}^\dagger_{j\sigma} b_j \tag{1.2.33}$$

with a constraint $b^\dagger_j b_j + \sum_\sigma f^\dagger_{j\sigma} f_{j\sigma} = 1$ at every lattice site. The mean-field Hamiltonian is

$$H = \sum_{\boldsymbol{k},\sigma} \varepsilon(\boldsymbol{k}) c^\dagger_{\boldsymbol{k}\sigma} c_{\boldsymbol{k}\sigma} + \sum_{j,\sigma} \tilde{\varepsilon}_f \tilde{f}^\dagger_{j\sigma} \tilde{f}_{j\sigma} + \sum_{j,\sigma} (\tilde{V} \tilde{f}^\dagger_{j\sigma} c_{j\sigma} + \text{h.c.}), \tag{1.2.34}$$

with $\tilde{V} \equiv bV$ and $\tilde{\varepsilon}_f \equiv \varepsilon_f + \lambda$ where spatially uniform expectation values of b and λ are assumed. By diagonalizing the mean-field Hamiltonian (1.2.34), we obtain quasi-particle band structures under the Kondo effect as

$$\varepsilon_\pm(\boldsymbol{k}) = \frac{\varepsilon(\boldsymbol{k}) - \tilde{\varepsilon}_f \pm \sqrt{(\varepsilon(\boldsymbol{k}) - \tilde{\varepsilon}_f)^2 + 4|\tilde{V}|^2}}{2}. \tag{1.2.35}$$

Each quasi-particle band is doubly degenerate due to the spin degrees of freedom. The band structure is illustrated in Fig. 1.5. The broad conduction-electron band admixes with the flat f-electron band and thereby realizes a hybridized band with nearly-flat dispersion near the Fermi energy. The band dispersion is strongly renormalized from the $U = 0$ model due to the expectation value of the slave boson, and thus the effective mass near the Fermi energy is largely enhanced realizing the heavy fermion state. Reflecting the emergence of Kondo effect with $b \neq 0$, there is a Kondo gap between the upper and lower bands. The value of the Kondo gap is mostly determined by the renormalized hybridization $\tilde{V}$, whose strength signifies the Kondo temperature.

An important difference between the impurity Kondo effect and the Kondo lattice is that there is an effective magnetic interaction between the f-electrons mediated by the conduction electrons, known as Ruderman-Kittel-Kasuya-Yosida (RKKY) interaction [29, 30, 31]. This interaction tends to cause magnetic order of localized spins. Since the RKKY interaction scales as J^2 while the Kondo temperature scales as $\exp[1/\rho_0 J]$, in the small J region the RKKY interaction dominates leading to magnetic order, and in the large J region the Kondo effect manifests itself with a nonmagnetic

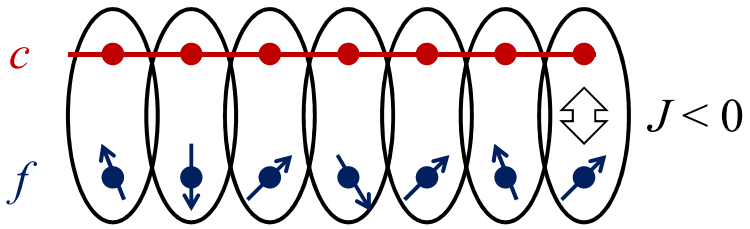

Figure 1.4: Schematic picture of the Kondo lattice model. The conduction electrons (red balls in the figure) interact with the periodically aligned localized spins of f-electrons (blue balls in the figure) with an antiferromagnetic coupling J. In this case, the Kondo singlet is formed at every lattice site, and thereby the heavy-fermion state is formed.

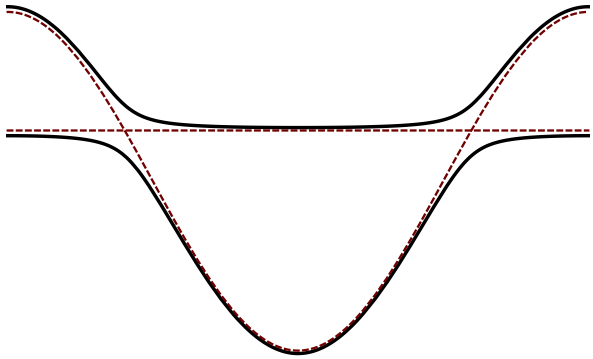

Figure 1.5: Typical band structure of the Anderson (Kondo) lattice model at low temperatures. The solid lines illustrate the hybridized band structures expressed by Eq. (1.2.35). For comparison, we also illustrate the energy band of the conduction electrons $\varepsilon(\boldsymbol{k})$ and the energy level (or the flat band) of the f-electrons ε_f using the broken lines.

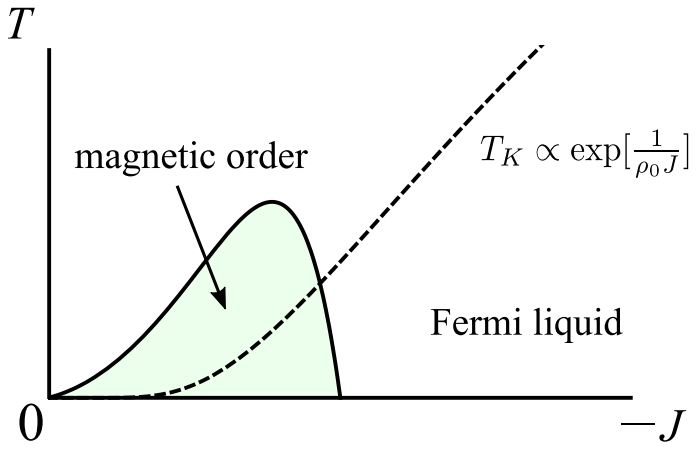

Figure 1.6: Doniach phase diagram of the Kondo lattice systems. the horizontal axis is the antiferromagnetic Kondo coupling $J < 0$ and the vertical axis is the temperature T. The shaded region indicates the appearance of magnetic order due to the RKKY interaction. When the Kondo temperature (the broken line) becomes comparable to the transition temperature of the magnetic order with increasing $-J$, the Kondo effect starts to manifest itself, and the magnetic order vanishes at some critical J.

Fermi-liquid state. Thus, in the phase diagram of the Kondo lattice system, the magnetic order and the Fermi liquid phase are separated by a quantum critical point as illustrated in Fig. 1.6, which is referred to as the Doniach phase diagram [32]. Near the quantum critical point, non-Fermi liquid behavior is often observed and various superconducting states appear. The competition between the RKKY magnetism and the Kondo effect in the Kondo lattice thus provides one of paradigmatic examples of strongly correlated electrons.

3 Topological phase

3.1 Concept of topological phases: classification of gapped ground states

The concept of topological phases arises from a classification of ground states of quantum many-body systems with finite energy gaps in a thermodynamic limit. The concepts of "phase" and "phase transition" are usually understood using the notion of spontaneous symmetry breaking [33]. However, quantum many-body systems can realize numerous distinct phases if the ground states share the same symmetries. Topological phases are such an example.

Let us consider a quantum many-body system described by a Hamiltonian composed of local interactions. We assume that the ground state of the Hamiltonian has a finite excitation gap in the thermodynamic limit. First, we do not assume any symmetry of the Hamiltonian. Then, the ground states are divided into two distinct classes:

(1a) Those which can be adiabatically deformed into a site-product state with a continuous path of Hamiltonian

(1b) Those which cannot be connected to site-product states using any continuous path of Hamiltonian without closing the excitation gap

The latter is called to have a **topological order** (or called a long-range entangled phase) [34]. Examples of topologically ordered phases are fractional quantum Hall (FQH) states [35, 36], chiral spin liquid [37], Z_2 quantum spin liquid [38], and Kitaev's toric code [39], etc. Topologically ordered phases have some exotic properties. For example, although gapped ground states are generically insensitive to local perturbations, the ground states of topologically ordered phases can capture a global structure of the space where it resides, and has nontrivial degeneracy depending on the topological structure (such as genus) of the space [34, 40]. This degeneracy is called as topological ground-state degeneracy. Topological ground-state degeneracy is reflected in nontrivial contribution to entanglement entropy which is known as topological entanglement entropy [41, 42]. Moreover, topologically ordered phases possess excitations with fractionalized quantum numbers [43, 36]. The fractionalized excitations often have exotic quantum statistics which are different from ordinary bosons and fermions, referred to as (Abelian, or non-Abelian) anyons [43, 44]. The non-Abelian anyons can be used to universal quantum computation robust against local perturabations and decoherence [45, 46]. It is also known that the topological ground-state degeneracy is a necessary condition of the existence of fractionalized excitations [47]. Other than the bulk fractionalized excitations, topologically ordered phases often have gapless excitations if the system has edges with open boundaries [48]. These gapless edge excitations are protected by the bulk topological order, and hence are stable against small perturbations such as impurity.

In the above definition of topologically ordered phases, we have not assumed any symmetry of the system and have not imposed any condition for the deformation path of Hamiltonian. However, when we consider symmetries in the system, the concept of topological phases is much enriched. If the system has some symmetries, the ground states have two possibilities:

(2a) The ground state breaks the symmetries of the Hamiltonian
(2b) The ground state preserves the symmetries.

The case (2a) is a standard ordered phase characterized by local order parameters. In the case (2b), the ground state may or may not have topological order. However, if the system has symmetries, we must restrict the deformation paths of Hamiltonian to those which respect the symmetries. Hence, in this case, even if the ground states do not have topological order, the class of ground states is divided into finer subclasses which cannot be connected with each other. The ground states of this kind are called **symmetry-protected topological (SPT) phases** [49, 50]. Namely, SPT phases are characterized by gapped ground states which do not have topological order but cannot be connected to site-product states without breaking the symmetry or closing the energy gap. Although SPT phases possess neither topological ground-state degeneracy nor fractionalized excitations, they have gapless edge excitations unless the edge breaks the symmetries. Examples of SPT phases include topological insulators [51, 52, 53, 54], Haldane phase in spin-1 chains [55, 56], and so on. We note that under the symmetries, the trivial product states are not necessarily the same phase. Such distinct product states are, for example, distinguished by their symmetry eigenvalues. We consider such a case in Chap. 3. More nontrivial examples are discussed in literature [57].

Topologically ordered phases are also divided into finer subclasses when we impose symmetries. Such distinct classes are called **symmetry-enriched topological (SET) phases** [49, 58, 59]. We summarize the above classification in Fig. 1.7.

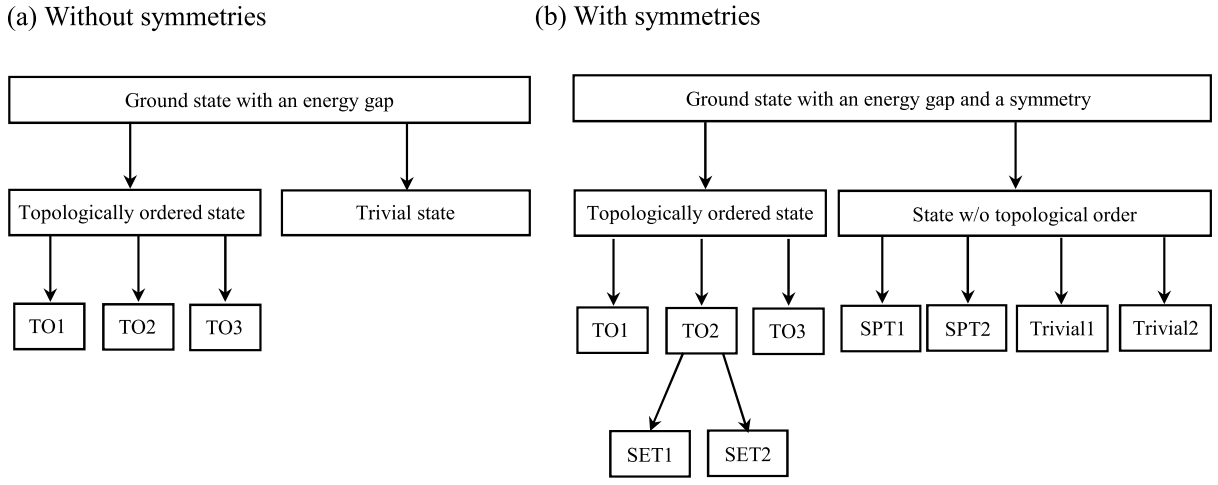

Figure 1.7: Classification of ground states with an energy gap. (a) The case where we do not assume any symmetry of the Hamiltonian and its deformation path. (b) The case where we assume some symmetry of the Hamiltonian and its deformation path. If the ground state breaks the symmetry of the Hamiltonian (which corresponds to the conventional Landau-Ginzburg-type order), the symmetry considered in the right panel is the unbroken symmetry which is retained by the ground state.

3.2 Topological order and fractional quantum Hall effect

In the rest of this section, we explain some examples of topological phases which will be discussed in the later chapters of this thesis. The first example, which is the first topological phase of matter discovered by experiments, is the quantum Hall effect [60, 35]. Electrons can be confined in two-dimensional space at interfaces of semiconductors. The two-dimensional electrons show some plateaus in the Hall conductivity as a function of a magnetic field perpendicular to the two-dimensional plane. At the plateaus, the Hall conductivity is quantized at $\nu\frac{e^2}{h}$, where ν is some rational values. When ν is integer (fractional), this phenomenon is called the integer (fractional) quantum Hall effect. In the quantum Hall states, the longitudinal conductivity vanishes, implying that gapped ground states are realized at the plateaus.

Let us explain the topological order behind the FQH states using a composite-particle picture [61, 62, 63, 64]. We consider interacting electrons in two dimensions under a uniform magnetic field:

$$H = \int d^2\boldsymbol{r}\psi^\dagger(\boldsymbol{r})\frac{[\boldsymbol{p}-e\boldsymbol{A}(\boldsymbol{r})]^2}{2M}\psi(\boldsymbol{r}) + \frac{1}{2}\int d^2\boldsymbol{r}d^2\boldsymbol{r}'\psi^\dagger(\boldsymbol{r})\psi^\dagger(\boldsymbol{r}')V(\boldsymbol{r}-\boldsymbol{r}')\psi(\boldsymbol{r}')\psi(\boldsymbol{r}). \tag{1.3.1}$$

Here $\psi(\boldsymbol{r})$ is the fermion field operator, $\boldsymbol{A} = (Bx, 0)$ is the gauge field, and $V(\boldsymbol{r}-\boldsymbol{r}')$ is the Coulomb interaction. We have neglected the spin degrees of freedom. Under the magnetic field, the electrons form Landau levels. We consider the case of $\nu = 1/q$ filling of the lowest Landau level, where q is an odd integer. Next, we introduce a composite boson operator

$$\phi(\boldsymbol{r}) \equiv e^{-iq\int d^2\boldsymbol{r}'\Theta(\boldsymbol{r}-\boldsymbol{r}')\rho(\boldsymbol{r})}\psi(\boldsymbol{r}). \tag{1.3.2}$$

Here $\Theta(\boldsymbol{r}-\boldsymbol{r}') = \tan^{-1}\frac{y'-y}{x'-x}$ is an angle between the two coordinates, and $\rho(\boldsymbol{r}) = \psi^\dagger(\boldsymbol{r})\psi(\boldsymbol{r})$ is the electron density. The composite operator satisfies the commutation relations $[\phi(\boldsymbol{r}), \phi^\dagger(\boldsymbol{r}')] =$

$\delta(\boldsymbol{r}-\boldsymbol{r}'), [\phi(\boldsymbol{r}), \phi(\boldsymbol{r}')] = 0$, and thus can be regarded as a bosonic field. Physically, the operator (1.3.2) describes a composite object of the electron and q flux quanta. Since a flux quantum leads to π Aharonov-Bohm phase, attaching q flux quanta to the electrons changes their quantum statistics from fermions to bosons. Inserting Eq. (1.3.2) into the Hamiltonian (1.3.1), we obtain

$$H = \int d^2\boldsymbol{r}\phi^\dagger(\boldsymbol{r})\frac{[\boldsymbol{p}-e\boldsymbol{A}(\boldsymbol{r})-e\boldsymbol{a}(\boldsymbol{r})]^2}{2M}\phi(\boldsymbol{r}) + \frac{1}{2}\int d^2\boldsymbol{r}d^2\boldsymbol{r}'\phi^\dagger(\boldsymbol{r})\phi^\dagger(\boldsymbol{r}')V(\boldsymbol{r}-\boldsymbol{r}')\phi(\boldsymbol{r}')\phi(\boldsymbol{r}). \quad (1.3.3)$$

Here we have defined the Chern-Simons gauge field

$$\boldsymbol{a}(\boldsymbol{r}) \equiv \frac{q}{e}\int d^2\boldsymbol{r}'\nabla\Theta(\boldsymbol{r}-\boldsymbol{r}')\rho(\boldsymbol{r}'), \quad (1.3.4)$$

which satisfies

$$(\nabla\times\boldsymbol{a})_z = \frac{2\pi q}{e}\rho(\boldsymbol{r}). \quad (1.3.5)$$

Eq. (1.3.5) means that the Chern-Simons gauge field is accompanied by the electron density, corresponding to the flux attachment. At this stage, let us move to the path-integral representation. The constraint (1.3.5) can be imposed using

$$\prod_{\boldsymbol{r},t}\delta(\varepsilon_{ij}\partial_i a_j - \frac{2\pi q}{e}\rho) = \int \mathcal{D}a_0 \exp\Big[i\int d^2\boldsymbol{r}dt a_0(\frac{\nu e^2}{2\pi}\varepsilon_{ij}\partial_i a_j - e\rho)\Big]. \quad (1.3.6)$$

Then, the Lagrangian density is written in a gauge-invariant form as

$$\begin{aligned}\mathcal{L} =& \mathcal{L}_0 + \mathcal{L}_{\rm CS}, & (1.3.7)\\ \mathcal{L}_0 =& \phi^*(i\partial_t - eA_0 - ea_0)\phi - \phi^*(\boldsymbol{p}-e\boldsymbol{A}-e\boldsymbol{a})^2\phi \\ & - \int d^2\boldsymbol{r}'V(\boldsymbol{r}-\boldsymbol{r}')|\phi(\boldsymbol{r})|^2|\phi(\boldsymbol{r}')|^2, & (1.3.8)\\ \mathcal{L}_{\rm CS} =& \frac{\nu e^2}{4\pi}\varepsilon^{\mu\nu\lambda}a_\mu\partial_\nu a_\lambda. & (1.3.9)\end{aligned}$$

Let us evaluate the partition function

$$Z = \int \mathcal{D}\phi\mathcal{D}a e^{i\int d^2\boldsymbol{r}dt\mathcal{L}} \quad (1.3.10)$$

by its saddle point value. The saddle-point condition for the Chern-Simons gauge field is reduced to Eq. (1.3.5). Thus, this saddle-point solution cancels with the magnetic field from $\boldsymbol{A}$. Then, in the Lagrangian (1.3.8), the boson field ϕ does not feel any magnetic field in average. Thus, the saddle point condition for the boson field ϕ is expected to be the Bose condensation of the bosons. In fact, this saddle point solution describes the FQH effect. To see the electromagnetic response for the above mean-field solution, let us couple the system to a probe gauge field A_μ. The electromagnetic response is deduced from an effective action for A_μ derived by integrating out the matter field ϕ and the Chern-Simons field a_μ. After some calculations, the effective action leads to the Chern-Simons theory described by the Lagrangian

$$\mathcal{L}_{\rm eff} = \frac{\nu e^2}{4\pi}\varepsilon^{\mu\nu\lambda}A_\mu\partial_\nu A_\lambda \quad (1.3.11)$$

at long wavelength. Since the electric current density is written as $j_\mu = \frac{\delta S_{\rm eff}}{\delta A_\mu}$, the Chern-Simons theory (1.3.11) leads to the fractionally quantized Hall conductivity

$$\sigma_{xy} = \nu \frac{e^2}{h}. \tag{1.3.12}$$

Thus, we find that the Chern-Simons theory (1.3.11) describes the FQH effect. The Chern-Simons theory is known as a celebrated example of topological field theory [65]. In general, the low-energy effective theory of topological phases are believed to be described by some topological field theory. In fact, the basic properties of topological order in the FQH states can be extracted from the effective Chern-Simons theory. For example, the topological ground-state degeneracy is derived by considering the Chern-Simons theory on a torus [40]. The fractionalized excitation corresponds to a vortex in the composite-boson condensate, since one flux quantum is accompanied by e/q charge due to the constraint (1.3.5) [64]. The gapless edge excitation can be also derived from the Chern-Simons theory [66].

3.3 One-dimensional SPT phase and Haldane phase

Next, we explain several examples of SPT phases. Let us consider the antiferromagnetic Heisenberg model in one dimension:

$$H = J \sum_j \boldsymbol{S}_j \cdot \boldsymbol{S}_{j+1}, \tag{1.3.13}$$

$$(\boldsymbol{S}_j)^2 = S(S+1), \quad S = \frac{1}{2}, 1, \frac{3}{2}, 2, \cdots, \tag{1.3.14}$$

where $J > 0$. In 1983, Haldane [55, 56] proposed a surprising "conjecture" about the ground-state properties of the model, based on argument of a topological term in effective nonlinear sigma model description. For half-odd-integer $S = 1/2, 3/2, \cdots$, the ground state of the model (1.3.13) is a gapless state without long-range magnetic order. However, for integer $S = 1, 2, \cdots$, the ground state of the model has an energy gap, in sharp contrast with the half-odd-integer case. Also, the ground state is non-degenerate. That is, there is neither magnetic order nor symmetry breaking. The gapped ground state is now called the Haldane phase. Naively, a non-degenerate ground state may be a "boring" trivial state composed of site-product states like $|GS\rangle = |S^z = 0\rangle \otimes |S^z = 0\rangle \otimes \cdots$. To check the non-triviality of the Haldane phase, let us add a single-ion anisotropy to the $S = 1$ Heisenberg model:

$$H = J \sum_j \boldsymbol{S}_j \cdot \boldsymbol{S}_{j+1} + D \sum_j (S_j^z)^2, \tag{1.3.15}$$

whose ground state at $D \to \infty$ is a trivial gapped state $|S^z = 0\rangle \otimes |S^z = 0\rangle \otimes \cdots$. By examining the evolution of ground states for the change of D/J, one can find that there is a quantum phase transition between the Haldane phase and the large-D phase despite of absence of symmetry breaking [67] (Fig. 1.8). Thus, it is implied that the $S = 1$ Haldane phase is a nontrivial gapped ground state which is essentially different from the site-product state. A physical picture of the Haldane phase was provided by Affleck, Kennedy, Lieb, and Tasaki (AKLT) [68, 69]. They considered a Hamiltonian modified from the $S = 1$ Heisenberg model by adding a biquadratic term with a specific coefficient:

$$H_{\rm AKLT} = J \sum_j \Big[\boldsymbol{S}_j \cdot \boldsymbol{S}_{j+1} + \frac{1}{3} (\boldsymbol{S}_j \cdot \boldsymbol{S}_{j+1})^2 \Big]. \tag{1.3.16}$$

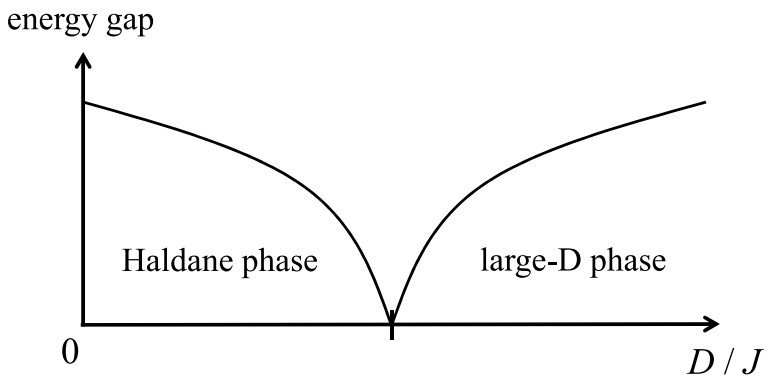

Figure 1.8: Evolution of energy gaps of the model (1.3.15) as a function of the single-ion anisotropy D/J in the unit of the Heisenberg interaction. The energy gap of the Haldane phase gradually shrinks as we increase D/J, and finally the system exhibits a quantum phase transition into a large-D phase.

Figure 1.9: Illustration of the AKLT state for spin-1 chains. Each red ball expresses a spin-1/2 degrees of freedom. The solid line indicates a singlet state between neighboring spins. The solid circle denotes a symmetrization operation of the wavefunction for recovering the state expressed in terms of the original spin-1 degrees of freedom.

The ground state of Eq. (1.3.16) is exactly obtained and is called AKLT state. The AKLT state is illustrated in Fig. 1.9. The spin-1 degree of freedom is first decomposed into two spin 1/2. Then, each spin-1/2 degree of freedom is entangled into a spin-singlet state with a partner at the neighboring site. Finally, by symmetrizing the wavefunction in terms of the two spin-1/2 at the same site, we obtain a ground state expressed in the original spin-1 degrees of freedom. This state is the AKLT state, which is also called a valence-bond-solid state. The AKLT state does not break any symmetry of the system. One can readily see that the AKLT state has a spin-1/2 degrees of freedom at the edge of the system. As mentioned in Sec. 3.1, these edge states are the hallmark of the SPT phase.

If the $S = 1$ Haldane phase is a nontrivial SPT phase, what are the relevant symmetries which protect it from trivial product states? The mechanism of symmetry protection of bosonic SPT phases in one dimension can be universally described using matrix product states (MPS) [70, 71, 72, 73]. A generic 1D ground state can be described by MPS in a canonical form as

$$|\psi\rangle = \sum_{\{i_n\}} \mathrm{Tr}[\Gamma_{i_1}\Lambda\Gamma_{i_2}\Lambda\cdots\Gamma_{i_L}]\,|i_1, i_2, \cdots, i_L\rangle \tag{1.3.17}$$

where we denote the number of sites as L. For simplicity, here we assume the periodic boundary condition and translational invariance. $\{|i_1, i_2, \cdots, i_L\rangle = |i_1\rangle \otimes |i_2\rangle \otimes \cdots \otimes |i_L\rangle\}_{i_1,i_2,\cdots,i_L}$ are the basis of the Hilbert space of the system. Γ_i and Λ are $\chi \times \chi$ matrices satisfying $\sum_i (\Gamma_i)^\dagger \Lambda^2 \Gamma_i = 1$. The elements of the diagonal matrix $(\Lambda)_{\alpha\beta} = \lambda_\alpha \delta_{\alpha\beta}$ give entanglement spectra $\varepsilon_\alpha = -2\ln\lambda_\alpha$ for a cut of the infinite chain into two pieces. A gapped ground state can be represented by MPS (1.3.17) with finite $\chi = \mathcal{O}(1)$ which does not diverge as increasing the system size L.

If two MPS data (Γ_i, Λ) and (Γ'_i, Λ') give the same gapped ground state (up to the U(1) phase ambiguity), they satisfy

$$\Gamma'_i = e^{i\vartheta} U^\dagger \Gamma_i U, \tag{1.3.18}$$

$$\Lambda' = U^\dagger \Lambda U \tag{1.3.19}$$

for a unitary matrix U and a phase factor $\theta \in \mathbb{R}$ [71, 74, 75]. The unitary matrix U is unique up to its U(1) phase. One can easily check that the right hand sides of Eqs. (1.3.18) and (1.3.19) give the original state up to a U(1) phase $e^{iL\vartheta}$. Let us consider a symmetry operation denoted by g and assume that the on-site basis transforms as $|i\rangle \to \sum_j (\tau_g)_{ji} |j\rangle$. Since

$$\begin{aligned} &\sum_{\{i_n\},\{j_n\}} \mathrm{Tr}[\Gamma_{i_1} \Lambda \cdots \Gamma_{i_L}] (\tau_g)_{j_1 i_1} \cdots (\tau_g)_{j_L i_L} |j_1, \cdots, j_L\rangle \\ &= \sum_{\{j_n\}} \mathrm{Tr}[(\sum_{i_1} (\tau_g)_{j_1 i_1} \Gamma_{i_1}) \Lambda \cdots (\sum_{i_L} (\tau_g)_{j_L i_L} \Gamma_{i_L})] |j_1, \cdots . j_L\rangle , \end{aligned} \tag{1.3.20}$$

the MPS data transform as $\Gamma_i \to \sum_j (\tau_g)_{ij} \Gamma_j$ and $\Lambda \to \Lambda$. Thus, if the state is invariant under the symmetry operation, we find

$$\sum_j (\tau_g)_{ij} \Gamma_j = e^{i\vartheta_g} U_g^\dagger \Gamma_i U_g, \tag{1.3.21}$$

$$\Lambda = U_g^\dagger \Lambda U_g, \tag{1.3.22}$$

from Eqs. (1.3.18) and (1.3.19).

The symmetry protection of the Haldane phase can be proven by using the above properties of MPS [76, 77]. Let us consider the following three symmetry operations: the time-reversal (T), bond-centered inversion (I), and the spin dihedral symmetry composed of spin π rotation around each axis (R_x, R_y, R_z). Under those symmetries, the MPS data satisfy the following properties. For time reversal,

$$\sum_j (\tau_T)_{ij} (\Gamma_j)^* = e^{i\vartheta_T} U_T^\dagger \Gamma_i U_T, \tag{1.3.23}$$

$$\Lambda = U_T^\dagger \Lambda U_T. \tag{1.3.24}$$

For spatial inversion,

$$(\Gamma_i)^T = e^{i\vartheta_I} U_I^\dagger \Gamma_i U_I, \tag{1.3.25}$$

$$\Lambda = U_I^\dagger \Lambda U_I. \tag{1.3.26}$$

For the spin π rotation around the $\alpha = x, y, z$ axis,

$$\sum_j (\tau_\alpha)_{ij} \Gamma_j = e^{i\vartheta_\alpha} U_\alpha^\dagger \Gamma_i U_\alpha, \tag{1.3.27}$$

$$\Lambda = U_\alpha^\dagger \Lambda U_\alpha. \tag{1.3.28}$$

U_T, U_I, U_α are unitary matrices, and $\vartheta_T, \vartheta_I, \vartheta_\alpha$ are phase factors. Furthermore, the unitary matrices satisfy

$$ {}^t(U_T) = e^{-i\varphi_T} U_T, \tag{1.3.29} $$

$$ {}^t(U_I) = e^{-i\varphi_I} U_I, \tag{1.3.30} $$

$$ U_x U_z = e^{i\varphi_{xz}} U_z U_x, \tag{1.3.31} $$

where $\varphi_T, \varphi_I, \varphi_{xz} \in \mathbb{R}$ and ${}^tA$ means the transpose of the matrix. The above equations readily lead to quantization of $\varphi_T, \varphi_I, \varphi_{xz}$ to 0 or π. Since the discrete phase factors cannot be changed unless the symmetries are broken or the energy gap collapses, ground states which have different phase factors are necessarily separated by quantum phase transitions. The quantized values of $\varphi_T, \varphi_I, \varphi_{xz}$ thus provide the characterization of the SPT phase. For the Haldane phase, we can calculate the phase factors using the AKLT state. The MPS representation of the AKLT state is given by $\Gamma_i = \sigma_i$ $(i = x, y, z)$ when we choose the on-site basis as $|x\rangle = \frac{1}{\sqrt{2}}(|1\rangle - |-1\rangle), |y\rangle = \frac{i}{\sqrt{2}}(|1\rangle + |-1\rangle), |z\rangle = |0\rangle$ ($|-1\rangle, |0\rangle, |1\rangle$ are the original spin-1 basis). A direct calculation leads to $\varphi_T = \varphi_I = \varphi_{xz} = \pi$, while the trivial large-D state gives $\varphi_T = \varphi_I = \varphi_{xz} = 0$ [76, 77]. Hence, the $S = 1$ Haldane phase is indeed a nontrivial SPT phase and is stable if either of the time-reversal, bond-centered inversion, or spin dihedral symmetries is present.

In contrast, the phase factors[1] $\vartheta_I, \vartheta_\alpha$ mean the eigenvalues of the ground state under symmetry operations, since the symmetry operation maps the ground state $|\psi\rangle$ into $e^{iL\vartheta_\alpha}|\psi\rangle$ $(\alpha = I, x, y, z)$. These phase factors are also quantized to 0 or π due to the property $I^2 = R_x^2 = R_y^2 = R_z^2 = 1$. Although the quantization can distinguish quantum phases which have different symmetry eigenvalues, this property does not lead to SPT phases. In this case, the quantization of $\vartheta_I, \vartheta_{x,y,z}$ diagnoses the distinction between trivial phases. Under certain point-group symmetry, quantization of a combination of ϑ_α and φ_α can also lead to distinct trivial phases [57].

In general, if the system possesses an on-site symmetry of a group G, the MPS data satisfy Eqs. (1.3.21) and (1.3.22). By performing successive symmetry operations associated with group elements $g_1, g_2 \in G$, we obtain

$$ U_{g_1} U_{g_2} = e^{i\varphi(g_1, g_2)} U_{g_1 g_2}, \tag{1.3.32} $$

since the matrix U_g is defined up to a U(1) phase. This fact means that the unitary matrix U_g obeys a projective representation of the group G. If U_g obeys a nontrivial projective representation, the ground state belongs to a SPT phase [72, 73]. We note that one-dimensional representations of U_g always give a trivial projective representation. Thus, it is necessary that the dimension of matrix U_g, or that of Γ and Λ, is larger than one, indicating that there is entanglement between neighboring sites. The off-site entanglement cannot be removed if the ground state belongs to a nontrivial SPT phase. Finally, we note that the phase factor $\varphi(g_1, g_2)$ satisfies the following properties (see also [78]). Since

$$ \begin{aligned} U_{g_1} U_{g_2} U_{g_3} &= e^{i\varphi(g_2, g_3)} U_{g_1} U_{g_2 g_3} \\ &= e^{i\varphi(g_2, g_3) + i\varphi(g_1, g_2 g_3)} U_{g_1} U_{g_2} U_{g_3} \end{aligned} \tag{1.3.33} $$

and

$$ \begin{aligned} U_{g_1} U_{g_2} U_{g_3} &= e^{i\varphi(g_1, g_2)} U_{g_1 g_2} U_{g_3} \\ &= e^{i\varphi(g_1, g_2) + i\varphi(g_1 g_2, g_3)} U_{g_1} U_{g_2} U_{g_3}, \end{aligned} \tag{1.3.34} $$

[1] ϑ_T is actually not well-defined since it depends on the choice of the U(1) phase of the ground state.

we obtain

$$\varphi(g_2, g_3) - \varphi(g_1 g_2, g_3) + \varphi(g_1, g_2 g_3) - \varphi(g_1, g_2) = 0. \tag{1.3.35}$$

Eq. (1.3.35) is called the cocycle condition. On the other hand, since the unitary matrix U_g has the U(1) phase ambiguity in its definition, we can use

$$\tilde{U}_g = e^{i\beta(g)} U_g \tag{1.3.36}$$

instead of U_g. Then, the phase factor $\varphi(g_1, g_2)$ is changed into

$$\tilde{\varphi}(g_1, g_2) = \varphi(g_1, g_2) + [\beta(g_2) - \beta(g_1 g_2) + \beta(g_1)]. \tag{1.3.37}$$

Thus, two phase functions φ and $\tilde{\varphi}$ defined on $G \times G$ describe the same projective representation. The three terms in the bracket $[\cdots]$ in Eq. (1.3.37) is called 2-coboundary. Thus, a set of different projective representations is equivalent to the equivalent class of the phase functions $\varphi(g_1, g_2)$ satisfying the cocycle condition (1.3.35), which is quotiented with the equivalence relation (1.3.37). This equivalent class is denoted by $H^2(G, U(1))$, which is called the second group cohomology of G over U(1). Thus, 1D bosonic SPT phases protected by the on-site symmetry G are classified by the cohomology group $H^2(G, U(1))$ [72, 73]. In general, it was proposed that bosonic SPT phases protected by an on-site symmetry G in spatial dimension d are classified by the $(d+1)$-th group cohomology class $H^{d+1}(G, U(1))$ [49, 79]. However, it was later found that there are some exceptional SPT phases which do not fit into the group cohomology classification [80, 81]. It has been proposed that more accurate classification is given by cobordism theory [82, 83] based on low-energy effective description of SPT phases using topological field theory. We note that in dimensions one or two, which we will consider in the later chapters of this thesis, there is no difference between the group cohomology classification and the cobordism classification.

To be precise, this description using MPS is applicable to bosonic (spin) systems. A fermionic version of MPS was also recently developed [84, 85].

3.4 Two-dimensional SPT phase and bosonic integer quantum Hall effect

As an example of bosonic SPT phases in two dimensions, we explain the bosonic integer quantum Hall (BIQH) effect, which was proposed by Senthil and Levin [86]. We consider two-component bosons with charge $Q = 1$ in a uniform magnetic field (Fig. 1.10) described by a Hamiltonian

$$\begin{aligned} H = &\sum_{\alpha=1,2} \int d^2\boldsymbol{r} \Psi^{(\alpha)\dagger}(\boldsymbol{r}) \frac{[\boldsymbol{p} - \boldsymbol{A}(\boldsymbol{r})]^2}{2M} \Psi^{(\alpha)}(\boldsymbol{r}) \\ &+ \sum_{\alpha,\beta} \frac{1}{2} \int d^2\boldsymbol{r} d^2\boldsymbol{r}' \Psi^{(\alpha)\dagger}(\boldsymbol{r}) \Psi^{(\beta)\dagger}(\boldsymbol{r}') V^{(\alpha\beta)}(\boldsymbol{r} - \boldsymbol{r}') \Psi^{(\beta)}(\boldsymbol{r}') \Psi^{(\alpha)}(\boldsymbol{r}). \end{aligned} \tag{1.3.38}$$

Here $\Psi^{(\alpha)}(\boldsymbol{r})$ $(\alpha = 1, 2)$ denotes the bosonic field operator for the α-th component. The filling factor for each component is set to unity so that the total filling factor is given by $\nu = 1 + 1$.

In the same spirit as Sec. 3.2, we consider composite bosons attached with the magnetic flux piercing the system. Here, the flux coupled to the first component is attached to the second component, and vice versa. Thus the composite operators due to the "mutual flux attachment" are defined by

$$\tilde{\Psi}^{(1)}(\boldsymbol{r}) \equiv e^{-i \int d^2\boldsymbol{r}' \Theta(\boldsymbol{r} - \boldsymbol{r}') \rho^{(2)}(\boldsymbol{r}')} \Psi^{(1)}(\boldsymbol{r}), \tag{1.3.39}$$

$$\tilde{\Psi}^{(2)}(\boldsymbol{r}) \equiv e^{-i \int d^2\boldsymbol{r}' \Theta(\boldsymbol{r} - \boldsymbol{r}') \rho^{(1)}(\boldsymbol{r}')} \Psi^{(2)}(\boldsymbol{r}). \tag{1.3.40}$$

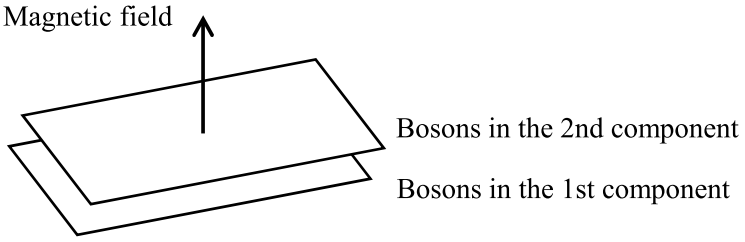

Figure 1.10: Two-component bosons under a uniform magnetic field with the Hamiltonian (1.3.38). Each sheet expresses the bosons in two-dimensional space.

The composite bosons satisfy ordinary commutation relations $[\tilde{\Psi}^{(1)}(\boldsymbol{r}), \tilde{\Psi}^{(1)\dagger}(\boldsymbol{r}')] = [\tilde{\Psi}^{(2)}(\boldsymbol{r}), \tilde{\Psi}^{(2)\dagger}(\boldsymbol{r}')] = \delta(\boldsymbol{r}-\boldsymbol{r}')$ within each component, but anticommute with the other component $\{\tilde{\Psi}^{(1)}(\boldsymbol{r}), \tilde{\Psi}^{(2)}(\boldsymbol{r}')\} = 0$. We also define the Chern-Simons gauge fields $\boldsymbol{a}_\alpha(\boldsymbol{r})$ $(\alpha = 1, 2)$ by

$$\boldsymbol{a}_1(\boldsymbol{r}) \equiv \int d^2\boldsymbol{r}' \nabla\Theta(\boldsymbol{r}-\boldsymbol{r}')\rho^{(2)}(\boldsymbol{r}'), \tag{1.3.41}$$

$$\boldsymbol{a}_2(\boldsymbol{r}) \equiv \int d^2\boldsymbol{r}' \nabla\Theta(\boldsymbol{r}-\boldsymbol{r}')\rho^{(1)}(\boldsymbol{r}'), \tag{1.3.42}$$

which satisfy

$$(\nabla \times \boldsymbol{a}_1)_z = 2\pi\rho^{(2)}(\boldsymbol{r}), \tag{1.3.43}$$

$$(\nabla \times \boldsymbol{a}_2)_z = 2\pi\rho^{(1)}(\boldsymbol{r}). \tag{1.3.44}$$

By imposing the constraint (1.3.41) and (1.3.42) on the path integral using

$$\begin{aligned}&\int \mathcal{D}\boldsymbol{a}_1 \mathcal{D}\boldsymbol{a}_2 \prod_{\boldsymbol{r},t} \delta(\varepsilon_{ij}\partial_i a_{1j} - 2\pi\rho^{(2)})\delta(\varepsilon_{ij}\partial_i a_{2j} - 2\pi\rho^{(1)}) \\ &= \int \mathcal{D}a_1 \mathcal{D}a_2 \exp\Big[i\int d^2\boldsymbol{r}dt\Big\{a_{20}(\frac{1}{2\pi}\varepsilon_{ij}\partial_i a_{1j} - \rho^{(2)}) + a_{10}(\frac{1}{2\pi}\varepsilon_{ij}\partial_i a_{2j} - \rho^{(1)})\Big\}\Big],\end{aligned} \tag{1.3.45}$$

the Lagrangian density is written in a gauge-invariant form

$$\mathcal{L} = \sum_{\alpha=1,2} \mathcal{L}_\alpha + \mathcal{L}_{\rm int} + \mathcal{L}_{\rm CS}, \tag{1.3.46}$$

$$\mathcal{L}_\alpha = \tilde{\Psi}^{(\alpha)*}(i\partial_t - A_0 - a_{\alpha 0})\tilde{\Psi}^{(\alpha)} - \tilde{\Psi}^{(\alpha)*}(\boldsymbol{p} - \boldsymbol{A} - \boldsymbol{a}_\alpha)^2\tilde{\Psi}^{(\alpha)}, \tag{1.3.47}$$

$$\mathcal{L}_{\rm int} = -\sum_{\alpha,\beta}\int d^2\boldsymbol{r}' V^{(\alpha\beta)}(\boldsymbol{r}-\boldsymbol{r}')|\tilde{\Psi}^{(\alpha)}(\boldsymbol{r})|^2|\tilde{\Psi}^{(\beta)}(\boldsymbol{r}')|^2, \tag{1.3.48}$$

$$\mathcal{L}_{\rm CS} = \frac{1}{4\pi}\varepsilon^{\mu\nu\lambda}(a_{1\mu}\partial_\nu a_{2\lambda} + a_{2\mu}\partial_\nu a_{1\lambda}). \tag{1.3.49}$$

At the mean-field level, the flux of Chern-Simons gauge fields effectively cancels the magnetic field due to $\boldsymbol{A}$. Thus, the mean-field solution is a Bose-Einstein condensate of the two-component bosons $\tilde{\Psi}^{(1)}$ and $\tilde{\Psi}^{(2)}$. Let us examine the long-wavelength response to probe gauge fields $A_{1\mu}$ $(A_{2\mu})$, which couples to bosons in the first (second) component, respectively. The effective theory leads to the Chern-Simons theory

$$\mathcal{L}_{\rm eff} = \frac{1}{4\pi}\varepsilon^{\mu\nu\lambda}(A_{1\mu}\partial_\nu A_{2\lambda} + A_{2\mu}\partial_\nu A_{1\lambda}). \tag{1.3.50}$$

To gain some insights to the response described by Eq. (1.3.50), let us introduce linear combinations of the gauge fields as $A_{c\mu} = (A_{1\mu} + A_{2\mu})/2$ and $A_{s\mu} = (A_{1\mu} - A_{2\mu})/2$. Then, Eq. (1.3.50) is rewritten as

$$\mathcal{L}_{\text{eff}} = \frac{1}{2\pi}\varepsilon^{\mu\nu\lambda}(A_{c\mu}\partial_\nu A_{c\lambda} - A_{s\mu}\partial_\nu A_{s\lambda}). \tag{1.3.51}$$

The above theory describes quantized Hall conductivity $\sigma^c_{xy} = +2\frac{Q^2}{h^2}$ and quantized spin Hall conductivity $\sigma^s_{xy} = -2\frac{Q^2}{h}$.

We can also derive an effective edge theory from the bulk Chern-Simons theory (1.3.50) [66]. The edge theory is

$$\mathcal{L}_{\text{edge}} = \frac{1}{4\pi}(\partial_x\phi_1\partial_t\phi_2 + \partial_x\phi_2\partial_t\phi_1 - \sum_{I,J=1,2} v_{IJ}\partial_x\phi_I\partial_x\phi_J) \tag{1.3.52}$$

where the Tomonaga-Luttinger bosons ϕ_1, ϕ_2 satisfy the Kac-Moody algebra

$$[\partial_x\phi_1(x), \partial_{x'}\phi_1(x')] = [\partial_x\phi_2(x), \partial_{x'}\phi_2(x')] = 0, \tag{1.3.53}$$

$$[\partial_x\phi_1(x), \partial_{x'}\phi_2(x')] = 2\pi i\partial_x\delta(x - x'), \tag{1.3.54}$$

and $v = \{v_{IJ}\}_{I,J}$ is a non-universal velocity matrix. The edge theory (1.3.52) describes counter-propagating chiral modes (Fig. 1.11). One of the two chiral modes corresponds to a charge mode which carries the charge +2. On the other hand, the other chiral mode is a charge-neutral mode which carries a pseudospin quantum number if we regard the two components as the pseudospin. By checking the stability of the edge modes, we can see the symmetry protection of the BIQH state as a SPT phase [87]. Although the original system (1.3.38) possesses the U(1) × U(1) symmetry associated with the charge conservation in each component, here we only assume the U(1) symmetry for the total charge conservation. This symmetry is expressed in terms of the boson fields as

$$\phi_1 \to \phi_1 + \varphi,$$
$$\phi_2 \to \phi_2 + \varphi, ,$$

since the original bosons are expressed by $b_\alpha \propto e^{i\phi_\alpha}$. Thus, the only possible perturbation consistent with the symmetry is

$$g\cos[n(\phi_1 - \phi_2)] \tag{1.3.55}$$

with $n \in \mathbb{Z}$. However, the perturbation (1.3.55) cannot lock the boson fields at their potential minimum, since

$$[\partial_x(\phi_1(x) - \phi_2(x)), \partial_{x'}(\phi_1(x') - \phi_2(x')] = -4\pi i\partial_x\delta(x - x') \neq 0$$

and thus the field $\phi_1 - \phi_2$ cannot have a definite value over the entire space due to the uncertainty principle. We therefore conclude that the edge theory (1.3.52) remains gapless unless we break the charge U(1) symmetry. The stability of the gapless edge modes means that the BIQH state is a SPT phase protected by the charge U(1) symmetry. Intuitively, the above stability of the edge modes can be understood by the following picture; since one chiral mode carries the charge quantum number $Q = +2$ while the other carries $Q = 0$, the backscattering between the two chiral modes is forbidden by the charge conservation (Fig. 1.11). The absence of the backscattering implies that the counterpropagating chiral modes are stable under the symmetry.

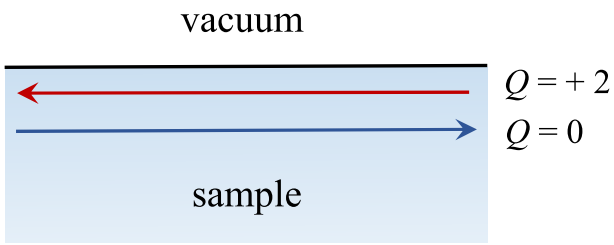

Figure 1.11: Schematic picture of the edge of the BIQH state. The two-dimensional sample is separated from the vacuum by a sharp boundary. At the boundary, two chiral modes counterpropagate along the edge. In the figure, the chiral mode with charge $Q = 2$ propagates to left, and the other chiral mode with $Q = 0$ propagates to right.

After the original proposal by Senthil and Levin [86] using the composite-boson mean field theory, numerical exact diagonalization studies found that the BIQH state is indeed the ground state of the Hamiltonian (1.3.38) with contact interactions $V^{(\alpha\beta)}(\boldsymbol{r} - \boldsymbol{r}') = g^{(\alpha\beta)}\delta(\boldsymbol{r} - \boldsymbol{r}')$ ($g^{(\alpha\beta)} > 0$) when the ratio $g^{(12)}/g^{(11)} = g^{(12)}/g^{(22)}$ is close to unity [88, 89, 90]. Several lattice models to realize the BIQH state have been also proposed [91, 92, 93, 94].

3.5 Fermionic SPT phase

So far, we have discussed the SPT phases mainly focusing on bosonic (or spin) systems. Since free bosons condense into the one-particle ground state at zero temperature, SPT phases of bosons naturally require interactions. However, the role of interaction on SPT phases is somewhat different when we consider fermions. Thanks to Pauli's exclusion principle, fermions can realize gapped ground state even if they are non-interacting. Typical examples of such gapped ground states are band insulators. By constraining the systems with symmetries, band insulators are classified into different SPT phases, and the nontrivial ones are known as topological insulators [51, 52, 53, 54]. In the same spirit, gapped ground states with conventional Landau-Ginzburg-type order can be classified by their unbroken symmetries using mean-field Hamiltonians. In the case of superconductivity, nontrivial SPT phases are called topological superconductors [95, 96]. The topological insulators and topological superconductors are classified under time-reversal, particle-hole, and chiral symmetries [97, 98, 99], and the classification was later extended to the case of crystalline symmetries [100, 101, 102, 103, 104].

Naturally expected, interactions have dramatic effects on the fate of the free-fermion SPT phases. When we allow interactions, a subset of nontrivial free-fermion SPT phases can be adiabatically deformed into a trivial phase. In other words, classifications of free-fermion SPT phases, which are given by Abelian groups such as $\mathbb{Z}$ and $\mathbb{Z}_2$, are reduced to their subgroup. Particularly, reductions from $\mathbb{Z}$ to $\mathbb{Z}_N$ have been found in various symmetry classes [105, 75, 106, 107, 108, 109, 110, 111, 112].

Let us illustrate the reduction of free-fermion classification of SPT phases by interactions, using the first example of such reduction discovered by Fidkowski and Kitaev [105, 75]. We consider a mean-field model of 1D topological superconductors with time-reversal symmetry (class BDI in the classification table in Ref. [97, 99]). The quadratic Hamiltonian is

$$H_0 = -\frac{t}{2}\sum_{j=1}^{N}(c_j^\dagger c_{j+1} + c_j^\dagger c_{j+1}^\dagger + \text{h.c.}) + u\sum_{j=1}^{N} c_j^\dagger c_j, \tag{1.3.56}$$

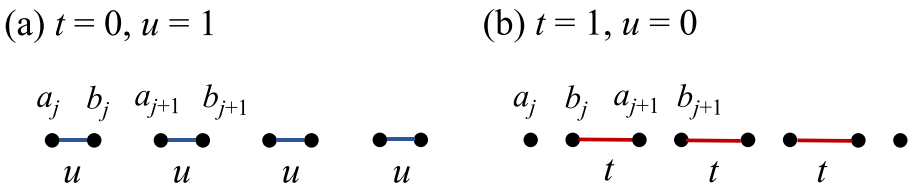

Figure 1.12: Schematic picture of the ground state of the Kitaev chain (1.3.56) with specific values of parameters t, u. The fermion c_j at each site is decomposed into two Majorana fermions a_j and b_j. The Hamiltonian can be written by the bonding of two Majorana fermions as Eq. (1.3.61). The bonding is expressed by the solid lines in the figure.

which was originally proposed by Kitaev [95]. Here $t, u \geq 0$. The Hamiltonian is symmetric for time reversal

$$\mathcal{T} c_j \mathcal{T}^{-1} = c_j, \quad \mathcal{T} c_j^\dagger \mathcal{T}^{-1} = c_j^\dagger, \quad \text{(with complex conjugation)} \tag{1.3.57}$$

and also has a fermion-parity symmetry

$$Q H_0 Q^\dagger = H_0, \quad Q = \exp\Big[i\pi \sum_{j=1}^{N} c_j^\dagger c_j \Big]. \tag{1.3.58}$$

The latter symmetry means that the Hamiltonian preserves the parity of particle number. We rewrite the Hamiltonian (1.3.56) by Majorana fermions

$$a_j \equiv c_j + c_j^\dagger, \tag{1.3.59}$$

$$b_j \equiv -i(c_j - c_j^\dagger), \tag{1.3.60}$$

as

$$H_0 = \frac{i}{2}\Big(t \sum_{j=1}^{N} b_{j-1} a_j + u \sum_{j=1}^{N} a_j b_j \Big) \tag{1.3.61}$$

where we define $b_0 = 0$. A schematic picture is illustrated in Fig. 1.12. The fermion c_j at each site j is divided into two Majorana fermions a_j and b_j. At $t = 0, u = 1$, the system is completely site-decoupled and the ground state is the vacuum $|\text{vac}\rangle$ of fermions which satisfies $c_j |\text{vac}\rangle = 0$. On the other hand, at $t = 1, u = 0$, the Hamiltonian can be written by new complex fermions

$$\tilde{c}_j \equiv \frac{a_{j+1} + i b_j}{2} \quad (j = 1, \cdots, N-1) \tag{1.3.62}$$

as

$$H_0(t = 1, u = 0) = -\sum_{j=1}^{N} \tilde{c}_j^\dagger \tilde{c}_j. \tag{1.3.63}$$

Thus the ground state is $|\psi\rangle = \prod_j \tilde{c}_j^\dagger |\text{vac}\rangle$. In this case, two Majorana fermions a_1, b_N do not appear in H_0 and hence these modes give zero-energy states. In fact, the ground state of Eq. (1.3.56) belongs to a topological phase in $u < t$ and a trivial phase in $u > t$. At the critical point $u = t$, the ground state is gapless.

Other topological phases in this class can be obtained by preparing some multiple copies of the topological phase of the single chain. To check the stability of the Majorana zero modes of the

multiple chains, let us restrict ourselves to the low-energy Hilbert space which is spanned by the edge Majorana fermions [113]. We denote the edge Majorana fermion at the left edge of the n-th wire as $a^{(n)}$. Then, the only possible quadratic Hamiltonian composed of $a^{(n)}$ and $a^{(m)}$ $(n \neq m)$ is

$$\begin{aligned} H_{\text{edge}} &= i a^{(n)} a^{(m)} \\ &= 2(f^\dagger f - \frac{1}{2}). \end{aligned} \tag{1.3.64}$$

In the second line, we have introduced a complex fermion $f \equiv (a^{(n)} + i a^{(m)})/2$. The Hamiltonian (1.3.64) has a non-degenerate ground state with no occupancy of the f-fermion. However, the Hamiltonian (1.3.64) breaks the time-reversal symmetry (1.3.57). Thus, if the system has the time-reversal symmetry, we cannot open an energy gap for the Majorana edge mode. As a result, arbitrary n copies of Kitaev chains provides different topological phases with n Majorana modes at one edge. The time-reversal invariant topological superconductors are therefore classified by integer $\mathbb{Z}$ when we do not consider interactions.

However, if we allow interactions, the classification is reduced to its subgroup. To see this, let us consider n copies of the Kitaev chains and examine the stability of the Majorana edge modes against interactions. The case of $n = 1$ is trivial, since there only exists an isolated Majorana edge mode at low energies. Similarly, we can easily see that the Majorana modes are stable when n is odd, since not all Majorana modes can be paired. For $n = 2$, the only possible edge Hamiltonian is (1.3.64) since Majorana fermions satisfy $(a^{(n)})^2 = 1$. Since (1.3.64) is forbidden by the time-reversal symmetry, the Majorana edge modes are stable in this case. For $n = 4$, we can consider only one nontrivial interaction

$$\begin{aligned} H_{\text{edge}} &= a^{(1)} a^{(2)} a^{(3)} a^{(4)} \\ &= 4(f_1^\dagger f_1 - \frac{1}{2})(f_2^\dagger f_2 - \frac{1}{2}). \end{aligned} \tag{1.3.65}$$

In the second line, the complex fermions are defined by $f_1 \equiv (a^{(1)} + i a^{(2)})/2$ and $f_2 \equiv (a^{(3)} + i a^{(4)})/2$. Since the ground state of the edge Hamiltonian is doubly degenerate, $f_1^\dagger |\text{vac}\rangle$ and $f_2^\dagger |\text{vac}\rangle$, we conclude that the $n = 4$ system is still a nontrivial topological phase. The breakdown of topological phases happens for $n = 8$. In this case, we can consider an edge Hamiltonian

$$H_{\text{edge}} = \boldsymbol{S}_1 \cdot \boldsymbol{S}_2 \tag{1.3.66}$$

where the spin operator

$$\boldsymbol{S}_1 \equiv (f_1^\dagger, f_2^\dagger) \boldsymbol{\sigma} \begin{pmatrix} f_1 \\ f_2 \end{pmatrix}, \quad \boldsymbol{S}_2 \equiv (f_3^\dagger, f_4^\dagger) \boldsymbol{\sigma} \begin{pmatrix} f_3 \\ f_4 \end{pmatrix} \tag{1.3.67}$$

is defined by four complex fermions $f_1, \cdots, f_4$ composed of the eight Majorana edge modes. The Hamiltonian (1.3.66) preserves the time-reversal symmetry. The ground state of Eq. (1.3.66) is a singlet state, and hence non-degenerate. Thus we conclude that the eight copies of Kitaev chains can be adiabatically connected to the trivial phase without edge Majorana zero modes. As a result, the classification is reduced from $\mathbb{Z}$ to $\mathbb{Z}_8$.

We have shown an example of reduction of classification of non-interacting topological phases. A natural question is whether there exists a SPT phase of fermions which cannot be deformed into non-interacting cases. Several examples are discussed in literatures [114, 115, 116].

4 Ultracold Atoms

4.1 Basics of ultracold atoms

Since the successful generation of Bose-Einstein condensates [117, 118, 119], ultracold atomic gases have offered a versatile platform to study quantum many-body physics. The atoms are trapped in vacuum using a magnetic or optical field and can be cooled down to ultralow temperatures using laser-cooling techniques. Typically the number of particles is from 10^4 to 10^7 and the energy scales are from an order of 100 nK to 10 μK. Although the interactions between atoms are originally a van der Waals type and depend on atomic structures in a complicated manner, the low-energy scattering properties are governed by only s-wave scattering. Thus the interactions can be effectively reduced to a short-range contact interaction and described by one parameter, namely, the s-wave scattering length a_s, regardless of the details of atomic structures.

One of the most important techniques in cold-atom experiments is optical lattice [120]. When the atoms are irradiated by an off-resonant optical field, the atomic levels are effectively shifted due to virtual absorption and emission of photons (AC Stark effect). The level shift can be regarded as a potential for the atoms, written as

$$V(\boldsymbol{r}) = -\frac{1}{2}\alpha(\omega)|\boldsymbol{E}(\boldsymbol{r})|^2 \tag{1.4.1}$$

where $\alpha(\omega)$ is the AC polarizability and $|\boldsymbol{E}(\boldsymbol{r})|^2$ is the time-averaged value of the AC electric field with frequency ω. When the optical field forms a standing wave $|\boldsymbol{E}(\boldsymbol{r})|^2 = E^2\cos^2(\boldsymbol{k}\cdot\boldsymbol{r})$, the potential (1.4.1) plays a role of periodic lattice. If the lattice potential is sufficiently deep, it is appropriate to expand the Hamiltonian using the Wannier basis. Thus the atoms in optical lattice are well described by the Hubbard model [121], which reads

$$H_{BH} = -t\sum_{\langle i,j\rangle}(b_i^\dagger b_j + \text{h.c.}) + \frac{U}{2}\sum_j (n_j - 1)^2 \tag{1.4.2}$$

for bosonic atoms and

$$H_{FH} = -t\sum_{\langle i,j\rangle,\sigma}(c_{i\sigma}^\dagger c_{j\sigma} + \text{h.c.}) + U\sum_j n_{j\uparrow}n_{j\downarrow} \tag{1.4.3}$$

for fermionic atoms. The above models (1.4.2) and (1.4.3) are the most simplest setup for atoms in optical lattice. By utilizing various atomic properties and atom-light coupling, we can realize more complicated models which show intriguing physics. We will see several examples in the following subsections.

4.2 Realization of topological phases in ultracold atoms

Thanks to the high controllability, ultracold atoms offer a versatile platform to investigate topological phases. One of promising routes to realize topological phases is to couple the particles to some gauge fields as in the case of the quantum Hall effect. However, since the atoms are electrically neutral, applying magnetic fields only gives rise to the Zeeman shift of the atomic levels and there is no contribution of the vector potential. An important technique to overcome the difficulty is called synthetic gauge fields [122]. The particles under the gauge fields acquire the Aharonov-Bohm phase along their motion. Thus, if some phases can be imprinted to the motion of atoms, the system

effectively mimics the effect of gauge fields. Such synthesis of the gauge fields can be realized using various methods. The first experiment which was reported by Lin *et al.* [123] utilized a spatially varying Raman beam, by which the induced Berry phase was equivalent to the vector potential of a uniform magnetic field. Consequently they observed vortex lattice formations in Bose-Einstein condensates which were not subjected to optical lattice potentials. Using the same idea, synthetic gauge fields corresponding to an electric field [124] and spin-orbit coupling [125] were realized. After the above implementations for bosonic atoms, synthetic magnetic fields or spin-orbit couplings for fermionic atoms have been also realized [126, 127]. However, there has been so far no report of realization of the integer or fractional quantum Hall effect using ultracold atoms in continuum space (i.e. without lattice potentials).

The synthetic gauge fields can be also implemented in optical lattice systems. Using Raman-assisted hopping which imprints a U(1) phase, a lattice model with a uniform magnetic flux, called the Harper-Hofstadter model, were realized [128, 129, 130]. The Harper-Hofstadter model hosts topologically nontrivial band structures accompanied by nonvanishing Chern numbers, depending on the magnitude of flux. If the Chen number is nonzero, the atoms loaded in the optical lattice show a drift motion perpendicular to an applied gravitational potential, which corresponds to the Hall effect in electron systems. By observing the drift motion of atomic clouds, the Chern number of the topological band structure was measured in the Hofstadter model [131]. Another important technique to simulate the effect of the gauge fields is lattice shaking. When the optical lattice is modulated periodically in time and the modulation frequency is sufficiently high compared to the bandwidth, the transfer integral is effectively modified by time averaging the modulation. Using carefully tailor-made protocols for the lattice modulation, the transfer integral acquires a phase factor and thus mimics the Peierls phase due to gauge fields [132, 133]. With a similar idea, the Haldane model [51] accompanied by Chern insulating phases was realized in honeycomb optical lattice and associated drift motions corresponding the nontrivial Chern number were observed [134].

Although the ultracold atoms are useful to realize various models with topological phases, observation of associated edge states involves some difficulties. Since the atoms are usually trapped by harmonic confinement, the "edge" of the atomic cloud is not sharp and correspondingly a metallic region is formed near the edge. Thus the edge states are admixed with the metallic region and there is in general no clear signature of the edge states. There have been some proposals to avoid the difficulty of the smooth edge. One idea is so-called "synthetic dimension" technique [135]. In this technique, we regard the internal states of atoms as another "dimension" of the system. Since there is no potential difference among the internal states, a sharp edge is realized for the synthetic dimension. Furthermore, Raman transitions between the internal states are shown to be equivalent to the flux piercing a plane spanned by the real axis and the synthetic dimension. Using this technique, the edge states of the integer quantum Hall state have been observed [136, 137]. Another idea is to create interface between the topological phase and the trivial phase. Using an amplitude-chirped optical lattice, an edge state associated with the Su-Schriffer-Heeger model have been observed [138].

In addition to the realization of topological phases in equilibrium states, real-time manipulation of optical lattice enables the realization of dynamical topological phenomena. By superimposing two optical lattice with different wavelengths, the Rice-Mele model for topological pumping have been realized [139, 140, 141]. We focus on this phenomenon in Chap. 4.

Finally, we remark that the aforementioned experiments mostly focused on topological phases of non-interacting systems (i.e. topologically nontrivial band structures). Since interactions can be easily introduced to atoms, it is expected that ultracold atoms also offer a platform to realize

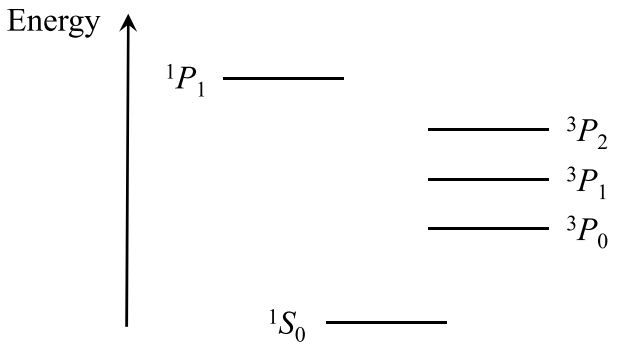

Figure 1.13: Typical energy diagram of AEA. The $^1S_0$ is the electronic ground state. The $^3P_0$ state and the $^3P_2$ state form metastable excited states with long lifetimes in a 10 second order. On the other hand, the $^3P_1$ state and the $^1P_1$ state have short lifetimes.

interacting topological phases. In Chap. 3, we address this problem using the realization of Kondo lattice systems in ultracold atoms.

4.3 Ultracold alkaline-earth atoms

Basic properties

The atomic species which is often used for cold-atom experiments is alkali metals, such as Rb, Li, and K. However, the laser-cooling of alkaline-earth atoms, such as Ca and Sr, and rare-earth Yb atoms, have also succeeded [142, 143, 144, 145, 146] (for reviews, see [147, 148]). These atoms have two electrons in the most outer shell. Thus the electronic ground state is a spin-singlet state denoted by $^1S_0$. Here we have written the electronic state as ^SL_J using the orbital angular momentum $L = 0(S), 1(P), 2(D), \cdots$, the spin quantum number S, and the total angular momentum J. The low-lying excited states have $L = 1$, and the $^3P_0$ state has the lowest energy (Fig. 1.13). Since the $^1S_0$ and $^3P_0$ states have the same total angular momentum $J = 0$, the optical dipole transition between them is forbidden. When the hyperfine interaction with nuclear spins are taken into account for fermionic isotopes, the optical transition is possible since the $^3P_0$ state and the $^1P_1$ state are hybridized. However, since the mixing of two states due to the hyperfine interaction are quite small, the $^3P_0$ state is long-lived and the lifetime reaches about 10 seconds. The long-lived excited state and the optical transition with ultranarrow linewidth has versatile applications, such as optical lattice clocks with the highest precision in the world [149]. In Chaps. 2 and 3, we utilize the long-lived excited state for realizing the Kondo effect in ultracold atoms.

The alkaline-earth-like atoms (AEA) have yet another interesting property. The spin degrees of freedom of AEA come from the nuclear spin I because the electrons form the $J = 0$ state. Since the interactions between atoms are determined by the electronic states, the interactions and the corresponding s-wave scattering lengths are independent of the spin degrees of freedom. Thus the atom-atom interactions possess the SU($2I+1$) symmetry which is enlarged from the ordinary SU(2) symmetry [150, 151]. Thus ultracold AEA in optical lattice are a rare example of realization of the SU(N) Hubbard model in nature.

Experimental progress

Here we briefly review the experimental progress on ultracold AEA. The first achievement of laser cooling of AEA down to quantum degeneracy was a generation of Bose-Einstein condensate using Yb atoms [142]. For Yb atoms in optical lattice, a superfluid-Mott-insulator transition has been demonstrated [152]. Also, using fermionic isotopes of Yb atoms, Fermi degeneracy [143, 153] and a Mott insulating state [154] have been realized. As explained above, the fermionic isotopes of AEA have the SU(N) symmetry in the interactions. The properties of SU(N) systems have been investigated for the Mott insulators [154, 155] and one-dimensional Tomonaga-Luttigner liquid states [156]. Since the $^3P_0$ state has the total angular momentum $J = 0$, interactions between the $^1S_0$ state and the $^3P_0$ state are also SU(N) symmetric. This feature has been indeed confirmed by experiments [157, 158]. Recently, a spin-orbit coupling using the two orbital degrees of freedom have been realized [159].

Similar experiments for Sr atoms have been also performed. Bose-Einstein condensation for bosonic isotopes [144, 145, 160, 161] and Fermi degeneracy for fermionic isotopes [162] have been realized. Also, the SU(N) exchange interaction between the $^1S_0$ state and the $^3P_0$ state have been measured [163].

For Ca atoms, a generation of Bose-Einstein condensate has succeeded [146]. However, there has been no report on Fermi degeneracy using fermionic isotopes.

Finally we remark the Feshbach resonance for AEA. In cold-atom experiments, a technique called Feshbach resonance [164] is often used to control the interactions (or the scattering lengths) of atoms. However, since the AEA have the $J = 0$ ground state, one cannot use the ordinary magnetic Feshbach resonance between the $^1S_0$ state. However, optical Feshbach resonance [165] is available and magnetic Feshbach resonance between the ground state and the $^3P_2$ state [166, 167] have been observed. Furthermore, based on a new mechanism called orbital Feshbach resonance [168], resonance between the $^1S_0$ state and the $^3P_0$ state has been observed [169, 170].

Chapter 2

Laser-Induced Kondo Effect in Ultracold Alkaline-Earth Atoms

In this chapter, we demonstrate that laser irradiation to AEA in optical lattice can coherently induce a novel Kondo effect. By utilizing the ${}^1S_0$ and the ${}^3P_0$ states explained in Sec. 4.3 in the previous chapter, it is shown that the optically coupled two internal states are dynamically entangled to form the Kondo-singlet state, overcoming the heating effect due to the irradiation. Furthermore, a lack of SU(N) symmetry in the optical coupling provides a peculiar feature in the Kondo effect, which results in spin-selective renormalization of effective masses. We also discuss effects of interorbital exchange interactions, and show that they induce novel crossover or reentrant behavior of the Kondo effect owing to control of the coupling anisotropy. This property is examined more deeply in the next chapter.

1 Setup

We consider ultracold fermionic AEA in a three-dimensional optical lattice which consist of the ${}^1S_0$ state and the ${}^3P_0$ state. The fermionic annihilation operators of the ${}^1S_0$ and ${}^3P_0$ states at site i are denoted as $c_{i\sigma}$ and $f_{i\sigma}$ respectively, and also as $c_{\boldsymbol{k}\sigma}$ and $f_{\boldsymbol{k}\sigma}$ for their Fourier transform. Here $\sigma = -I, \cdots, I$ labels the z component of the nuclear spin. As we have explained in Sec. 4.1 in the previous chapter, the atoms in each state in optical lattice can be described by the Hubbard model (1.4.3). Thus the system is initially prepared with the Hamiltonian

$$\mathcal{H}_0 = \sum_{\boldsymbol{k},\sigma} (\varepsilon_c(\boldsymbol{k}) c^\dagger_{\boldsymbol{k}\sigma} c_{\boldsymbol{k}\sigma} + \varepsilon_f^{(0)} f^\dagger_{\boldsymbol{k}\sigma} f_{\boldsymbol{k}\sigma}) + U \sum_{i,\sigma<\sigma'} n_{fi\sigma} n_{fi\sigma'} \tag{2.1.1}$$

with $n_{fi\sigma} = f^\dagger_{i\sigma} f_{i\sigma}$, where we denote the band dispersion of each orbital as $\varepsilon_c(\boldsymbol{k})$ and $\varepsilon_f^{(0)}$. The setup is illustrated in Fig. 2.1 (a). An important point is that the two internal states have different polarizability to the light. Thus, the depths of the optical lattice potentials (1.4.1) can be changed between the ${}^1S_0$ state and the ${}^3P_0$ state by choosing an appropriate wavelength of the laser. Here, we implement an optical lattice in which the ${}^3P_0$ state feels a deep potential while the ${}^1S_0$ state is confined weakly [150]. We assume that the ${}^3P_0$ state is completely localized due to the strong confinement and thus is dispersionless, experiencing strong on-site repulsion $U > 0$. For the moment, we neglect other interatomic interactions. In the initial setup, we assume that the system is in

thermal equilibrium with temperature T_0. The chemical potential for the ${}^1S_0$ orbital is μ_0, and the immobile ${}^3P_0$ state is assumed to be singly occupied at each site.

At this stage, let us apply a monochromatic laser at time $t = 0$ which induces the ${}^1S_0$-${}^3P_0$ transition allowed by the electric dipole coupling with the help of hyperfine interaction (see Sec. 4.3 in the previous chapter):

$$\mathcal{H}_{\rm mix} = \theta(t) \sum_{i,\sigma,\sigma'} (\boldsymbol{V} \cdot \boldsymbol{\sigma}_{\sigma\sigma'} e^{i\boldsymbol{K}\cdot\boldsymbol{R}_i - i\omega t} f^\dagger_{i\sigma} c_{i\sigma'} + \text{h.c.}). \tag{2.1.2}$$

Here we consider the simplest setup for the application of the laser, and $\theta(t)$ is the Heaviside step function. After $t = 0$, the system evolves in time under the Hamiltonian $\mathcal{H}_0 + \mathcal{H}_{\rm mix}$. The coupling coefficient in $\mathcal{H}_{\rm mix}$ is calculated from matrix elements of $-\boldsymbol{d} \cdot \boldsymbol{E}$, where $\boldsymbol{d}$ is the electric dipole moment and $\boldsymbol{E}$ is the electric field of light. Using the Wigner-Eckart theorem [171], the matrix elements of $\boldsymbol{d}$ are proportional to those of the nuclear spin operator $\boldsymbol{\sigma}_{\sigma\sigma'}$, since there is no electronic angular momentum.

Our central idea is that the Hamiltonian $\mathcal{H} = \mathcal{H}_0 + \mathcal{H}_{\rm mix}$ mimics the Anderson lattice model, which has been introduced by Eq. (1.2.31). Here the hybridization term $\mathcal{H}_{\rm mix}$ induces an effective antiferromagnetic interaction between the orbitals. The space-time oscillation of the optical field in Eq. (2.1.2) can be eliminated easily. After a gauge transformation $f_{i\sigma}(t) = e^{i\boldsymbol{K}\cdot\boldsymbol{R}_i - i\omega t} f'_{i\sigma}(t)$, the optical coupling takes a stepwise form in time. Hence, in this setup the hybridization term is suddenly turned on, and this corresponds to a "hybridization quench" problem of the Anderson lattice model. The transformation involves the energy level shift in the ${}^3P_0$-orbital: $\varepsilon_f \equiv \varepsilon_f^{(0)} - \omega$ as depicted in Fig. 2.1 (b), which comes from the time-derivative term in the Lagrangian.

2 Slave boson theory

To analyze the Kondo effect arising from the Hamiltonian $\mathcal{H}$, we employ the slave-boson mean-field theory (Sec. 2.3 in the previous chapter) which becomes exact in $N \to \infty$ limit ($N = 2I + 1$ is the number of spin components). As the first approximation, we take the strong-correlation limit $U \to \infty$ and neglect double occupancy of the ${}^3P_0$ state. Next, we split the f operators into $f'_{i\sigma} = b_i^\dagger \tilde{f}_{i\sigma}$ by introducing a slave-boson operator b_i, with a constraint $\sum_\sigma \tilde{f}^\dagger_{i\sigma} \tilde{f}_{i\sigma} + b_i^\dagger b_i = 1$ at each site. To impose the constraint, the Lagrange multiplier field λ_i is added to the Hamiltonian. Although the slave boson theory is explained using the Matsubara formalism in the previous chapter, here we use the real-time field theory referred to as Keldysh formalism [172], keeping the time-dependence of the system explicitly. Our action in the slave-boson representation is

$$S = \int_C \mathrm{d}t (\mathcal{L}_0 + \mathcal{L}_{\rm mix}),$$

$$\mathcal{L}_0 = \sum_{\boldsymbol{k},\sigma} c^\dagger_{\boldsymbol{k}\sigma} (i\partial_t - \varepsilon_c(\boldsymbol{k})) c_{\boldsymbol{k}\sigma} + \sum_{i,\sigma} \tilde{f}^\dagger_{i\sigma} (i\partial_t - \varepsilon_f) \tilde{f}_{i\sigma} + \sum_i b_i^\dagger i\partial_t b_i - \sum_i \lambda_i \Big(\sum_\sigma \tilde{f}^\dagger_{i\sigma} \tilde{f}_{i\sigma} + b_i^\dagger b_i - 1 \Big),$$

$$\mathcal{L}_{\rm mix} = -\sum_{i,\sigma,\sigma'} (\boldsymbol{V} \cdot \boldsymbol{\sigma}_{\sigma\sigma'} \tilde{f}^\dagger_{i\sigma} b_i c_{i\sigma'} + \text{h.c.}).$$

$C = C_+ \cup C_-$ denotes the Keldysh contour [172], which is the sum of two contours from $t = 0$ to $t = \infty$ and from $t = \infty$ to $t = 0$. We denote a field on the contour C_+ and C_- as $\varphi_+(t)$ and $\varphi_-(t)$, respectively ($\varphi = c, \tilde{f}, b, \lambda$). Thanks to the doubling of the fields, this field theory contains full

information of real-time correlators of the system, especially the Green's functions. For convenience, we introduce the Keldysh rotation of each field: for bosons,

$$\begin{pmatrix}\chi_1(t)\\ \chi_2(t)\end{pmatrix} \equiv \frac{1}{\sqrt{2}}\begin{pmatrix}1 & 1\\ 1 & -1\end{pmatrix}\begin{pmatrix}\chi_+(t)\\ \chi_-(t)\end{pmatrix}, \begin{pmatrix}\chi_1^\dagger(t)\\ \chi_2^\dagger(t)\end{pmatrix} \equiv \frac{1}{\sqrt{2}}\begin{pmatrix}1 & 1\\ 1 & -1\end{pmatrix}\begin{pmatrix}\chi_+^\dagger(t)\\ \chi_-^\dagger(t)\end{pmatrix}$$

and for fermions,

$$\begin{pmatrix}\psi_1(t)\\ \psi_2(t)\end{pmatrix} \equiv \frac{1}{\sqrt{2}}\begin{pmatrix}1 & 1\\ 1 & -1\end{pmatrix}\begin{pmatrix}\psi_+(t)\\ \psi_-(t)\end{pmatrix}, \begin{pmatrix}\psi_1^\dagger(t)\\ \psi_2^\dagger(t)\end{pmatrix} \equiv \frac{1}{\sqrt{2}}\begin{pmatrix}1 & -1\\ 1 & 1\end{pmatrix}\begin{pmatrix}\psi_+^\dagger(t)\\ \psi_-^\dagger(t)\end{pmatrix},$$

where the convention of Ref. [172] is used. After the Keldysh rotation, the action turns into

$$S = S_c + S_f + S_b + S_{\rm mix} + \sqrt{2}\sum_i \lambda_{2i},$$

$$S_c = \int_0^\infty {\rm d}t \sum_{\boldsymbol{k},\sigma} (c_{1\boldsymbol{k}\sigma}^\dagger, c_{2\boldsymbol{k}\sigma}^\dagger)\begin{pmatrix} i\partial_t - \varepsilon_c(\boldsymbol{k}) & 0\\ 0 & i\partial_t - \varepsilon_c(\boldsymbol{k})\end{pmatrix}\begin{pmatrix}c_{1\boldsymbol{k}\sigma}\\ c_{2\boldsymbol{k}\sigma}\end{pmatrix},$$

$$S_f = \int_0^\infty {\rm d}t \sum_{i,\sigma} (\tilde{f}_{1i\sigma}^\dagger, \tilde{f}_{2i\sigma}^\dagger)\begin{pmatrix} i\partial_t - \varepsilon_f - \lambda_{1i}/\sqrt{2} & -\lambda_{2i}/\sqrt{2}\\ -\lambda_{2i}/\sqrt{2} & i\partial_t - \varepsilon_f - \lambda_{1i}/\sqrt{2}\end{pmatrix}\begin{pmatrix}\tilde{f}_{1i\sigma}\\ \tilde{f}_{2i\sigma}\end{pmatrix},$$

$$S_b = \int_0^\infty {\rm d}t \sum_{i} (b_{1i}^\dagger, b_{2i}^\dagger)\begin{pmatrix} -\lambda_{2i}/\sqrt{2} & i\partial_t - \lambda_{1i}/\sqrt{2}\\ i\partial_t - \lambda_{1i}/\sqrt{2} & -\lambda_{2i}/\sqrt{2}\end{pmatrix}\begin{pmatrix}b_{1i}\\ b_{2i}\end{pmatrix},$$

$$S_{\rm mix} = \int_0^\infty {\rm d}t \frac{-1}{\sqrt{2}} \sum_{i,\sigma,\sigma'} \Big\{ \boldsymbol{V}\cdot\boldsymbol{\sigma}_{\sigma\sigma'} \tilde{f}_{1i\sigma}^\dagger (b_{1i}c_{1i\sigma'} + b_{2i}c_{2i\sigma'}) + \boldsymbol{V}\cdot\boldsymbol{\sigma}_{\sigma\sigma'} \tilde{f}_{2i\sigma}^\dagger (b_{2i}c_{1i\sigma'} + b_{1i}c_{2i\sigma'}) + {\rm h.c.}\Big\}.$$

The partition function is

$$\begin{aligned} Z &= \int \mathcal{D}[c, \tilde{f}, b, \lambda] e^{iS} \\ &\equiv \int \mathcal{D}[b, \lambda] e^{iS_{\rm eff}}. \end{aligned}$$

In the second line, we integrate out the fermions and define the effective bosonic action $S_{\rm eff}$. The saddle-point condition of the path integral is obtained by

$$\begin{aligned} \frac{\delta S_{\rm eff}}{\delta b_{\alpha i}(t)} &= \Big\langle \frac{\delta S}{\delta b_{\alpha i}(t)} \Big\rangle = 0, \\ \frac{\delta S_{\rm eff}}{\delta \lambda_{\alpha i}(t)} &= \Big\langle \frac{\delta S}{\delta \lambda_{\alpha i}(t)} \Big\rangle = 0 \end{aligned}$$

with $\alpha = 1, 2$, where $\langle \cdots \rangle$ is the expectation value with fixed $b_{\alpha i}$ and $\lambda_{\alpha i}$. These lead to

$$(i\partial_t - \frac{\lambda_{1i}}{\sqrt{2}}) b_{2i}(t) - \frac{\lambda_{2i}}{\sqrt{2}} b_{1i}(t) - \frac{1}{\sqrt{2}} \sum_{i,\sigma,\sigma'} (\boldsymbol{V}\cdot\boldsymbol{\sigma}_{\sigma\sigma'})^* (\langle c_{1i\sigma'}^\dagger(t) \tilde{f}_{1i\sigma}(t)\rangle + \langle c_{2i\sigma'}^\dagger(t) \tilde{f}_{2i\sigma}(t)\rangle) = 0,$$

$$(i\partial_t - \frac{\lambda_{1i}}{\sqrt{2}}) b_{1i}(t) - \frac{\lambda_{2i}}{\sqrt{2}} b_{2i}(t) - \frac{1}{\sqrt{2}} \sum_{i,\sigma,\sigma'} (\boldsymbol{V}\cdot\boldsymbol{\sigma}_{\sigma\sigma'})^* (\langle c_{2i\sigma'}^\dagger(t) \tilde{f}_{1i\sigma}(t)\rangle + \langle c_{1i\sigma'}^\dagger(t) \tilde{f}_{2i\sigma}(t)\rangle) = 0,$$

$$\sum_\sigma (\langle \tilde{f}_{1i\sigma}^\dagger(t) \tilde{f}_{1i\sigma}(t)\rangle + \langle \tilde{f}_{2i\sigma}^\dagger(t) \tilde{f}_{2i\sigma}(t)\rangle) + b_{1i}^\dagger(t) b_{2i}(t) + b_{2i}^\dagger(t) b_{1i}(t) = 0,$$

$$\sum_\sigma (\langle \tilde{f}_{1i\sigma}^\dagger(t) \tilde{f}_{2i\sigma}(t)\rangle + \langle \tilde{f}_{2i\sigma}^\dagger(t) \tilde{f}_{1i\sigma}(t)\rangle) + b_{1i}^\dagger(t) b_{1i}(t) + b_{2i}^\dagger(t) b_{2i}(t) - 2 = 0.$$

After the gauge transformation, the Hamiltonian at $t > 0$ is time-independent. Thus, instead of solving the full time-dependent mean-field theory, we here focus on the steady state after a long time and simply assume that the steady state is a thermal equilibrium state described by an effective temperature T and a chemical potential μ. Since the external driving leads to heating of the system, the temperature T and the chemical potential μ after the application of the laser are different from T_0 and μ_0. The Kondo effect occurs below the Kondo temperature T_K. If the effective temperature T exceeds the Kondo temperature, the Kondo effect is washed out by the heating. To address the effect of heating by the application of the laser, we evaluate T and μ using the energy conservation law and the particle number conservation law, since the atoms are trapped in vacuum and well isolated from the environment.

For simplicity, we set a homogeneous ansatz for the mean-field solution, neglecting the effect of the trap potential to atoms. Then, the set of saddle-point conditions in the steady state can be simplified as

$$\lambda_1 b_2 + \lambda_2 b_1 + \frac{1}{N_s}\sum_{\boldsymbol{k},\sigma,\sigma'} (\boldsymbol{V}\cdot\boldsymbol{\sigma}_{\sigma\sigma'})^* (\langle c^\dagger_{1\boldsymbol{k}\sigma'}(t)\tilde{f}_{1\boldsymbol{k}\sigma}(t)\rangle + \langle c^\dagger_{2\boldsymbol{k}\sigma'}(t)\tilde{f}_{2\boldsymbol{k}\sigma}(t)\rangle) = 0, \tag{2.2.1}$$

$$\lambda_1 b_1 + \lambda_2 b_2 + \frac{1}{N_s}\sum_{\boldsymbol{k},\sigma,\sigma'} (\boldsymbol{V}\cdot\boldsymbol{\sigma}_{\sigma\sigma'})^* (\langle c^\dagger_{2\boldsymbol{k}\sigma'}(t)\tilde{f}_{1\boldsymbol{k}\sigma}(t)\rangle + \langle c^\dagger_{1\boldsymbol{k}\sigma'}(t)\tilde{f}_{2\boldsymbol{q}\sigma}(t)\rangle) = 0, \tag{2.2.2}$$

$$\frac{1}{N_s}\sum_{\boldsymbol{k},\sigma} (\langle \tilde{f}^\dagger_{1\boldsymbol{k}\sigma}(t)\tilde{f}_{1\boldsymbol{k}\sigma}(t)\rangle + \langle \tilde{f}^\dagger_{2\boldsymbol{k}\sigma}(t)\tilde{f}_{2\boldsymbol{k}\sigma}(t)\rangle) + b_1^\dagger b_2 + b_2^\dagger b_1 = 0, \tag{2.2.3}$$

$$\frac{1}{N_s}\sum_{\boldsymbol{k},\sigma} (\langle \tilde{f}^\dagger_{1\boldsymbol{k}\sigma}(t)\tilde{f}_{2\boldsymbol{k}\sigma}(t)\rangle + \langle \tilde{f}^\dagger_{2\boldsymbol{k}\sigma}(t)\tilde{f}_{1\boldsymbol{k}\sigma}(t)\rangle) + b_1^\dagger b_1 + b_2^\dagger b_2 - 2 = 0. \tag{2.2.4}$$

We note that Eqs. (2.2.1) and (2.2.3) are identically satisfied when we set $b_2 = \lambda_2 = 0$ because of the relation between the retarded and advanced Green's function: $G^R(t,t) + G^A(t,t) = 0$ (See also Ref. [173]). Hence, we arrive at the saddle-point conditions:

$$-\lambda_1 b_1 - \sum_{\boldsymbol{k},\sigma,\sigma'} (\boldsymbol{V}\cdot\boldsymbol{\sigma}_{\sigma\sigma'})^* \langle c^\dagger_{2\boldsymbol{k}\sigma'}(t)\tilde{f}_{1\boldsymbol{k}\sigma}(t)\rangle = 0, \tag{2.2.5}$$

$$\sum_{\boldsymbol{k},\sigma} \langle \tilde{f}^\dagger_{2\boldsymbol{k}\sigma}(t)\tilde{f}_{1\boldsymbol{k}\sigma}(t)\rangle + b_1^\dagger b_1 - 2N_s = 0. \tag{2.2.6}$$

Using the relation $\langle c^\dagger_{2\boldsymbol{k}\sigma'}(t)\tilde{f}_{1\boldsymbol{k}\sigma}(t)\rangle = iG^K_{fc,\boldsymbol{k}\sigma\sigma'}(t,t)$ and $\langle \tilde{f}^\dagger_{2\boldsymbol{k}\sigma}(t)\tilde{f}_{1\boldsymbol{k}\sigma}(t)\rangle = 1 - iG^K_{ff,\boldsymbol{k}\sigma\sigma}(t,t) = 2iG^<_{ff,\boldsymbol{k}\sigma\sigma}(t,t)$, the saddle-point conditions can be rewritten as

$$\tilde{V}(\tilde{\varepsilon}_f - \varepsilon_f) + \frac{V^2}{2N_s}\sum_{\boldsymbol{k},\sigma,\sigma'} (\hat{\boldsymbol{V}}\cdot\boldsymbol{\sigma}_{\sigma\sigma'})^* iG^K_{fc,\boldsymbol{k}\sigma\sigma'}(t,t) = 0, \tag{2.2.7}$$

$$\frac{1}{N_s}\sum_{\boldsymbol{k},\sigma} iG^<_{ff,\boldsymbol{k}\sigma\sigma}(t,t) + \Big(\frac{\tilde{V}}{V}\Big)^2 - 1 = 0, \tag{2.2.8}$$

where $G^<_{ff,\boldsymbol{k}\sigma\sigma}(t,t') = i\langle \tilde{f}^\dagger_{\boldsymbol{k}\sigma}(t)\tilde{f}_{\boldsymbol{k}\sigma}(t')\rangle$ and $G^K_{fc,\boldsymbol{k}\sigma\sigma'}(t,t') = -i\langle[\tilde{f}_{\boldsymbol{k}\sigma}(t), c^\dagger_{\boldsymbol{k}\sigma'}(t')]\rangle$ are the lesser and Keldysh components of Green's function, respectively [172]. N_s denotes the number of sites. The mean fields b and λ (here we have dropped the site indices) are incorporated in the renormalized hybridization $\tilde{\boldsymbol{V}} \equiv \boldsymbol{V}b_1/\sqrt{2N_s}$ and the renormalized energy level $\tilde{\varepsilon}_f \equiv \varepsilon_f + \lambda_1/\sqrt{2N_s}$. These

renormalization effects are the manifestation of the strong correlation arising from the Kondo effect. We set $V = |\boldsymbol{V}|, \tilde{V} = |\tilde{\boldsymbol{V}}|$ and $\hat{\boldsymbol{V}} = \boldsymbol{V}/|\boldsymbol{V}|$.

We must determine the temperature T and the chemical potential μ at the steady state. Thus the rest of self-consistent equations consists of the energy conservation and the particle number conservation. These read

$$\begin{aligned}
&\sum_{\boldsymbol{k},\sigma}(\varepsilon_c(\boldsymbol{k})\langle c^\dagger_{\boldsymbol{k}\sigma}c_{\boldsymbol{k}\sigma}\rangle_{\rm ini} + \varepsilon_f\langle f^\dagger_{\boldsymbol{k}\sigma}f_{\boldsymbol{k}\sigma}\rangle_{\rm ini}) \\
=&\sum_{\boldsymbol{k},\sigma}(\varepsilon_c(\boldsymbol{k})\langle c^\dagger_{\boldsymbol{k}\sigma}(t)c_{\boldsymbol{k}\sigma}(t)\rangle + \tilde{\varepsilon}_f\langle \tilde{f}^\dagger_{\boldsymbol{k}\sigma}(t)\tilde{f}_{\boldsymbol{k}\sigma}(t)\rangle) + \sum_{\boldsymbol{k},\sigma,\sigma}(\tilde{\boldsymbol{V}}\cdot\boldsymbol{\sigma}_{\sigma\sigma'}\langle \tilde{f}^\dagger_{\boldsymbol{k}\sigma}(t)c_{\boldsymbol{k}\sigma'}(t)\rangle + \text{h.c.}) + \sum_i \lambda_i(|b_i|^2-1),
\end{aligned} \tag{2.2.9}$$

$$\sum_{\boldsymbol{k},\sigma}(\langle c^\dagger_{\boldsymbol{k}\sigma}c_{\boldsymbol{k}\sigma}\rangle_{\rm ini} + \langle f^\dagger_{\boldsymbol{k}\sigma}f_{\boldsymbol{k}\sigma}\rangle_{\rm ini}) = \sum_{\boldsymbol{k},\sigma}(\langle c^\dagger_{\boldsymbol{k}\sigma}(t)c_{\boldsymbol{k}\sigma}(t)\rangle + \langle f^\dagger_{\boldsymbol{k}\sigma}(t)f_{\boldsymbol{k}\sigma}(t)\rangle), \tag{2.2.10}$$

where $\langle\cdots\rangle_{\rm ini}$ is the expectation value for the initial state, namely $\langle c^\dagger_{\boldsymbol{k}\sigma}c_{\boldsymbol{k}\sigma}\rangle_{\rm ini} = f(\varepsilon_c(\boldsymbol{k}))$ and $\sum_{\boldsymbol{k},\sigma}\langle f^\dagger_{\boldsymbol{k}\sigma}f_{\boldsymbol{k}\sigma}\rangle_{\rm ini} = 1$ ($f(\varepsilon)$ is the Fermi distribution function).

To calculate the mean-field equations, we use the Green's functions of the mean-field Hamiltonian. Here we assume that the laser has π-polarization $\boldsymbol{V} = (0,0,V)$. For the π-polarized laser, the Green's functions can be easily calculated. These reads

$$\begin{aligned}
G^<_{cc,\boldsymbol{k}\sigma\sigma}(t,t') &= i\langle c^\dagger_{\boldsymbol{k}\sigma}(t')c_{\boldsymbol{k}\sigma}(t)\rangle \\
&= i|u_{\boldsymbol{k}\sigma}|^2 f(\varepsilon_{\sigma+}(\boldsymbol{k}))e^{-i\varepsilon_{\sigma+}(\boldsymbol{k})(t-t')} + i|v_{\boldsymbol{k}\sigma}|^2 f(\varepsilon_{\sigma-}(\boldsymbol{k}))e^{-i\varepsilon_{\sigma-}(\boldsymbol{k})(t-t')} \\
G^<_{ff,\boldsymbol{k}\sigma\sigma}(t,t') &= i\langle \tilde{f}^\dagger_{\boldsymbol{k}\sigma}(t')\tilde{f}_{\boldsymbol{k}\sigma}(t)\rangle \\
&= i|v_{\boldsymbol{k}\sigma}|^2 f(\varepsilon_{\sigma+}(\boldsymbol{k}))e^{-i\varepsilon_{\sigma+}(\boldsymbol{k})(t-t')} + i|u_{\boldsymbol{k}\sigma}|^2 f(\varepsilon_{\sigma-}(\boldsymbol{k}))e^{-i\varepsilon_{\sigma-}(\boldsymbol{k})(t-t')}, \\
G^<_{fc,\boldsymbol{k}\sigma\sigma}(t,t') &= i\langle c^\dagger_{\boldsymbol{k}\sigma}(t')\tilde{f}_{\boldsymbol{k}\sigma}(t)\rangle \\
&= iu_{\boldsymbol{k}\sigma}v^*_{\boldsymbol{k}\sigma} f(\varepsilon_{\sigma+}(\boldsymbol{k}))e^{-i\varepsilon_{\sigma+}(\boldsymbol{k})(t-t')} - iu_{\boldsymbol{k}\sigma}v^*_{\boldsymbol{k}\sigma} f(\varepsilon_{\sigma-}(\boldsymbol{k}))e^{-i\varepsilon_{\sigma-}(\boldsymbol{k})(t-t')},
\end{aligned}$$

and

$$\begin{aligned}
G^K_{fc,\boldsymbol{k}\sigma\sigma}(t,t') = &-iu_{\boldsymbol{k}\sigma}v^*_{\boldsymbol{k}\sigma}(1-2f(\varepsilon_{\sigma+}(\boldsymbol{k})))e^{-i\varepsilon_{\sigma+}(\boldsymbol{k})(t-t')} \\
&+ iu_{\boldsymbol{k}\sigma}v^*_{\boldsymbol{k}\sigma}(1-2f(\varepsilon_{\sigma-}(\boldsymbol{k})))e^{-i\varepsilon_{\sigma-}(\boldsymbol{k})(t-t')},
\end{aligned}$$

where

$$\begin{aligned}
&u_{\boldsymbol{k}\sigma} = \sqrt{\frac{1}{2}\Big(1+\frac{\varepsilon_c(\boldsymbol{k})-\tilde{\varepsilon}_f}{E_\sigma(\boldsymbol{k})}\Big)}, v_{\boldsymbol{k}\sigma} = \sqrt{\frac{1}{2}\Big(1-\frac{\varepsilon_c(\boldsymbol{k})-\tilde{\varepsilon}_f}{E_\sigma(\boldsymbol{k})}\Big)}, \\
&\varepsilon_{\sigma\pm}(\boldsymbol{k}) = \frac{\varepsilon_c(\boldsymbol{k})-\tilde{\varepsilon}_f \pm E_\sigma(\boldsymbol{k})}{2}, \\
&E_\sigma(\boldsymbol{k}) = \sqrt{(\varepsilon_c(\boldsymbol{k})-\tilde{\varepsilon}_f)^2 + 4|\sigma\tilde{V}|^2}.
\end{aligned}$$

In the equilibrium state, the saddle point conditions (2.2.7) and (2.2.8) have the same form as that derived using standard Matsubara formalism [28, 174]. In the slave boson theory, the Kondo

temperature T_K is defined by the temperature where the slave boson starts to have a non-zero expectation value in thermal equilibrium [175]. Thus the Kondo temperature is obtained by setting $b_1 = 0$ and $T = T_K$ in Eqs. (2.2.7) and (2.2.8). First, using Eq. (2.2.8), we obtain

$$\tilde{\varepsilon}_f|_{T=T_K} = \mu + T_K \log(N-1)$$

because of the condition $Nf(\tilde{\varepsilon}_f) = 1$. Substituting this into Eq. (2.2.5), and using the constant density of states $\rho(\varepsilon) = \rho_0 = 1/(2D), -D \le \varepsilon \le D$, we arrive at

$$T_K = c_N (D-\mu)^{1/N} (D+\mu)^{1-1/N} \exp\Big[\frac{\varepsilon_f - \mu}{A_N \rho_0 V^2}\Big],$$

where

$$A_N \equiv \frac{N(N^2-1)}{12},$$
$$\log c_N \equiv -(N-1)\int_0^\infty \mathrm{d}x \log x \cdot \Big\{ \frac{e^x}{((N-1)e^x+1)^2} + \frac{e^{-x}}{((N-1)e^{-x}+1)^2} \Big\}.$$

3 Laser-induced Kondo effect

The self-consistent equations are solved numerically. In the numerical calculation, we assume that the laser has π-polarization $\boldsymbol{V} = (0, 0, V)$, and that the density of states of the ${}^1S_0$-orbital is constant with finite bandwidth: $\rho(\varepsilon) = \rho_0 = 1/(2D), -D \le \varepsilon \le D$. Figures 2.1 (c) and (d) show the numerical solutions of the self-consistent equations starting from the zero-temperature initial state. The non-zero value of the renormalized hybridization, which entangles the localized ${}^3P_0$ atoms with the ${}^1S_0$ cloud, signals the emergence of the Kondo effect under the photo-irradiation. The strongly renormalized value of $\tilde{V}$ leads to a hybridized band with a narrow Kondo gap and thus realizes a heavy-fermion liquid. The effective temperature (Fig. 2.1 (d)) is increased due to the heating effect caused by the irradiation. An important point is that *the effective temperature is always lower than the Kondo temperature* T_K, and thus the Kondo effect can be realized. If the Fermi temperature is of the order of 100 nK, the necessary laser strength (or Rabi frequency) is estimated to be a few kHz, which is an achievable value in experiments.

We note that AEA can offer a system with large-N spin components, where $N = 6$ (i.e. $I = 5/2$) for ^{173}Yb and $N = 10$ ($I = 9/2$) for ^{87}Sr. The Kondo temperature, which is the underlying energy scale of the Kondo physics, rapidly increases with the number of components N. This means that the Kondo state is more stable in large-N systems, and makes the observation of the Kondo effect more feasible in the large spin state with AEA.

We also comment on a role of the trap potential. Since the trap potential reduces $\varepsilon_f - \mu$, T_K is lowest at the trap center, and there should appear a "mixed valence" region where $\varepsilon_f \lesssim \mu$ and the Kondo temperature is quite high. The existence of that region supports the feasibility to realize the Kondo liquid. However, we note that since the renormalization effect is weak in the mixed valence regime, a sharp Kondo effect may appear near the trap center.

Next, we show numerical results for the case where the initial states are at finite temperatures. Figure 2.2 shows the numerical solutions of the mean-field equations at finite initial temperatures. In this case, the laser-induced Kondo effect emerges above some threshold value of laser strength, since the Kondo effect cannot appear in the region where $T_K < T_0$. When the optical coupling is weak, the photo-induced hybridization between the orbitals is washed out due to the thermal

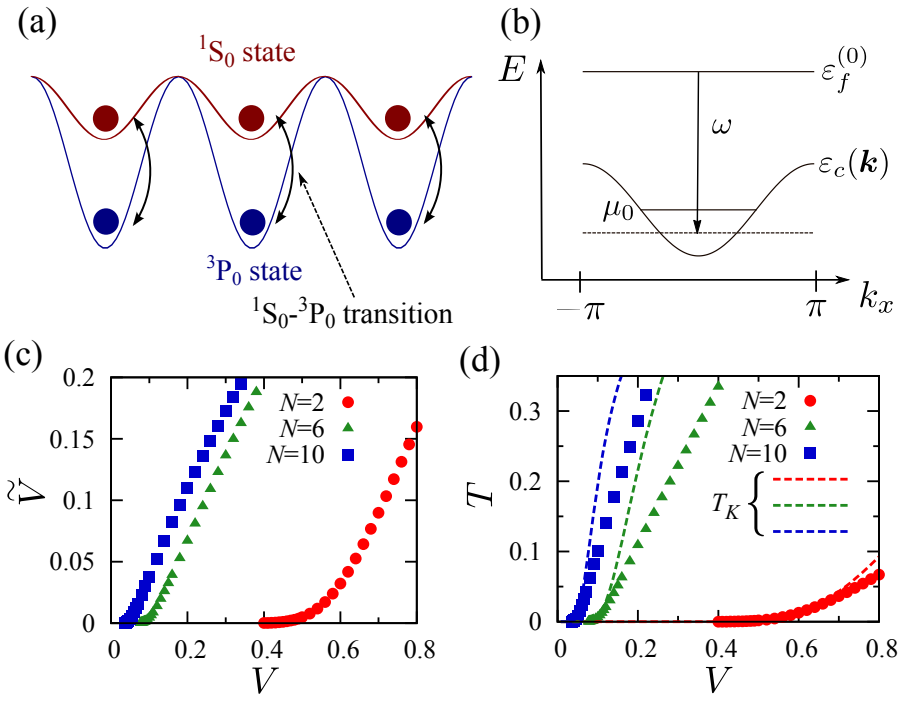

Figure 2.1: (a) Schematic picture of the setup. Fermionic atoms in the $^1S_0$ state can move between sites of the optical lattice, while those in the $^3P_0$ state cannot. (b) The energy level shift after the gauge transformation. (c) Renormalized hybridization calculated with parameters $D = 1, \varepsilon_f = -0.5, T_0 = 0, \mu_0 = -0.1$ and $N = 2, 6, 10$. (d) Effective temperatures calculated with the same parameters. The broken lines show the Kondo temperature T_K.

fluctuations. With sufficiently strong laser fields, the two orbitals start to entangle and show the Kondo effect. As we increase the laser strength, the thermal fluctuations become less important, and the solutions approach the case of zero initial temperatures.

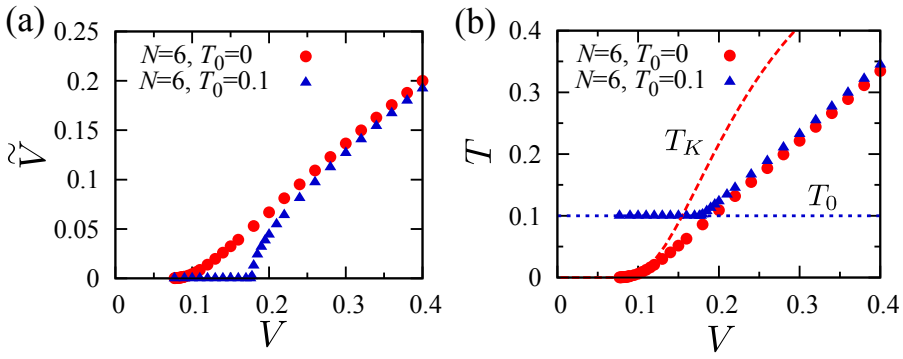

Figure 2.2: Solutions of the mean-field equations starting from finite initial temperatures, with parameters $D = 1, \varepsilon_f = -0.5, T_0 = 0.1, \mu_0 = -0.1$ and $N = 6$. The solutions at zero initial temperature is also shown for comparison. (a) Renormalized hybridization. (b) Effective temperature. The broken line shows the Kondo temperature, and the horizontal dotted line is the initial temperature.

4 Spin-selective renormalization

The laser-induced Kondo state shows peculiar features owing to interplay between the optical coupling and the multicomponent spin structure of AEA. In particular, the spin-dependent optical coupling leads to intriguing consequences with the Kondo state. The optical coupling for the π-polarized light becomes $\boldsymbol{V} \cdot \boldsymbol{\sigma}_{\sigma\sigma'} = \sigma V \delta_{\sigma\sigma'}$ and explicitly breaks the spin SU(N)-invariance. Therefore, the laser-driven Kondo gaps are spin-dependent, as seen in the quasiparticle band structure $\varepsilon_{\sigma\pm}(\boldsymbol{k}) = \frac{1}{2}(\varepsilon_c(\boldsymbol{k}) + \tilde{\varepsilon}_f \pm \sqrt{(\varepsilon_c(\boldsymbol{k}) - \tilde{\varepsilon}_f)^2 + 4|\sigma\tilde{V}|^2})$ (illustrated in Fig. 2.3 (a)) which is obtained by diagonalizing the mean-field Hamiltonian. This gives rise to spin-dependent effective masses of quasiparticles, since the quasiparticle band is more flattened in the higher spin components at the Fermi energy. As a result, the laser-induced Kondo effect selectively renormalizes the effective masses of higher spin components, beside light quasiparticles of lower spin components. These consequences are in marked contrast to the SU(N)-symmetric Kondo effect proposed for ultracold atoms previously [150, 176, 177, 178, 179, 180], where the all spin components are completely degenerate.

These characteristic spin-dependent structures are reflected in physical observables. The spin-dependent quasiparticle band yields population imbalance between the spin components. In Fig. 2.3 (b), we have plotted the population imbalance. The population imbalance, which can be directly measured by cold-atom experiments, inherits both the spin-dependent nature and nonperturbative V-dependence in the laser-induced Kondo effect. The Kondo states can also be measured by density profiles of the atomic cloud. For $N = 2$, and when the $^1S_0$-orbital is half-filled in the lattice, the lower hybridized band formed by the Kondo effect is completely filled: this phase is called the Kondo insulator. Reflecting the formation of the Kondo insulator, a density plateau of the atomic cloud appears in some region of the atomic cloud [177, 178]. Similarly, in the case of $N > 2$, reflecting the spin-dependent Kondo gaps, a half-metallic phase composed of a completely filled band (the Kondo

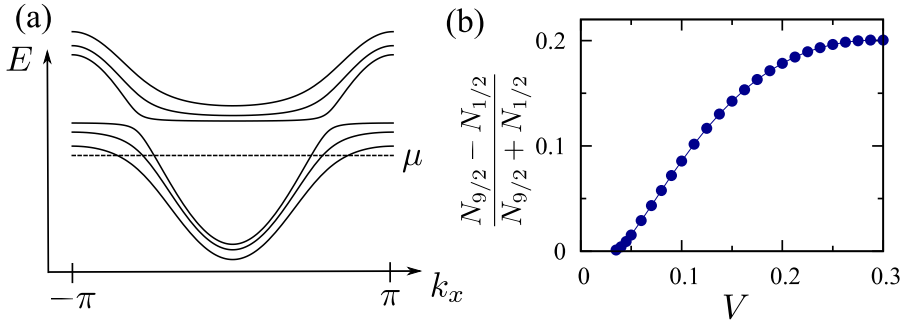

Figure 2.3: (a) The renormalized quasiparticle band induced by the laser-induced Kondo effect for $N = 6$. (b) Population imbalance induced by the Kondo effect. $N = 10$ case is shown, with parameters $D = 1, \varepsilon_f = -0.8, T_0 = 0, \mu_0 = -0.5$. $N_\sigma = n_\sigma + n_{-\sigma}$ is the particle number of each spin component.

insulator) and partially filled Kondo metals can be formed. Correspondingly the density plateau may also be spin-dependent for $N > 2$.

5 Effect of spin-exchange interactions

So far we have described the laser-induced Kondo effect using the minimal Hamiltonian $\mathcal{H}_0 + \mathcal{H}_{\mathrm{mix}}$, which includes only interactions between the ${}^3P_0$ states. In reality, other interactions also exist [150]. Among them, strong interorbital SU(N) exchange interactions observed in experiments [157, 158, 163] play the most crucial role for the Kondo physics. Here we consider how these interactions affect the laser-induced Kondo effect. The model Hamiltonian can be written in the most general form as [150, 181]

$$\begin{aligned} H = & \sum_{\langle i,j\rangle,\sigma} (-t_c c^\dagger_{i\sigma} c_{j,\sigma} - t_f f^\dagger_{i\sigma} f_{j,\sigma} + \mathrm{h.c.}) + \sum_{j,\sigma} \varepsilon_f^{(0)} n_{fj\sigma} \\ & + U \sum_{j,\sigma<\sigma'} n_{cj\sigma} n_{cj\sigma'} + U_{ff} \sum_{j,\sigma<\sigma'} n_{fj\sigma} n_{fj\sigma'} \\ & + U_{cf} \sum_{j,\sigma,\sigma'} n_{cj\sigma} n_{fj\sigma'} + V_{\mathrm{ex}} \sum_{j,\sigma,\sigma'} c^\dagger_{j\sigma} f^\dagger_{j\sigma'} c_{j\sigma'} f_{j\sigma} \\ & + \sum_{j,\sigma,\sigma'} (\boldsymbol{V} \cdot \boldsymbol{\sigma}_{\sigma\sigma'} e^{i\boldsymbol{K}\cdot\boldsymbol{R}_j - i\omega t} f^\dagger_{j\sigma} c_{j\sigma'} + \mathrm{h.c.}), \end{aligned} \tag{2.5.1}$$

where $n_{cj\sigma} = c^\dagger_{j\sigma} c_{j\sigma}$ and $n_{fj\sigma} = f^\dagger_{j\sigma} f_{j\sigma}$ count the number of particles at site j. $\varepsilon_f^{(0)}$ denotes the excitation energy of the ${}^3P_0$ state from the ${}^1S_0$ state. The specific values of interaction parameters $U, U_{ff}, U_{cf}, V_{\mathrm{ex}}$ depend on s-wave scattering lengths in corresponding collision channels and the Wannier-function overlaps. Since the s-wave scattering lengths are independent of the nuclear spin states, the interactions possess SU($N = 2I + 1$) symmetry [150, 151]. Here V_{ex} denotes the SU(N) exchange interaction. We assume that $U > 0, U_{ff} > 0$. In principle, there exist additional terms originating from a magnetic field [182], but for simplicity we take the zero-field limit and avoid the complication. As shown in Sec. 1, the explicit time dependence in the hybridization term of Eq.

(4.4.1) is eliminated by the gauge transformation $f_{j\sigma} \to e^{-i\omega t} f_{j\sigma}$. After this transformation, the energy level of the ${}^3P_0$ state is effectively shifted, and we replace $\varepsilon_f^{(0)}$ with $\varepsilon_f \equiv \varepsilon_f^{(0)} - \omega$. Also, we assume that the lattice potential is sufficiently deep for the ${}^3P_0$ state to suppress inelastic collisions which cause loss of atoms, and thus $t_f \ll U_{ff}$. On the other hand, the lattice potential for the ${}^1S_0$ state is shallow to allow the hopping between sites.

To simplify the original model (4.4.1), we consider a limiting case in which the Kondo limit is achieved: $\varepsilon_f \ll \mu \ll \varepsilon_f + U_{ff}$ and $|\boldsymbol{V}|$ is sufficiently small. In this case, since the occupation number of the ${}^3P_0$ state in low-energy states is one at each site, we can restrict ourselves to the Hilbert subspace with $\sum_\sigma n_{fj\sigma} = 1$ and derive an effective low-energy Hamiltonian using the Schrieffer-Wolff transformation in a similar way as Sec. 2.2 in Chap. 1. The resulting low-energy theory leads to

$$\begin{aligned} H_{\text{eff}} =& -t_c \sum_{\langle i,j\rangle,\sigma} (c_{i\sigma}^\dagger c_{j,\sigma} + \text{h.c.}) + U \sum_{j,\sigma<\sigma'} n_{cj\sigma} n_{cj\sigma'} \\ &+ \sum_{j,\sigma,\sigma'} (V_{\text{ex}} - \sigma\sigma' J) c_{j\sigma}^\dagger f_{j\sigma'}^\dagger c_{j\sigma'} f_{j\sigma} \\ &+ J_H \sum_{\langle i,j\rangle,\sigma,\sigma'} f_{i\sigma}^\dagger f_{i\sigma'} f_{j,\sigma'}^\dagger f_{j,\sigma} \end{aligned} \tag{2.5.2}$$

where $J = 2V^2(\frac{1}{|\varepsilon_f - \mu|} + \frac{1}{\varepsilon_f - \mu + U_{ff}}) > 0$ and $J_H = 4t_f^2/U_{ff} > 0$. We note that when $\sum_\sigma n_{fj\sigma} = 1$, the interaction U_{cf} can be incorporated into the chemical potential and therefore we omit this term from H_{eff}.

The effective Hamiltonian (2.5.2) contains an effective Kondo interaction V_{ex}, J between the two orbitals and the Heisenberg interaction J_H between ${}^3P_0$ states. While the spin-exchanging collision V_{ex} is fully symmetric, the optically induced Kondo coupling J breaks the spin SU(N) symmetry due to the polarization-spin coupling in the last term in Eq. (2.5.1). For general N, this Kondo coupling is somewhat complicated, but the case of $N = 2$ is simple. For $N = 2$, we can rewrite the Kondo coupling as

$$\begin{aligned} &\sum_{j,\sigma,\sigma'} (V_{\text{ex}} - \sigma\sigma' J) c_{j\sigma}^\dagger f_{j\sigma'}^\dagger c_{j\sigma'} f_{j\sigma} \\ =& -J_\perp \sum_j (S_{cj}^x S_{fj}^x + S_{cj}^y S_{fj}^y) - J_z \sum_j S_{cj}^z S_{fj}^z \\ &+ \text{potential term}, \end{aligned} \tag{2.5.3}$$

where

$$J_\perp \equiv V_{\text{ex}} + J/4, \tag{2.5.4a}$$

$$J_z \equiv V_{\text{ex}} - J/4. \tag{2.5.4b}$$

The "potential term" can be absorbed into the chemical potential. The spin operators are defined by $\boldsymbol{S}_{cj} = \frac{1}{2}\sum_{\sigma,\sigma'} c_{j\sigma}^\dagger \boldsymbol{\sigma}_{\sigma\sigma'} c_{j\sigma'}$ and $\boldsymbol{S}_{fj} = \frac{1}{2}\sum_{\sigma,\sigma'} f_{j\sigma}^\dagger \boldsymbol{\sigma}_{\sigma\sigma'} f_{j\sigma'}$, where $\boldsymbol{\sigma}$ is the three-component Pauli matrices. This interaction is just an anisotropic XXZ-type exchange coupling between the ${}^1S_0$ and the ${}^3P_0$ states.

Since the full analysis of the model (2.5.2) is difficult, we here consider the simplest case, where the ${}^3P_0$ state forms a single Kondo impurity. For the Kondo impurity, the effect of the anisotropic

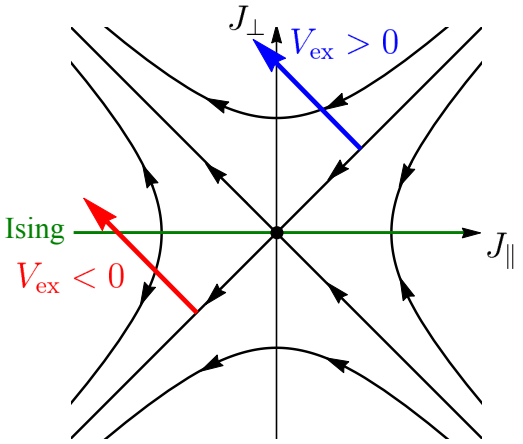

Figure 2.4: The renormalization group flow for the case of the Kondo impurity for $N = 2$. The blue (red) line shows a trajectory of the coupling constants when we apply the external laser in the case of $V_{\rm ex} > 0$ ($V_{\rm ex} < 0$).

exchange coupling can be deduced from the renormalization group (RG) flow using Anderson's poor-man's scaling for the case of Kondo impurity, particularly in the case of $N = 2$. The RG equations are Eqs. (1.2.12) and (1.2.13) as derived in Sec. 2.2 in the previous chapter. The RG flow diagram is depicted in Fig. 2.4.

When we turn on the laser in the case of $V_{\rm ex} > 0$, the coupling constants immediately change from an irrelevant coupling into a relevant one; namely, the laser-induced Kondo effect occurs, despite the bare *ferromagnetic* exchange coupling. This fact is in sharp contrast to the proposals in Ref. [150, 177, 178]. The behavior of the RG flow from the weak-coupling fixed point to the strong-coupling one may be observed as a crossover in the temperature dependence of the laser-induced Kondo effect.

In the case of $V_{\rm ex} < 0$, where the bare exchange coupling is relevant, the Kondo effect owing to $V_{\rm ex}$ (as described in Ref. [177, 178]) takes place. This Kondo effect is suppressed by the laser application. At $J = 4|V_{\rm ex}|$, the Kondo effect vanishes since the interaction is purely Ising-type: $J_\perp = 0$. After that, as seen in the flow diagram, the Kondo effect revives and the system is governed by another strong-coupling fixed point which is described in this chapter. In other words, the laser gives a novel method to induce a reenatrant Kondo effect across the Ising point.

Finally, we note that the laser-induced Kondo effect is described by a fixed point with $J_\perp \to \infty, J_z \to -\infty$, which has the opposite sign of $J_\perp$ compared to the ordinary Kondo effect. The nature of this fixed point can be extracted from a transformation

$$(S^x_{\rm imp}, S^y_{\rm imp}, S^z_{\rm imp}) \to (-S^x_{\rm imp}, -S^y_{\rm imp}, S^z_{\rm imp}), \tag{2.5.5}$$

which is equivalent to flipping the sign of $J_\perp$. Note that this transformation keeps the commutation relation intact. Since the singlet state $|\downarrow\rangle_c|\uparrow\rangle_f - |\uparrow\rangle_c|\downarrow\rangle_f$ is transformed into $|\downarrow\rangle_c|\uparrow\rangle_f + |\uparrow\rangle_c|\downarrow\rangle_f$ by this procedure, we find that the fixed point describes the Kondo effect with Kondo "singlet" $|\downarrow\rangle_c|\uparrow\rangle_f + |\uparrow\rangle_c|\downarrow\rangle_f$. In this sense, the realization of the Kondo effect in AEA provides a rare example of the "unusual" Kondo effect.

6 Summary of this chapter

In this chapter, we have proposed a possible realization of the laser-induced Kondo state using ultracold AEA in an optical lattice. It has been shown that the emergent Kondo effect under the application of the laser field overwhelms the heating effect, thereby realizing the orbital-spin entangled singlets and the heavy-fermion liquid. Furthermore, we have elucidated peculiar Kondo physics arising from the specific form of optical coupling, such as the spin-selective renormalization of effective masses and the nontrivial competition between the bare exchange coupling and the laser-induced hybridization which leads to novel crossover or reentrant behavior of the Kondo effect.

Chapter 3

Topological Phase Transition in One-Dimensional Kondo Lattice

In this chapter, by extending the setup in the previous chapter, we propose that ultracold AEA confined in one-dimensional optical lattice can realize a Kondo lattice model which hosts a fermionic SPT phase and an associated quantum phase transition in a controllable manner. The symmetry protection of the phase transition is discussed from two different viewpoints: topological properties related to spatial patterns of Kondo singlets, and symmetry eigenvalues of the spin states. We uncover the role of various symmetries in the phase diagram of this system by combining a weak-coupling approach by Abelian bosonization and strong-coupling pictures of ground states. Furthermore, in the bosonization language, we elucidate how the charge degrees of freedom of the Kondo lattice change the nature of the SPT phase from bosonic spin systems to interacting fermions.

1 1D Kondo impurity

In the cold-atom setups, the dimensionality of systems can be easily changed by tuning the hopping amplitude in the optical lattice. What happens when we consider the Kondo effect in ultracold atoms in low-dimensional systems? Hereafter, we analyze the low-energy effective model (2.5.2) for $N = 2$ in one dimension (1D). Before studying the full Kondo lattice Hamiltonian (2.5.2), it is helpful to gain some insights from what happens when a single atom in the ${}^3P_0$ state is immersed into the Fermi sea of ${}^1S_0$ atoms as an impurity. Let us consider the following Kondo impurity problems:

$$\begin{aligned} H_{1D} = &-t_c \sum_{j,\sigma} (c^\dagger_{j,\sigma} c_{j+1,\sigma} + \text{h.c.}) + U \sum_j n_{cj\uparrow} n_{cj\downarrow} \\ &- J_\perp (S^x_{c0} S^x_{\text{imp}} + S^y_{c0} S^y_{\text{imp}}) - J_z S^z_{c0} S^z_{\text{imp}}. \end{aligned} \tag{3.1.1}$$

The single impurity spin is located at $j = 0$. The impurity interacts with itinerant fermions living in 1D lattice via anisotropic Kondo couplings. Here we have introduced the interaction between itinerant fermions (the reason is described later) and consider a metallic Tomonaga-Luttinger-liquid region away from half filling.

The 1D Kondo problem was studied by Refs. [183, 184], and the situation is somewhat different from 3D. In 1D, the forward scattering off the impurity and the backward one are distinguished.

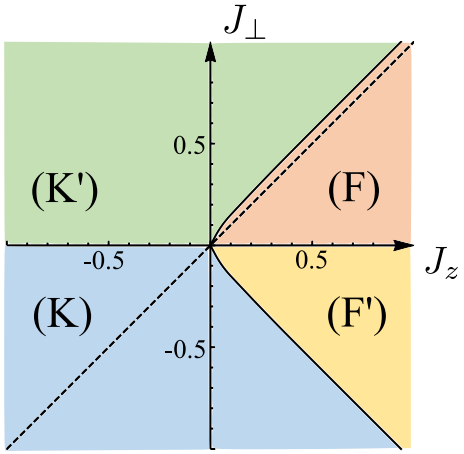

Figure 3.1: Phase diagram of the Kondo impurity in 1D. We set $J_{\perp F} = J_{\perp B} = J_\perp, J_{zF} = J_{zB} = J_z$, $v_F = 1$ and $g_2 = 0.5$. The broken line indicates the isotropic line on which $J_\perp = J_z$ is satisfied.

Hence we must double the coupling constants for the Kondo coupling: $J_{\perp F}, J_{\perp B}, J_{zF}, J_{zB}$ where the subscript F (B) denotes the forward (backward) process. Then the RG equations are given by

$$\frac{dJ_{\perp F}}{d\ell} = -\frac{1}{2\pi v_F}(J_{\perp F}J_{zF} + J_{\perp B}J_{zB}), \tag{3.1.2a}$$

$$\frac{dJ_{\perp B}}{d\ell} = -\frac{1}{2\pi v_F}(J_{\perp F}^2 + J_{\perp B}^2), \tag{3.1.2b}$$

$$\frac{dJ_{zF}}{d\ell} = \frac{1}{2\pi v_F}(g_2 J_{\perp B} - J_{\perp F}J_{zB} - J_{\perp B}J_{zF}), \tag{3.1.2c}$$

$$\frac{dJ_{zB}}{d\ell} = \frac{1}{2\pi v_F}(g_2 J_{zB} - 2J_{\perp F}J_{\perp B}), \tag{3.1.2d}$$

where $d\ell = -d\ln D$ and g_2 denotes the matrix element of the forward scattering process between itinerant fermions due to the Hubbard repulsion in Eq. (3.1.1). v_F is the Fermi velocity. By integrating Eqs. (3.1.2a) - (3.1.2d) numerically, we obtain a phase diagram in Fig. 3.1, although the flow diagram was shown only for the isotropic ($J_\perp = J_z$) case in Ref. [184]. The phase (K) shows the ordinary Kondo effect and the phase (K') shows the "unusual" Kondo effect as in the 3D case. A peculiar point in 1D is the existence of a new phase (F) where the exchange coupling grows to strong coupling starting from bare *ferromagnetic* interactions. This fixed point appears only when $g_2 > 0$ is included [184], and therefore we need to consider the Hubbard repulsion in Eq. (3.1.1). At the fixed point, the coupling constants grow as $J_{\perp F} \to -\infty, J_{\perp B} \to \infty, J_{zF} \to -\infty, J_{zB} \to \infty$. Note that the signs are negative for the forward processes and positive for the backward ones. From this observation, it turns out that the fixed point describes growth of nearest-neighbor antiferromagnetic Kondo coupling which leads to a Kondo singlet state with the adjacent sites of the impurity, while the onsite Kondo coupling is kept finite [184]. The phase (F') is not important for the later discussions, but the nature of this phase is also understood by the transformation (2.5.5).

2 Bosonization of 1D Kondo lattice

2.1 Bosonization identities

Let us now proceed to the analysis of the 1D Kondo lattice model. The properties of the 1D Kondo lattice model have been intensively studied using various analytical and numerical approaches [185, 186, 187, 188, 189, 190, 191, 192, 193, 194, 195, 196, 197, 198, 199, 200, 201, 202]. Here we adopt an analytic and a weak-coupling approach using bosonization [203]. Hereafter we consider the Hamiltonian (2.5.2) with the half-filling condition for ${}^1S_0$ states. We divide the Hamiltonian into three parts:

$$H_{\text{eff}} = H_c + H_f + H_K, \tag{3.2.1}$$

$$H_c = -t_c \sum_{j,\sigma} (c^\dagger_{j\sigma} c_{j+1\sigma} + \text{h.c.}) + U \sum_j n_{cj\uparrow} n_{cj\downarrow}, \tag{3.2.2}$$

$$H_f = J_H \sum_j \boldsymbol{S}_{fj} \cdot \boldsymbol{S}_{fj+1}, \tag{3.2.3}$$

$$H_K = -J_\perp \sum_j (S^x_{cj} S^x_{fj} + S^y_{cj} S^y_{fj}) - J_z \sum_j S^z_{cj} S^z_{fj}. \tag{3.2.4}$$

To apply the bosonization recipe, we focus on the low-energy behavior of the system and linearize the dispersion relation of the Hubbard part (3.2.2). Then Eq. (3.2.2) is bosonized using the following identity:

$$c_{j\sigma} = \frac{1}{\sqrt{2\pi}} (\eta_{R\sigma} e^{ik_F x} e^{i(\theta_{1\sigma}(x) - \phi_{1\sigma}(x))} + \eta_{L\sigma} e^{-ik_F x} e^{i(\theta_{1\sigma}(x) + \phi_{1\sigma}(x))}) \tag{3.2.5}$$

where $x = ja$ is the continuum space variable and the boson fields ϕ, θ satisfy a commutation relation $[\phi_{1\sigma}(x), \nabla\theta_{1\sigma'}(y)] = i\pi\delta_{\sigma\sigma'}\delta(x-y)$. In the above expression, the boson field ϕ are compactified as $\phi \sim \phi + 2\pi$. The Fermi momentum k_F is fixed at $k_F = \pi/2a$ due to the half-filling condition. $\eta_{R/L\sigma}$ is a Klein factor expressed in terms of Majorana fermions satisfying $\{\eta_\alpha, \eta_\beta\} = 2\delta_{\alpha\beta}$, which ensures the anticommutation relation between the right mover and the left mover. Following standard calculations, we obtain

$$H_c = \sum_{\nu=c,s} \frac{1}{2\pi} \int dx (u_{1\nu} K_{1\nu} (\nabla\theta_{1\nu})^2 + \frac{u_{1\nu}}{K_{1\nu}} (\nabla\phi_{1\nu})^2) + \frac{U}{2\pi^2\alpha} \int dx \cos(2\sqrt{2}\phi_{1c}), \tag{3.2.6}$$

where a marginally irrelevant term in the spin part is neglected. α denotes a short-range cutoff. Here the charge mode and the spin mode are defined as $\phi_{c,s} = \frac{1}{\sqrt{2}}(\phi_{1\uparrow} \pm \phi_{1\downarrow}), \theta_{c,s} = \frac{1}{\sqrt{2}}(\theta_{1\uparrow} \pm \theta_{1\downarrow})$, respectively (the minus sign stands for the spin part). The cosine term comes from the Umklapp scattering due to the Hubbard interaction. The velocities are $u_{1c} = 2t_c a\sqrt{1 + \frac{U}{2\pi t_c}}, u_{1s} = 2t_c a\sqrt{1 - \frac{U}{2\pi t_c}}$ and the Luttinger paremeters are $K_{1c} = 1/\sqrt{1 + \frac{U}{2\pi t_c}}, K_{1s} = 1$. The Luttinger parameter for the spin part has been set unity because of the spin SU(2) symmetry of the Hubbard part.

The Heisenberg part (3.2.3) is also bosonized. While one can use the standard Jordan-Wigner transformation to convert the spin chain into fermions, we here adopt an expression of the Heisenberg chain as the Mott insulating phase of the Hubbard model, where the charge mode is gapped out

by the cosine term in Eq. (3.2.6), since a parallel description is available between the ${}^1S_0$ and the ${}^3P_0$ states. Then the Heisenberg chain is described by the spin part of the bosonized Hubbard Hamiltonian as

$$H_f = \frac{1}{2\pi}\int dx(u_2(\nabla\theta_{2s})^2 + u_2(\nabla\phi_{2s})^2) \tag{3.2.7}$$

where we again set the Luttinger parameter as unity due to the SU(2) symmetry.

Finally, we bosonize the Kondo coupling (3.2.4). The spin operators of the ${}^1S_0$ state are expressed as

$$\boldsymbol{S}_c(x) \equiv \boldsymbol{S}_{cj}/\alpha = \boldsymbol{M}_c(x) + (-1)^{x/a}\boldsymbol{N}_c(x). \tag{3.2.8}$$

The uniform component $\boldsymbol{M}_c(x)$ reads

$$M_c^x(x) = \frac{1}{\pi\alpha}\sin\sqrt{2}\theta_{1s}\cos\sqrt{2}\phi_{1s}, \tag{3.2.9a}$$

$$M_c^y(x) = \frac{1}{\pi\alpha}\cos\sqrt{2}\theta_{1s}\cos\sqrt{2}\phi_{1s}, \tag{3.2.9b}$$

$$M_c^z(x) = -\frac{1}{\sqrt{2}\pi}\nabla\phi_{1s} \tag{3.2.9c}$$

and the staggered component $\boldsymbol{N}_c(x)$ is

$$N_c^x(x) = \frac{1}{\pi\alpha}\cos\sqrt{2}\theta_{1s}\sin\sqrt{2}\phi_{1c}, \tag{3.2.10a}$$

$$N_c^y(x) = -\frac{1}{\pi\alpha}\sin\sqrt{2}\theta_{1s}\sin\sqrt{2}\phi_{1c}, \tag{3.2.10b}$$

$$N_c^z(x) = \frac{1}{\pi\alpha}\cos\sqrt{2}\phi_{1s}\sin\sqrt{2}\phi_{1c}. \tag{3.2.10c}$$

Those of the ${}^3P_0$ state, $\boldsymbol{M}_f(x)$ and $\boldsymbol{N}_f(x)$, are of the same form as Eqs. (3.2.9a) - (3.2.9c) and (3.2.10a) - (3.2.10c) with the charge mode replaced by its expectation value $m = \langle\sin\sqrt{2}\phi_{2c}\rangle$. The Kondo coupling H_K is thereby divided into the following parts:

$$\begin{aligned} H_{K\perp F} =& -J_\perp\int dx(M_c^x(x)M_f^x(x) + M_c^y(x)M_f^y(x)) \\ =& H_{K\perp F+} + H_{K\perp F-}, \end{aligned} \tag{3.2.11}$$

$$\begin{aligned} H_{K\perp B} =& -J_\perp\int dx(N_c^x(x)N_f^x(x) + N_c^y(x)N_f^y(x)) \\ =& -g_{K\perp B}\int dx\sin\sqrt{2}\phi_{1c}\cos 2\theta_-, \end{aligned} \tag{3.2.12}$$

$$\begin{aligned} H_{KzF} =& -J_z\int dx M_c^z(x)M_f^z(x) \\ =& -\frac{\alpha J_z}{2\pi^2}\int dx\nabla\phi_{1s}\nabla\phi_2, \end{aligned} \tag{3.2.13}$$

$$\begin{aligned} H_{KzB} =& -J_z\int dx N_c^z(x)N_f^z(x) \\ =& H_{KzB+} + H_{KzB-} \end{aligned} \tag{3.2.14}$$

with

$$H_{K\perp F+} = -\, g_{K\perp F+} \int dx \cos 2\phi_+ \cos 2\theta_-, \tag{3.2.15}$$

$$H_{K\perp F-} = -\, g_{K\perp F-} \int dx \cos 2\phi_- \cos 2\theta_-, \tag{3.2.16}$$

$$H_{KzB+} = -\, g_{KzB+} \int dx \sin \sqrt{2}\phi_{1c} \cos 2\phi_+, \tag{3.2.17}$$

$$H_{KzB-} = -\, g_{KzB-} \int dx \sin \sqrt{2}\phi_{1c} \cos 2\phi_-, \tag{3.2.18}$$

where the coupling constants are

$$g_{K\perp F+} = g_{K\perp F-} = \frac{1}{2m} g_{K\perp B} = \frac{J_\perp}{2\pi^2 \alpha}, \tag{3.2.19}$$

$$g_{KzB+} = g_{KzB-} = \frac{m J_z}{2\pi^2 \alpha}. \tag{3.2.20}$$

Here we have named each perturbation with subscript F and B in terms of momentum transfers of itinerant fermions in analogy with the impurity problem. In the calculation, we have dropped the oscillation terms which vanish after the integration. Also we have defined new boson fields $\phi_\pm, \theta_\pm$ as

$$\phi_\pm \equiv \frac{1}{\sqrt{2}}(\phi_{1s} \pm \phi_{2s}), \tag{3.2.21}$$

$$\theta_\pm \equiv \frac{1}{\sqrt{2}}(\theta_{1s} \pm \theta_{2s}), \tag{3.2.22}$$

which describe the total (+) and relative (−) spin modes, respectively.

2.2 RG equations

The low-energy behavior of the model (3.2.1) is deduced from RG equations. Here we treat the free boson part in Eqs. (3.2.6) and (3.2.7) as unperturbed theory. The Umklapp part in Eq. (3.2.6) and the Kondo coupling are added as perturbation. However, since H_{KzF} can be incorporated into the free-boson parts, we include H_{KzF} into the unperturbed theory. The resulting unperturbed theory is

$$\begin{aligned} H_0 =& \frac{1}{2\pi} \int dx (u_{1c} K_{1c} (\nabla\theta_{1c})^2 + \frac{u_{1c}}{K_{1c}} (\nabla\phi_{1c})^2) \\ &+ \sum_{\nu=\pm} \frac{1}{2\pi} \int dx (u_\nu K_\nu (\nabla\theta_\nu)^2 + \frac{u_\nu}{K_\nu} (\nabla\phi_\nu)^2). \end{aligned} \tag{3.2.23}$$

Here $u_\pm = u\sqrt{1 \mp \frac{\alpha J_z}{2\pi u}}$ and the naive estimation of the Luttinger parameters leads to

$$K_\pm = \frac{1}{\sqrt{1 \mp \frac{\alpha J_z}{2\pi u}}}, \tag{3.2.24}$$

where $u_{1s} = u_2 = u$ is assumed, for simplicity. The perturbation terms are $H_{K\perp F\pm}, H_{K\perp B}, H_{KzB\pm}$, and

$$H_U = g_U \int dx \cos(2\sqrt{2}\phi_{1c}) \tag{3.2.25}$$

with $g_U = \frac{U}{2\pi^2\alpha}$. Since the unperturbed theory is free bosons and thus is a conformal field theory (CFT), the RG equations can be derived from the CFT data of the free boson theory, i.e. scaling dimensions and operator-product-expansion coefficients [204]. After some calculations, we arrive at a set of RG equations when the cutoff is changed from α to $e^{d\ell}\alpha$, as

$$\frac{dK_{1c}}{d\ell} = -K_{1c}^2(2\tilde{g}_U + 2\tilde{g}_{K\perp B}^2 + \tilde{g}_{KzB+}^2 + \tilde{g}_{KzB-}^2), \tag{3.2.26a}$$

$$\frac{dK_+}{d\ell} = -K_+^2(2\tilde{g}_{K\perp F+}^2 + 2\tilde{g}_{KzB+}^2), \tag{3.2.26b}$$

$$\frac{dK_-}{d\ell} = -K_-^2(2\tilde{g}_{K\perp F-}^2 + 2\tilde{g}_{KzB-}^2) + 2\tilde{g}_{K\perp F+}^2 + 2\tilde{g}_{K\perp F-}^2 + 4\tilde{g}_{K\perp B}^2, \tag{3.2.26c}$$

and

$$\frac{d\tilde{g}_U}{d\ell} = (2 - 2K_{1c})\tilde{g}_U + \tilde{g}_{K\perp B}^2 + \tilde{g}_{KzB+}^2 + \tilde{g}_{KzB-}^2, \tag{3.2.26d}$$

$$\frac{d\tilde{g}_{K\perp 1+}}{d\ell} = (2 - K_+ - \frac{1}{K_-})\tilde{g}_{K\perp F+} - \tilde{g}_{K\perp B}\tilde{g}_{KzB+}, \tag{3.2.26e}$$

$$\frac{d\tilde{g}_{K\perp 1-}}{d\ell} = (2 - K_- - \frac{1}{K_-})\tilde{g}_{K\perp F-} - \tilde{g}_{K\perp B}\tilde{g}_{KzB-}, \tag{3.2.26f}$$

$$\frac{d\tilde{g}_{K\perp 2}}{d\ell} = (2 - \frac{1}{2}K_{1c} - \frac{1}{K_-})\tilde{g}_{K\perp B} - \tilde{g}_{K\perp F+}\tilde{g}_{KzB+} - \tilde{g}_{K\perp F-}\tilde{g}_{KzB-} + \frac{1}{2}\tilde{g}_U\tilde{g}_{K\perp B}, \tag{3.2.26g}$$

$$\frac{d\tilde{g}_{KzB+}}{d\ell} = (2 - \frac{1}{2}K_{1c} - K_+)\tilde{g}_{KzB+} - \tilde{g}_{K\perp F+}\tilde{g}_{K\perp B} + \frac{1}{2}\tilde{g}_U\tilde{g}_{KzB+}, \tag{3.2.26h}$$

$$\frac{d\tilde{g}_{KzB-}}{d\ell} = (2 - \frac{1}{2}K_{1c} - K_-)\tilde{g}_{KzB-} - \tilde{g}_{K\perp F-}\tilde{g}_{K\perp B} + \frac{1}{2}\tilde{g}_U\tilde{g}_{KzB-}, \tag{3.2.26i}$$

up to the second order perturbation theory. Here the dimensionless coupling constants are defined by $\tilde{g}_\alpha \equiv \frac{1}{\pi}g_\alpha a^{2-\Delta_\alpha}$, where Δ_α is the scaling dimension of the perturbation.

3 Phase diagram

The zero-temperature phase diagram of the system is determined by fixed points derived from the RG equations (3.2.26a) - (3.2.26i). Numerical solutions of the RG equations indicate the phase diagram summarized in Fig. 4.2. In calculating Fig. 4.2, we have set $\tilde{g}_U = 0.1$ and the initial values of the coupling constants as $\tilde{g}_{K\perp F\pm} = \frac{1}{2}\tilde{g}_{K\perp B} = \tilde{g}_{K\perp}$ and $\tilde{g}_{KzB\pm} = \tilde{g}_{Kz}$. The phase diagram is fully symmetric with respect to the sign of $\tilde{g}_{K\perp}$. As seen from scaling dimensions, the low-energy behavior is mainly governed by relevant terms $H_{K\perp B}, H_{KzB+}$, and H_{KzB-}. Each phase is characterized by the most divergent interactions as follows:

(K)	$\tilde{g}_{K\perp B} \to -\infty,$	$\tilde{g}_{KzB+} \to -\infty$
(K')	$\tilde{g}_{K\perp B} \to +\infty,$	$\tilde{g}_{KzB+} \to -\infty$
(Top)	$\tilde{g}_{K\perp B} \to +\infty,$	$\tilde{g}_{KzB+} \to +\infty$
(Top')	$\tilde{g}_{K\perp B} \to -\infty,$	$\tilde{g}_{KzB+} \to +\infty$
(N1)	$\tilde{g}_{KzB+} \to -\infty,$	$\tilde{g}_{KzB-} \to -\infty$
(N2)	$\tilde{g}_{KzB+} \to +\infty,$	$\tilde{g}_{KzB-} \to +\infty$

The phase boundary between (K') and (Top) (or (K) and (Top')) is signaled by the change of the sign of $\tilde{g}_{KzB+}$. On the other hand, the transitions to the phase (N1) or (N2) are determined by competition between $H_{K\perp B}$ and H_{KzB-}, which cannot be minimized simultaneously. Since the renormalization is stopped around $\tilde{g}(\ell) \sim 1$, we determine those phase boundaries by examining which of $\tilde{g}_{K\perp B}$ and $\tilde{g}_{KzB-}$ first grows to unity. We note that the role of less relevant $H_U, H_{K\perp F\pm}$ terms is the shift of phase boundaries. If we truncate the RG equations up to the tree level, the phase boundary between the phase (K') and the phase (Top) is located at $\tilde{g}_{Kz} = 0$. Thus the generation of effective couplings due to less relevant interactions significantly shifts the phase boundaries.

Qualitatively, our weak-coupling calculation by the perturbative RG approach reproduces the phase diagram of 1D anisotropic Kondo lattice obtained by strong coupling expansion and exact diagonalization of a small cluster [197]. We note that the precise positions of phase boundaries depend on the Luttinger parameter. As clearly seen, the phase diagram has some resemblance with the impurity phase diagram in Fig. 3.1 except for the appearance of the phases (N1) and (N2), which denote Néel orders absent in the impurity problem. In the following subsections, we explain the details of each phase.

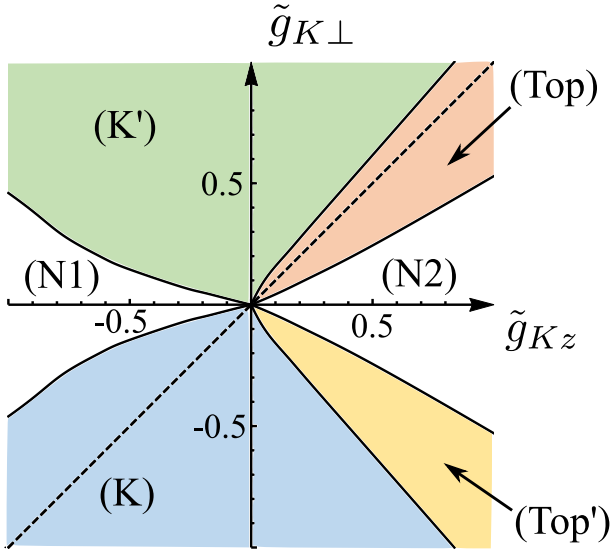

Figure 3.2: Phase diagram of the 1D anisotropic Kondo lattice model. The broken line indicates the isotropic line on which $J_\perp = J_z$ is satisfied.

3.1 Kondo insulator

The phases (K), (K'), (Top), and (Top') are described by pinning of ϕ_{1c}, ϕ_+ and θ_- to their potential minimum, leading to disordered ground states with an energy gap. The phase (K) corresponds to

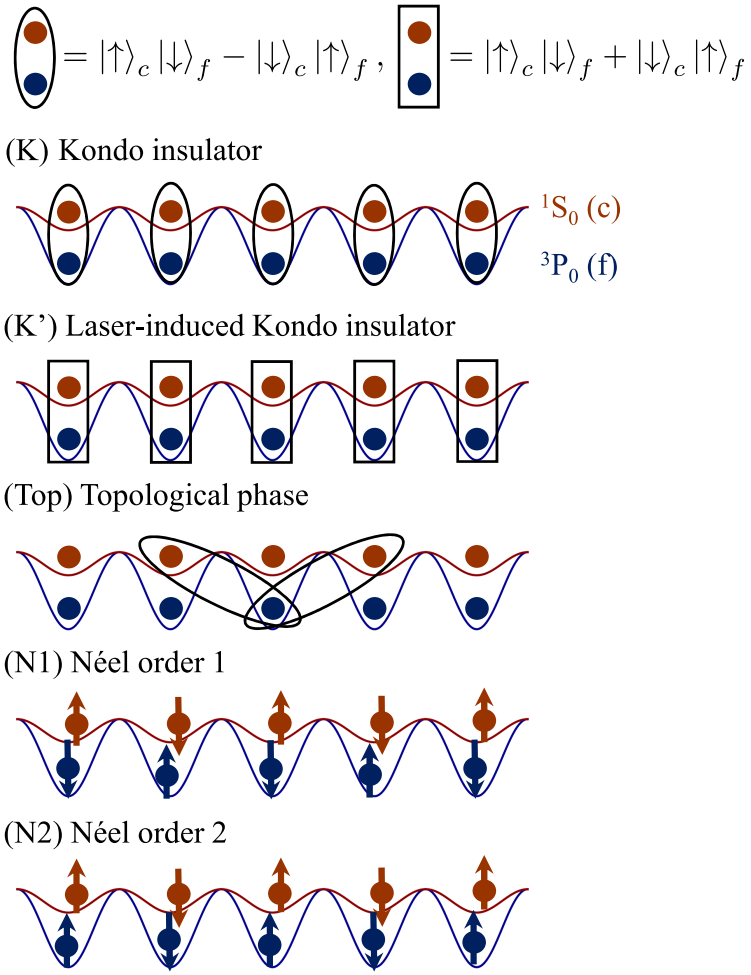

Figure 3.3: Schematic pictures of the phases of the 1D Kondo lattice. The red (blue) balls illustrate atoms in the ${}^1S_0$ (${}^3P_0$) state loaded in a shallow (deep) optical lattice potential. In the figure of the phase (Top), the singlet formation is represented by the central site for clarity of illustration.

the growth of on-site antiferrromagnetic Kondo coupling, which means the formation of the Kondo insulator [185]. The strong coupling picture of this phase is illustrated in Fig. 3.3, where the Kondo singlet at each site opens the energy gaps in charge and spin sectors. We note that the Kondo coupling effectively generates the Hubbard repulsion between conductive fermions due to Eq. (3.2.26d). Hence, even if the bare Hubbard interaction is switched off, the Kondo insulator cannot be distinguished from the Mott insulating state at least in the low-energy region. At the strong coupling limit, the Kondo insulating state approaches to the rung-singlet state if we regard the system as a spin-1/2 ladder.

3.2 Laser-induced Kondo insulator

With sufficiently strong laser coupling, the phase (K') is realized owing to Eqs. (2.5.4a) and (2.5.4b). This phase is also a Kondo insulator, but is composed of the "unusual" Kondo effect described in Sec. 1 by a strong coupling fixed point with anisotropic Kondo coupling. The physical picture of this Kondo insulator is obtained by a unitary transformation

$$f_{j\sigma} \to \mathrm{sgn}(\sigma) f_{j\sigma}, \tag{3.3.1}$$

which flips the sign of S^x_{fj}, S^y_{fj} and maps the Kondo singlet $|{\downarrow}\rangle_c |{\uparrow}\rangle_f - |{\uparrow}\rangle_c |{\downarrow}\rangle_f$ to $|{\downarrow}\rangle_c |{\uparrow}\rangle_f + |{\uparrow}\rangle_c |{\downarrow}\rangle_f$. Thus, in the strong coupling limit, the phase (K') is described by an insulating state where the ${}^1S_0$ state and the ${}^3P_0$ state form the "Kondo singlet" $|{\downarrow}\rangle_c |{\uparrow}\rangle_f + |{\uparrow}\rangle_c |{\downarrow}\rangle_f$ at each site (Fig. 3.3). The unusual Kondo singlet has total spin 1 with $S^z_c + S^z_f = 0$, and therefore the expectation value of total spin is nonzero in the x, y plane: $\langle (S^x_{cj} + S^x_{fj})^2 + (S^y_{cj} + S^y_{fj})^2 \rangle \neq 0$. In the language of spin systems, this phase is very similar to the so-called large-D phase [197] where a strong single-ion anisotropy favors the $S^z = 0$ state in spin-1 systems [67].

3.3 Topological phase

The phase (Top) in Fig. 4.2 is a nontrivial topological phase protected by the spatial inversion symmetry, whose topological aspects are described in the next section. This phase includes the case of isotropic ferromagnetic Kondo coupling indicated by the broken line in Fig. 4.2. This phase is smoothly connected to the Haldane phase in spin ladders [205, 206, 207, 208] in the strong coupling limit $U \to \infty$ (or $J_\perp, J_z \to \infty$) [195]. An intuitive picture of this fixed point can be obtained by considering a nearest-neighbor Kondo coupling

$$\tilde{H}_K \equiv -\tilde{J} \sum_j (\boldsymbol{S}_{c,j-1} + \boldsymbol{S}_{c,j+1}) \cdot \boldsymbol{S}_{f,j} \tag{3.3.2}$$

in addition to the original on-site Kondo coupling. The bosonized Hamiltonian is changed as

$$H_{K\perp F} \to \frac{J_\perp + \tilde{J}}{J_\perp} H_{K\perp F}, \tag{3.3.3a}$$

$$H_{K\perp B} \to \frac{J_\perp - \tilde{J}}{J_\perp} H_{K\perp B}, \tag{3.3.3b}$$

$$H_{KzF} \to \frac{J_z + \tilde{J}}{J_z} H_{KzF}, \tag{3.3.3c}$$

$$H_{KzB} \to \frac{J_z - \tilde{J}}{J_z} H_{KzB}. \tag{3.3.3d}$$

Thus, the fixed point is equivalent to growth of the *nearest-neighbor antiferromagnetic* Kondo coupling, similarly to the phase (F) appearing in the 1D Kondo impurity problem in Sec. 1, while the on-site Kondo coupling is ferromagnetic and kept finite. An intuitive picture is illustrated in Fig. 3.3. The formation of the non-local Kondo singlets is reminiscent of 1D topological Kondo insulators [209, 210, 211, 212] realized by a p-wave Kondo coupling. In fact, the low-energy effective theory is the same as that of the 1D topological Kondo insulators [210].

We note that the nature of the phase (Top') is related to the topological phase (Top) via the transformation (3.3.1), although this phase cannot be realized because the coupling constants cannot be manipulated into the corresponding parameter region, since J is always positive in Eqs. (2.5.4a) and (2.5.4b).

3.4 Néel order

The phases (N1) and (N2) which appear near the "Ising line" $J_\perp = 0$ have an antiferromagnetic Néel order with spontaneously broken spin flip symmetry. The ordered spin patterns are illustrated in Fig. 3.3. To understand the appearance of the Néel order, it is useful to consider the case of $J_\perp = 0$. In this case, the remaining perturbation terms are H_U, H_{KzB+}, and H_{KzB-}, which are all relevant for $U > 0$ and thus lock the fields $\phi_{1c}, \phi_+, \phi_-$ at their potential minimum. The locking of $\phi_\pm$ leads to the nonzero expectation value of $N^z_{c,f}(x)$ (Eq. (3.2.10c)), implying the emergence of the Néel ordering. Since the pinning of $\phi_{1c}, \phi_+, \phi_-$ opens the energy gap and the gap cannot be collapsed by infinitesimal perturbation, the Néel order should persist to some threshold value of $J_\perp$. However, the threshold value should not exceed $|J_z|$, since at the isotropic line $|J_\perp| = |J_z|$ we obtain the Kondo insulating phases or the topological phases by non-Abelian bosonization [187, 188].

The existence of the Néel order can also be naturally understood from the corresponding impurity problem described in Sec. 1. When the Kondo coupling is completely Ising-like with vanishing $J_\perp$, we do not have the Kondo effect and the impurity ground state is doubly degenerate where the spins of conduction electrons and the impurity align ferromagnetically in $J_z > 0$ and antiferromagnetically in $J_z < 0$. Thus the residual impurity entropy $\ln 2$ should be washed out by spin ordering in the case of Kondo lattice systems.

4 Symmetry protection

All the quantum phases of the 1D anisotropic Kondo lattice described in Sec. 3 have energy gaps both in charge and spin excitations. While the Néel orders can be characterized by spontaneous breaking of the spin flip symmetry, rest four phases have the same symmetries and cannot be characterized by spontaneous symmetry breaking. Then, what characterizes these phases? Is there any order parameter or topological property to distinguish these phases? In this section, we describe the roles of various symmetries in the system and provide conditions to distinguish these four phases as different quantum phases.

4.1 SPT phase in one dimension: a bosonization viewpoint

The structure of symmetry protection of SPT phases should be encoded in their low-energy effective theory. Description of symmetry protection in bosonization language was discussed in Refs. [213, 214]. To analyze the topological properties in the present system, we here adopt this approach combining the MPS description in Sec. 3.3 of Chap. 1. Since the bosonization description with

perturbative RG is only applicable to low-energy states of the unperturbed theory, the description of symmetry protection using bosonization is not exact in contrast to the MPS approach. However, the advantage here is that we can discuss the symmetry protection at a Hamiltonian level, not using explicit expression of ground states. To exemplify the symmetry protection using bosonization approach, let us consider the following sine-Gordon theory:

$$H = \frac{1}{2\pi}\int dx (uK(\nabla\theta)^2 + \frac{u}{K}(\nabla\phi)^2 + g\cos\frac{\phi}{R}). \tag{3.4.1}$$

We here assume that the boson field ϕ is compactified with radius R (namely $\phi \sim \phi + 2\pi R$), and hence the cosine term appearing in the Hamiltonian is the most relevant perturbation allowed in the system. For simplicity, we do not consider a vertex operator which contains the dual field θ, or simply assume that such term is forbidden by a symmetry. The ground state of this theory is gapped if $K < 8R^2$, and the boson field ϕ is pinned at $\phi = 0$ for $g < 0$ and $\phi = \pi R$ for $g > 0$. The two phases are separated by a critical point at $g = 0$. If the sine term $\sin\frac{\phi}{R}$ is forbidden by a symmetry constraint, we can say that the two phases cannot be adiabatically connected, since the cosine term is the most relevant perturbation in the system. Conversely, we can connect the two phases if the sine term is allowed, since $g\cos\frac{\phi}{R} + g'\sin\frac{\phi}{R} = G\cos(\frac{\phi}{R} + \gamma)$ and the parameter γ can be changed from 0 to π by tuning the ratio between g and g'.

4.2 Protection by spin π rotation symmetries around the x or y axis

Let us analyze the symmetry protection of quantum phases of the 1D Kondo lattice. First we calculate the phase factors in Sec. 3.3 of Chap. 1 for each symmetry of the system. Among them, we focus on the spin π rotation symmetry around x or y axis. To calculate the phase factors, we use a strong coupling limit $|J_\perp|, |J_z| \to \infty$, since the phase factors cannot change unless the energy gap collapses. The strong coupling limit of the topological phase is continuously connected to the Haldane phase of the spin-1 Heisenberg model, and therefore we obtain $\vartheta_x = \vartheta_y = 0$. In the strong coupling limit of the (ordinary) Kondo insulator and the laser-induced Kondo insulator, the ground states are site-product states of on-site Kondo singlets. The Kondo singlet is $|\downarrow\rangle_c|\uparrow\rangle_f - |\uparrow\rangle_c|\downarrow\rangle_f$ for the former phase, and $|\downarrow\rangle_c|\uparrow\rangle_f + |\uparrow\rangle_c|\downarrow\rangle_f$ for the latter phase, respectively. Since

$$R_x(|\downarrow\rangle_c|\uparrow\rangle_f - |\uparrow\rangle_c|\downarrow\rangle_f) = +(|\downarrow\rangle_c|\uparrow\rangle_f - |\uparrow\rangle_c|\downarrow\rangle_f), \tag{3.4.2}$$

$$R_x(|\downarrow\rangle_c|\uparrow\rangle_f + |\uparrow\rangle_c|\downarrow\rangle_f) = -(|\downarrow\rangle_c|\uparrow\rangle_f + |\uparrow\rangle_c|\downarrow\rangle_f), \tag{3.4.3}$$

and the same holds for R_y, we obtain $\vartheta_x = \vartheta_y = 0$ for the ordinary Kondo insulator and $\vartheta_x = \vartheta_y = \pi$ for the laser-induced Kondo insulator. By comparing ϑ_x, ϑ_y of each phase, we conclude that the laser-induced Kondo insulating phase is distinct from the ordinary Kondo insulator and the topological phase, protected by the spin π rotation symmetry around x or y axis. To connect the distinct phases, we must close the energy gap or break the symmetry. In fact, at the phase boundary between the topological phase and the laser-induced Kondo insulator, the spin gap of ϕ_+ is collapsed. At the boundary between the ordinary and the anomalous Kondo insulators, the Néel order intervenes, signaling the symmetry breaking. Thus, the phase diagram obtained in Sec. 3 is consistent with the symmetry protection. As noted in Sec. 3.3 of Chap. 1, this symmetry protection is not related to the topological property of the SPT phases.

If the spin π rotation symmetries are broken, we can adiabatically connect the laser-induced Kondo insulator and the ordinary Kondo insulator. To check this, let us consider a unitary trans-

formation [215] $U(\gamma)^\dagger H U(\gamma)$ with

$$U(\gamma) = \exp\Big[i\gamma \sum_j S^z_{fj}\Big], \tag{3.4.4}$$

which changes the Kondo coupling into

$$\begin{aligned} & U(\gamma)^\dagger H_K U(\gamma) \\ =& - J_\perp \cos\gamma \sum_j (S^x_{cj} S^x_{fj} + S^y_{cj} S^y_{fj}) - J_z \sum_j S^z_{cj} S^z_{fj} \\ & - J_\perp \sin\gamma \sum_j (S^x_{cj} S^y_{fj} - S^y_{cj} S^x_{fj}). \end{aligned} \tag{3.4.5}$$

The rest H_c and H_f are unchanged. As seen easily, the spin π rotation symmetry around x or y axis is broken in the transformed Hamiltonian except for $\gamma = 0, \pi$. Since $U(\gamma)$ is unitary, the energy spectra of H and $U(\gamma)^\dagger H U(\gamma)$ are identical. Thus we can connect the ordinary Kondo insulator at $\gamma = 0$ and the laser-induced Kondo insulator at $\gamma = \pi$ without closing the energy gap by changing γ continuously.

We can also show the symmetry protection using the bosonization language. To apply the symmetry protection argument to the present Kondo lattice system, we fisrt summarize the symmetry transformation of bosonized fields for each symmetry of the system. The translational operation $c_\sigma(x) \to c_\sigma(x+a)$, $\boldsymbol{S}_f(x) \to \boldsymbol{S}_f(x+a)$ can be expressed in terms of the boson fields as

$$\phi_{1c}(x) \to \phi_{1c}(x+a) - \sqrt{2} k_F a, \tag{3.4.6a}$$
$$\theta_{1c}(x) \to \theta_{1c}(x+a), \tag{3.4.6b}$$
$$\phi_{1s}(x) \to \phi_{1s}(x+a), \tag{3.4.6c}$$
$$\theta_{1s}(x) \to \theta_{1s}(x+a). \tag{3.4.6d}$$

The transformation on ϕ_{2s} and θ_{2s} is same as that on ϕ_{1s} and θ_{1s}. Similarly, we obtain the following results. For the charge U(1) symmetry $c_\sigma \to e^{i\varphi} c_\sigma$,

$$\phi_{1c} \to \phi_{1c}, \tag{3.4.7a}$$
$$\theta_{1c} \to \theta_{1c} + \varphi, \tag{3.4.7b}$$
$$\phi_{1s} \to \phi_{1s}, \tag{3.4.7c}$$
$$\theta_{1s} \to \theta_{1s}. \tag{3.4.7d}$$

For the spatial inversion operation $c_\sigma(x) \to c_\sigma(a-x)$, $\boldsymbol{S}_f(x) \to \boldsymbol{S}_f(a-x)$,

$$\phi_{1c}(x) \to -\phi_{1c}(a-x) + \sqrt{2} k_F a, \tag{3.4.8a}$$
$$\theta_{1c}(x) \to \theta_{1c}(a-x), \tag{3.4.8b}$$
$$\phi_{1s}(x) \to -\phi_{1s}(a-x), \tag{3.4.8c}$$
$$\theta_{1s}(x) \to \theta_{1s}(a-x). \tag{3.4.8d}$$

For the spin π rotation around x axis $S^x_{c,f} \to S^x_{c,f}, S^{y,z}_{c,f} \to -S^{y,z}_{c,f}$,

$$\phi_{1c} \to \phi_{1c}, \tag{3.4.9a}$$
$$\theta_{1c} \to \theta_{1c}, \tag{3.4.9b}$$
$$\phi_{1s} \to -\phi_{1s}, \tag{3.4.9c}$$
$$\theta_{1s} \to -\theta_{1s}, \tag{3.4.9d}$$

and for that around y axis $S^y_{c,f} \to S^y_{c,f}, S^{x,z}_{c,f} \to -S^{x,z}_{c,f}$,

$$\phi_{1c} \to \phi_{1c}, \tag{3.4.10a}$$
$$\theta_{1c} \to \theta_{1c}, \tag{3.4.10b}$$
$$\phi_{1s} \to -\phi_{1s}, \tag{3.4.10c}$$
$$\theta_{1s} \to -\theta_{1s} + \frac{\pi}{\sqrt{2}}. \tag{3.4.10d}$$

Finally, for the spin U(1) symmetry $S^x_{c,f} \to S^x_{c,f}\cos\varphi + S^y_{c,f}\sin\varphi$ and $S^y_{c,f} \to -S^x_{c,f}\sin\varphi + S^y_{c,f}\cos\varphi$, we obtain

$$\phi_{1s} \to \phi_{1s}, \tag{3.4.11a}$$
$$\theta_{1s} \to \theta_{1s} + \varphi, \tag{3.4.11b}$$
$$\phi_{1c} \to \phi_{1c}, \tag{3.4.11c}$$
$$\theta_{1c} \to \theta_{1c}. \tag{3.4.11d}$$

Let us focus on a parameter region near the phase boundary between the topological phase and the laser-induced Kondo insulator. In that region, the relevant perturbation for the gap generation in terms of the scaling dimensions is $H_{K\perp B}$ and H_{KzB+}, and the low-energy behavior is governed by these terms, making the fields ϕ_{1c}, ϕ_+, and θ_- locked at their potential minimum. Here we note that the $H_{K\perp B}$ term does not change its sign between the two phases, but the H_{KzB+} term does. Hence the difference between the two phases is the pinning position of the total spin mode ϕ_+. To adiabatically connect the two phases preserving the energy gap, we must shift the expectation value of ϕ_+ by allowing a perturbation term like

$$g'_{KzB+} \int dx \sin\sqrt{2}\phi_{1c} \sin 2\phi_+. \tag{3.4.12}$$

We note that in the present system an additional spin U(1) symmetry forbids perturbations containing the dual field θ_+. However, the shift of the expectation value of ϕ_+ necessarily breaks the spin π rotation symmetry. Hence the quantum phase transition between the topological phase and the laser-induced Kondo insulator is protected by the spin π rotation symmetry, being consistent with the analysis of symmetry eigenvalues. We note that the perturbation (3.4.12) also breaks the inversion symmetry. This fact is important for the topological properties discussed in the next subsection.

To connect the ordinary Kondo insulator and the laser-induced Kondo insulator, we must shift the expectation value of θ_-. This procedure also breaks the spin π rotation symmetries. The required perturbation can be obtained by bosonization of the last term in Eq. (3.4.5).

4.3 Protection by spatial inversion symmetry: role of the charge degrees of freedom

Now we describe the symmetry protection of the topological phase. The topological phase approaches the Haldane phase in spin chains in the strong coupling limit $U \to \infty$. Hence the topological phase of the 1D Kondo lattice is expected to be stable under either time-reversal, spatial inversion, or spin dihedral symmetry, if U is sufficiently large and the charge degrees of freedom are frozen in the low-energy part of the Hilbert space. However, if $J_\perp, J_z$ and U are small compared to

the kinetic energy t_c, we can no more regard the system as bosonic (spin) systems and must treat it as interacting fermions. It was previously shown [216, 217] that the Haldane phase with mobile charge degrees freedom is unstable and can be adiabatically connected to a trivial band insulator by only breaking inversion symmetry, even if the time-reversal and spin rotation symmetries are preserved. This fact stems from that the charge fluctuations in the low-energy Hilbert space mixes the integer-spin representation of the original spin chain and that of half-odd-integer spin, invalidating the proof of the symmetry protection in Sec. 3.3 in Chap. 1. Hence the only protecting symmetry of the topological phase is the inversion symmetry. Under the inversion symmetry, the degeneracy of the entanglement spectrum, which is a fingerprint of the SPT phase, still persists [217]. A similar degenerate structure of the entanglement spectrum is also observed in 1D topological Kondo insulator [212] and 1D periodic Anderson model with Hund coupling [218], indicating the existence of the SPT phase. A related study on a three-leg Hubbard ladder has been also performed [219].

We can check the above properties for the present Kondo lattice system by the bosonization method. Let us first consider the strong coupling limit $U \to \infty$. In this case, the charge mode ϕ_{1c} is completely frozen to the potential minimum of the Umklapp term (3.2.25). The remaining degrees of freedom are the total and relative spin modes $\phi_\pm, \theta_\pm$, and they are equivalent to the effective theory of the corresponding spin ladder system [207, 208]. Hence the proof of symmetry protection can be performed in parallel with the case of the spin ladder [214]. To connect the topological phase with the trivial phases, a shift of the expectation value of ϕ_+ must take place, which breaks the time-reversal, spatial inversion, and spin dihedral symmetries. Hence the topological phase is protected by those three symmetries. However, the situation is changed if we consider a weakly interacting regime. If the Hubbard interaction U is sufficiently small, the Umklapp term is less relevant than the Kondo couplings $H_{K\perp B}, H_{KzB+}$, and H_{KzB-}. Thus the low-energy behavior is mainly governed by the Kondo couplings. In this case, we can adiabatically connect the topological phase and the ordinary Kondo insulator without closing the energy gap, by shifting the expectation value of the charge mode. This is done by adding the following perturbation:

$$g'_{K\perp B}\int dx \cos\sqrt{2}\phi_{1c}\cos 2\theta_- + g'_{KzB+}\int dx \cos\sqrt{2}\phi_{1c}\cos 2\phi_+ \tag{3.4.13}$$

which is generated by an artificial Kondo coupling

$$H'_K = J'\sum_{j,\sigma,\sigma'} c^\dagger_{j\sigma}\boldsymbol{\sigma}_{\sigma\sigma'}c_{j+1\sigma'}\cdot\boldsymbol{S}_{fj} + \text{h.c.}. \tag{3.4.14}$$

This perturbation only breaks the inversion symmetry, and preserves the other symmetries. In the present system, the charge U(1) symmetry prohibits vertex operators which involve the field θ_{1c}. Thus, the only possible way to connect the topological phase and the trivial phase using the charge degrees of freedom is the shift of the expectation value of ϕ_{1c} accompanied by the breaking of inversion symmetry. From these observations, we conclude that the topological phase is protected only by the inversion symmetry.

From the above argument, we can interpret the crossover from the fermionic SPT phase (protected by the inversion symmetry only) to the bosonic SPT phase (protected by the time-reversal, inversion, and spin dihedral symmetries) via the bosonization language. In the weakly interacting regime, the low-energy behavior of the charge mode is mainly determined by the Kondo coupling rather than the Umklapp scattering due to the Hubbard repulsion. In this case, we can connect the topological phase and the trivial phase by shifting the pinning position of the charge mode with

breaking the inversion symmetry, while the time-reversal and the spin rotation symmetries are kept intact. However, this shift cannot be reconciled with minimization of the Umklapp term H_U. Hence if we gradually increase the Hubbard repulsion U, the above procedure fails to work at some point. After that, the topological phase and the trivial phase are separated by a quantum phase transition if the time-reversal or the spin dihedral symmetry is present. We note that the perturbation (3.4.13) vanishes if the charge mode is frozen at the potential minimum of the Umklapp term, $2\sqrt{2}\phi_{1c} = \pi$.

Before closing this section, we clarify where the topological phase of the Kondo lattice stands in the classification of SPT phases of interacting fermions. In non-interacting systems, topological insulators protected by the inversion symmetry in 1D are classified [102, 103, 220] by integer $\mathbb{Z}$, which means that there are infinitely many different topological phases. However, when we allow interactions as perturbation to systems, a part of nontrivial topological phases can be connected to the trivial phase and free-fermion classification of topological phases is reduced to its subgroup [105, 75, 221, 111, 112], as we have discussed in Sec. 3.5 of Chap. 1. In the case of inversion-symmetric topological insulators, the classification is performed by several methods [222, 223, 224] and is argued to reduce from $\mathbb{Z}$ to $\mathbb{Z}_4$ in the interacting case. Since the Haldane phase is classified by $\mathbb{Z}_2$, two copies of them can be deformed into the trivial phase. Using the fact that the topological phase of the 1D Kondo lattice approaches the Haldane phase in the strong coupling limit, we can also deform the two copies of the model (3.2.1) into a trivial phase. Thus we conclude that the topological phase in 1D Kondo lattice is specified by an integer $2 \in \mathbb{Z}_4 = \{0, 1, 2, 3\}$.

5 Fate of edge states and experimental detection

We have demonstrated the topological phase of the 1D Kondo lattice is protected only by the inversion symmetry when the charge fluctuations cannot be ignored, while the Haldane phase in the strong coupling limit is also protected by the time-reversal and spin dihedral symmetries. The change of the nature of the topological phase from fermionic to bosonic SPT phases leads to an intriguing consequence in the fate of edge states of the topological phase. In the strong coupling regime, the Haldane phase has spin-1/2 zero-energy states at the edge of the system. The edge states are magnetically active, and have been detected by applying magnetic fields [225, 226]. On the other hand, in the weak-coupling regime, the SPT phase is protected only by the inversion symmetry. This means that the zero-energy edge state is absent in general, since the edges generically break the inversion symmetry. Thus it is implied that the edge states gradually decrease their excitation energies with increasing the Hubbard interaction U, and finally they turn into the zero-energy state at some threshold value of U. Such "interaction-induced" edge states are one possible hallmark of the crossover from fermionic SPT phases to bosonic ones.

Observation of such a crossover using the present cold-atom setup is intriguing but may be a challenging issue. To detect a clear signature of the edge states, it is appropriate to create an interface between the topologically nontrivial phase and the trivial phase [138, 227], since the true edge of the atomic cloud is usually a metallic state due to a harmonic confinement potential. In our setup, the interface can be easily created, since the topological-trivial phase transition is caused by the laser irradiation, which can be performed in a spatially varying manner. The interface-localized edge modes are, in principle, detected by combining a magnetic field and spin-resolved quantum gas microscopy, by which antiferromagnetic correlations have been recently observed in the Fermi-Hubbard model [228, 229, 230].

6 Summary of this chapter

In this chapter, we have shown that cold-atom realization of the Kondo lattice model offers a platform to investigate a 1D SPT phase and an associated quantum phase transition with high contrabillity. By utilizing the spin-exchanging collisions with the help of the laser-induced mixing of internal states, ultracold AEA in optical lattice can realize the Kondo lattice with tunable anisotropic Kondo couplings, which is hard to be realized in solid state experiments. Since the sign of the bare exchange coupling V_{ex} can be controlled using the confinement-induced resonance specific to 1D optical lattices [182], a large portion of the phase diagram in Fig. 4.2 can be accessed in this system. If we start from ferromagnetic $V_{\mathrm{ex}} > 0$, the SPT phase transition from the topological phase to the laser-induced Kondo insulating state is possible. This phase transition is protected by the inversion symmetry and the spin π rotation symmetries around the x or y axis, and the only former symmetry stands for the topological properties. On the other hand, if we switch on the laser coupling starting from antiferromagnetic $V_{\mathrm{ex}} < 0$, the ordinary Kondo insulator is first changed into the Néel order, and finally turns into the laser-induced Kondo insulator. This reentrant Kondo transitions associated with the Néel order are stable (at least $T = 0$) if the spin π rotation symmetries are preserved.

Chapter 4

Topological Pumping in Interacting Systems

1 Introduction

In this chapter, we focus on a somewhat different topological phenomenon which is called topological pumping. Adiabatic change of parameters of a Hamiltonian sometimes causes nontrivial effects which cannot be found in its instantaneous ground state. Topological pumping, originally proposed by Thouless [231], provides a prototypical example of such phenomena. Thouless considered a 1D band insulator in a periodic lattice potential $V(x) = V(x + a)$. Let us consider an adiabatic shift of the lattice potential $V(x - at/T)$ parametrized by t. Since the lattice potential is periodic, so is the Hamiltonian with respect to its parameter: $H(t + T) = H(t)$. The one-particle quantum states in an energy band are then specified by the wave number k_x and the parameter t. When the lattice potential is adiabatically shifted by varying t, the particles move with the lattice, and the Hamiltonian returns to its original form after a shift by one lattice spacing. The ground state also returns to the initial one as long as the particles stay in the same band. However, the change in the ground state during the cycle can cause a nonvanishing particle current. The total current over one cycle is given by the Chern number, which takes an integer and characterizes topologically distinct classes of the set of one-particle states defined in the (k_x, t) plane. Hence the total current is quantized, and this phenomenon is called the topological Thouless pumping. If we identify the (k_x, t) plane with the 2D reciprocal space, we find that the Thouless pumping shares the same origin as the integer quantum Hall effect [232, 233] in which the quantized pumping corresponds to the quantized Hall conductivity. Owing to its topological nature, the topological pumping is robust against small deformation of the pumping protocol, and can be realized by various types of cycles using lattice models [234, 235, 236, 237]. After almost 30 years since Thouless's prediction, the topological pumping was finally realized experimentally by using ultracold atoms in optical superlattices [139, 140, 141] in which the periodic change of the lattice potential was created by the change of the phase of the standing wave potential. Other schemes of manipulating an optical superlattice for realizing the topological pumping have also been discussed [238, 239, 240, 241].

Since the Thouless pumping corresponds to the integer quantum Hall effect, it is natural to ask whether we can obtain topological pumping which is a counterpart of quantum Hall states in interacting systems, such as fractional quantum Hall (FQH) states (see Sec. 3.2 in Chap. 1). In this chapter, we aim to construct nontrivial classes of topological pumping which correspond to

quantum Hall states created by strong interactions. We first consider topological pumping which mimics the Hall response of the FQH states, and then focus on the case of the bosonic integer quantum Hall (BIQH) state (see Sec. 3.4 in Chap. 1). Based on a quasi-1D limit of quantum Hall states [242, 243, 244, 245], we can systematically construct strongly interacting models of topological pumping and thus naturally extend the connection between the topological pumping and the quantum Hall effect to interacting systems. Interestingly, it is shown that the quasi-1D limit of the BIQH state is given by the Haldane phase [55, 56, 68, 69], which is a celebrated example of a SPT phase in one dimension [246, 76, 77] as we have seen in Sec. 3.3 of Chap. 1. The mechanism of the resulting topological pumping is interpreted in terms of changes in polarizations between quantized values that correspond to two distinct gapped phases in the presence of the inversion symmetry. The obtained topological pumping intertwining two-component bosons provides novel interaction-induced topological pumping, and suggests an intriguing connection between the 2D topological phases and 1D gapped phases.

2 Topological pumping as flux insertion through a thin torus

In this section, we explain our idea for obtaining models of 1D topological pumping systematically from a so-called thin-torus limit of 2D quantum Hall states [242, 243, 244, 245] Let us consider a bosonic or fermionic system composed of N particles of charge Q and mass M in a uniform magnetic field B on a 2D torus of size $L_x \times L_y$. We take the Landau gauge $\boldsymbol{A} = (0, Bx)$ and assume $QB > 0$. The total number of flux quanta piercing the system is $N_\phi = \frac{L_x L_y}{2\pi\ell^2}$, where $\ell = \sqrt{\frac{\hbar}{QB}}$ is the magnetic length. The filling factor is defined as $\nu = N/N_\phi$. The single-particle spectrum is given by the Landau levels $E_n = \hbar\Omega(n + \frac{1}{2})$ $(n = 0, 1, \dots)$, where $\hbar\Omega = \frac{\hbar^2}{2M\ell^2}$ is the cyclotron energy. The states in each level are N_ϕ-fold degenerate, and labeled in the present gauge by the wave number $k_m = \frac{2\pi m}{L_y}$ $(m = 0, 1, \cdots, N_\phi - 1)$ in the y direction. In particular, the lowest-Landau-level (LLL) wavefunctions are given by [247, 248]

$$\psi_m(\boldsymbol{r}) = \frac{1}{\sqrt{\pi^{1/2}\ell L_y}} \sum_{n\in\mathbb{Z}} \exp\Big[-\frac{1}{2\ell^2}(x - k_m\ell^2 - nL_x)^2 + i\Big(k_m + \frac{nL_x}{\ell^2}\Big)y\Big]. \tag{4.2.1}$$

This wavefunction is localized around $x = k_m\ell^2 = ma$ with a width ℓ in the x direction, and delocalized in the y direction; see the left panel of Fig. 4.1. Here, $a = 2\pi\ell^2/L_y = L_x/N_\phi$ is the spacing between neighboring wavefunctions, and used as an effective "lattice constant" later.

In Laughlin's flux insertion argument [249], the quantized Hall conductivity can be derived as a response to an adiabatic insertion of a flux quantum through the torus. The effect of flux insertion is expressed by a twisted boundary condition, which results in the replacement $k_m \to k_m + \frac{\phi}{L_y}$ with $0 \le \phi \le 2\pi$. After inserting one flux quantum ($\phi = 2\pi$), the Hamiltonian of the system goes back to its original form. However, each Landau-level orbital shifts its position during this process. Hence, if some of the Landau levels are completely occupied and others are empty, the system exhibits the integer quantum Hall effect. The FQH effect is also understood in a similar manner by taking into account the topological ground-state degeneracy on the torus [248, 250, 40]. In this case, the insertion of one flux quantum transfers the initial ground state to another degenerate ground state, and some integer multiple of flux quanta are required to go back to the initial ground state.

Keeping this picture in mind, let us gradually decrease the length L_y in the y direction while keeping the total area L_xL_y fixed. By identifying the locations $x = ma$ of the LLL orbitals (4.2.1)

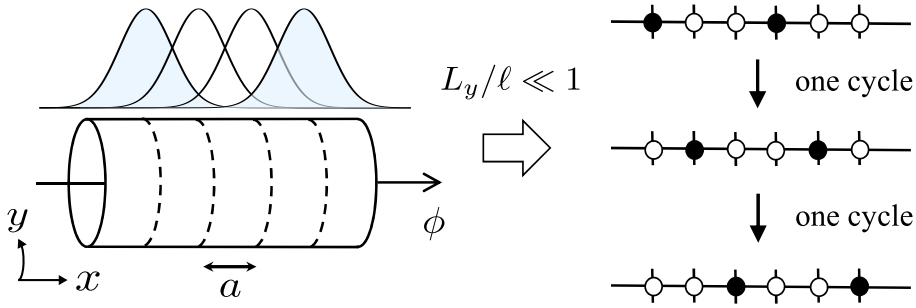

Figure 4.1: Quantum Hall system on a thin torus (left) and topological pumping (right). A flux ϕ (in units of $\hbar/Q$) is inserted through a thin torus on which the LLL orbitals (4.2.1) are formed with a constant spacing a. In a thin-torus limit $L_y/\ell \ll 1$, the flux insertion argument for the Laughlin FQH states can be restated as the change between degenerate CDW ground states by a translation, which results in fractional Thouless pumping. The figure is the case of $\nu = 1/3$.

as a lattice coordinate, the original 2D system can be viewed as an effective 1D lattice model [242, 243, 244, 245]. The effective model contains some long-range interactions, whose coefficients are given by interaction matrix elements with respect to the LLL orbitals on concerned sites. However, as we decrease L_y, the lattice constant a increases, and the LLL orbitals are mutually separated further. Interactions for longer distances are thus suppressed more rapidly in this process, and the physics for $L_y/\ell \ll 1$ is expected to be dominated by a few interaction terms at short distances.

If the ground state of a given quantum Hall state is smoothly changed without closing an excitation gap with decreasing L_y, the ground state is expected to gradually acquires a 1D character owing to the suppression of interactions for long distances. We can then view the ground state on a thin torus as the 1D lattice counterpart of the quantum Hall state. It is then expected that the insertion of a flux quantum through the thin torus induces quantized current in the x direction. This phenomenon can be viewed as the topological pumping in the 1D model [251, 252].

3 Fractional charge pumping in the thin-torus limit of FQH states

Let us illustrate the above idea using the simplest FQH state, the Laughlin state of fermions at $\nu = 1/3$. It was shown that with decreasing L_y, the $\nu = 1/3$ Laughlin state is smoothly deformed into a charge-density-wave (CDW) state in which every third site is occupied by a particle [243]. Here, density-density interactions for nearest-neighbor and next-nearest-neighbor pairs of sites play a dominant role and stabilize the CDW state. If a flux quantum is adiabatically inserted through a thin torus, the LLL orbitals shift their positions by one lattice spacing a, and the CDW ground state changes into another degenerate ground state [252] as shown in Fig. 4.1. The total current during this shift of the ground state is equal to $1/3$ if averaged in space; this corresponds to the fractional Hall conductivity $\sigma_{xy} = \frac{1}{3}\frac{Q^2}{h}$ of the Laughlin state. Hence, as expected, the flux insertion for the 1D counterpart of the FQH state results in fractional Thouless pumping. Similarly to Laughlin's argument for the FQH effect [250], here the degeneracy of the ground states is essential in obtaining the fractional pumping.

For a filling fraction with a denominator larger than 3, it is not clear whether the FQH state is adiabatically connected to a CDW state with decreasing L_y. This is because in a thin torus, the

density-density interactions that stabilize a CDW state can severely compete with other interaction terms in which two particles hop in a center-of-mass-conserving manner [243, 244, 245, 253, 254]. However, if we keep only the density-density interactions and neglect other interaction terms, the system exhibits a CDW ground state with q-fold degeneracy at every rational filing fraction $\nu = p/q$ (with p and q being coprime) [244, 245, 243, 255]. The adiabatic shift of such a CDW state by one lattice spacing clearly results in fractional Thouless pumping. Similar schemes for realizing fractional pumping by CDW states have been discussed in literature [256, 257, 258, 259, 260], especially in connection with the synthetic dimension technique [135] in cold atoms (see also Sec. 4.2 of Chap. 1). In this technique, infinite-range interactions in the synthetic dimension stabilize CDW ground states [257, 258, 260, 261, 262]. Although the topological pumping constructed here is just a translational operation of the entire system and seems to be somewhat trivial, we will see that the case of the BIQH state provides more nontrivial topological pumping.

4 Thin-torus limit of the bosonic integer quantum Hall state

Based on the correspondence between the quantum Hall states on the thin torus and the topological pumping, we here construct the thin-torus counterpart of the BIQH state. Let us start with two-component bosons in a uniform magnetic field on a torus described by the Hamiltonian

$$\begin{aligned} H = &\sum_{\alpha=1,2} \int d^2\boldsymbol{r} \Psi^{(\alpha)\dagger}(\boldsymbol{r}) \frac{[\boldsymbol{p} - Q\boldsymbol{A}(\boldsymbol{r})]^2}{2M} \Psi^{(\alpha)}(\boldsymbol{r}) \\ &+ \sum_{\alpha,\beta} \frac{g^{(\alpha\beta)}}{2} \int d^2\boldsymbol{r} \Psi^{(\alpha)\dagger}(\boldsymbol{r}) \Psi^{(\beta)\dagger}(\boldsymbol{r}) \Psi^{(\beta)}(\boldsymbol{r}) \Psi^{(\alpha)}(\boldsymbol{r}), \end{aligned} \tag{4.4.1}$$

where $\Psi^{(\alpha)}(\boldsymbol{r})$ ($\alpha = 1, 2$) denotes the bosonic field operator for the α-th component. We assume repulsive contact interactions $g^{(\alpha\beta)} > 0$ between particles, and set $g^{(11)} = g^{(22)} \equiv g$ for simplicity. The filling factor for each component is set to unity so that the total filling factor is given by $\nu = 1 + 1$. The system possesses the U(1)×U(1) symmetry associated with the particle number conservation in each component. Through exact diagonalization analyses [88, 89, 90], it was shown that the BIQH state described by the effective Chern-Simons theory (1.3.50) appears when the ratio of the intercomponent to intracomponent interactions, $\delta \equiv g^{(12)}/g$, is close to unity.

Within the LLL approximation, the field operators are expanded as

$$\Psi^{(\alpha)}(\boldsymbol{r}) = \sum_{m=0}^{N_\phi - 1} b_m^{(\alpha)} \psi_m(\boldsymbol{r}, \phi_\alpha), \tag{4.4.2}$$

where $b_m^{(\alpha)}$ annihilates a particle in the m-th LLL orbital and satisfies the commutation relations $[b_m^{(\alpha)}, b_n^{(\beta)\dagger}] = \delta_{\alpha\beta}\delta_{mn}$ and $[b_m^{(\alpha)}, b_n^{(\beta)}] = 0$. To facilitate later discussions on topological pumping, we have introduced a magnetic flux ϕ_α which couples to the α-th component so that the LLL wave function $\psi_m(\boldsymbol{r}, \phi_\alpha)$ is given by the right-hand side of Eq. (4.2.1) with k_m replaced by $k_m + \frac{\phi_\alpha}{Ly}$. Correspondingly, the positions of the LLL orbitals are shifted to $x = (m + \frac{\phi_\alpha}{2\pi})a$ in the α-th

component. Substituting the expansion (4.4.2) into the Hamiltonian (4.4.1), we obtain

$$H = \frac{1}{2}\hbar\Omega \sum_{\alpha} N^{(\alpha)} + \sum_{\alpha}\sum_{j} \sum_{|n|\le m\le \frac{N_\phi}{2}} V_{mn} b_{j+n}^{(\alpha)\dagger} b_{j+m}^{(\alpha)\dagger} b_{j+m+n}^{(\alpha)} b_j^{(\alpha)} + \sum_{j} \sum_{-\frac{N_\phi}{2}<m,n\le \frac{N_\phi}{2}} V_{mn}^{(12)} (\phi_1-\phi_2) b_{j+n}^{(1)\dagger} b_{j+m}^{(2)\dagger} b_{j+m+n}^{(2)} b_j^{(1)}. \tag{4.4.3}$$

We note that the interactions in this Hamiltonian preserves the center-of-mass position in the x direction. The interaction matrix elements are calculated by using the LLL wavefunctions as [247, 245]

$$V_{mn} = \frac{z_{mn} g}{L_x L_y} \sum_{\boldsymbol{q}} \left[\delta'_{n,n_y} e^{-\frac{1}{2}\boldsymbol{q}^2\ell^2} \cos(q_x k_m \ell^2) + (m \leftrightarrow n) \right], \tag{4.4.4a}$$

$$V_{mn}^{(12)}(\phi) = \frac{g^{(12)}}{L_x L_y} \sum_{\boldsymbol{q}} \delta'_{n,n_y} e^{-\frac{1}{2}\boldsymbol{q}^2\ell^2} \cos\left[q_x \left(k_m - \frac{\phi}{L_y} \right) \ell^2 \right], \tag{4.4.4b}$$

where the sum is over the wave vector $\boldsymbol{q} = (\frac{2\pi n_x}{L_x}, \frac{2\pi n_y}{L_y})$ $(n_x, n_y \in \mathbb{Z})$, δ'_{n,n_y} is the modulo-N_ϕ Kronecker delta, and $z_{mn} = 2^{-\delta_{m,|n|}(1+\delta_{m,0})} 2^{-\delta_{m,N_\phi/2}(1+\delta_{|n|,N_\phi/2})}$ is a factor for fixing the double counting of some terms. If we take the limit $L_x/\ell \to \infty$ (and thus $N_\phi \to \infty$) while keeping L_y/ℓ fixed, these elements are given more simply by

$$V_{mn} = \frac{2 z_{mn} g}{\sqrt{2\pi} L_y \ell} e^{-\frac{1}{2}(k_m^2 + k_n^2)\ell^2}, \tag{4.4.5a}$$

$$V_{mn}^{(12)}(\phi) = \frac{g^{(12)}}{\sqrt{2\pi} L_y \ell} e^{-\frac{1}{2}[(k_m - \phi/L_y)^2 + k_n^2]\ell^2}. \tag{4.4.5b}$$

Let us first consider the case when no flux is inserted through the torus: $\phi_1 = \phi_2 = 0$. When we take the thin-torus limit $L_y \to 0$, the only remaining interactions are on-site ones, which are the $m = n = 0$ components of Eq. (4.4.3). We thus obtain

$$H = \sum_{\alpha=1,2} \sum_{j} V_{00} n_j^{(\alpha)} (n_j^{(\alpha)} - 1) + \sum_{j} V_{00}^{(12)} n_j^{(1)} n_j^{(2)}, \tag{4.4.6}$$

where we ignore the constant kinetic energy of the LLL. The ground state of the thin-torus Hamiltonian (4.4.6) is easily obtained. For $\delta < 1$, where the intracomponent interaction is dominant ($2V_{00} > V_{00}^{(12)}$), the ground state is the product state of Bose Mott insulators

$$\left| \begin{matrix} \cdots & n_j^{(1)} & \cdots \\ \cdots & n_j^{(2)} & \cdots \end{matrix} \right\rangle = \left| \begin{matrix} \cdots & 1\,1\,1\,1 & \cdots \\ \cdots & 1\,1\,1\,1 & \cdots \end{matrix} \right\rangle. \tag{4.4.7}$$

For $\delta > 1$, where the intercomponent interaction is dominant ($2V_{00} < V_{00}^{(12)}$), the ground states are ferromagnetic states

$$\left| \begin{matrix} \cdots & n_j^{(1)} & \cdots \\ \cdots & n_j^{(2)} & \cdots \end{matrix} \right\rangle = \left| \begin{matrix} \cdots & 2\,2\,2\,2 & \cdots \\ \cdots & 0\,0\,0\,0 & \cdots \end{matrix} \right\rangle, \quad \left| \begin{matrix} \cdots & 0\,0\,0\,0 & \cdots \\ \cdots & 2\,2\,2\,2 & \cdots \end{matrix} \right\rangle, \tag{4.4.8}$$

if we fix only the total number of particles. If we fix the number of particles in each component, a phase separation occurs. The point $\delta = 1$, at which $2V_{00} = V_{00}^{(12)}$, is special—the on-site energy is the same for $|n_j^{(1)}, n_j^{(2)}\rangle = |2,0\rangle, |1,1\rangle, |0,2\rangle$, leading to 3^{N_ϕ}-fold degeneracy of the ground state. This macroscopic degeneracy in the thin-torus limit is lifted by fluctuations as we increase L_y.

To obtain a unique ground state at $\delta = 1$, we proceed away from the thin-torus limit by increasing L_y and consider leading fluctuations. The next-leading interactions are the nearest-neighbor ones, which are $V_{10}, V_{10}^{(12)} (= V_{-1,0}^{(12)})$, and $V_{01}^{(12)}$ terms. The $V_{01}^{(12)}$ term involves hopping of particles while the other ones are of an electrostatic type. To discuss the competition of these terms, we restrict ourselves to the low-energy manifold of the Hilbert space spanned by the 3^{N_ϕ}-fold degenerate ground states of Eq. (4.4.6) at $\delta = 1$. The thin-torus ground states (4.4.7) and (4.4.8) for $\delta \neq 1$ also reside in this manifold. In this restricted subspace, in which the constraint $\sum_\alpha n_j^{(\alpha)} = 2$ is satisfied at every site, the operators

$$\boldsymbol{S}_j = \frac{1}{2} \sum_{\alpha,\beta} b_j^{(\alpha)\dagger} \boldsymbol{\sigma}_{\alpha\beta} b_j^{(\beta)} \tag{4.4.9}$$

satisfy the commutation relations of the SU(2) generators and have the fixed magnitude $\boldsymbol{S}_j^2 = 1(1+1)$ as is known in the Schwinger boson formalism [263]. Here, $\boldsymbol{\sigma} = (\sigma^x, \sigma^y, \sigma^z)$ is a set of Pauli matrices. The Hamiltonian can thus be written in terms of the spin-1 operators as

$$H = \sum_j \left[J_{xy} (S_j^x S_{j+1}^x + S_j^y S_{j+1}^y) + J_z S_j^z S_{j+1}^z + D (S_j^z)^2 \right], \tag{4.4.10}$$

where $J_{xy} = 2V_{01}^{(12)}$, $J_z = 2(V_{10} - V_{10}^{(12)})$, and $D = 2V_{00} - V_{00}^{(12)}$. This has the form of the XXZ chain with a single-ion anisotropy [264, 265, 67]. At $\delta = 1$, in particular, since $V_{10} = 2V_{10}^{(12)} = 2V_{01}^{(12)}$, the effective Hamiltonian is given by the spin-1 antiferromagnetic Heisenberg chain

$$H = J \sum_j \boldsymbol{S}_j \cdot \boldsymbol{S}_{j+1}, \tag{4.4.11}$$

where we set $V_{10} \equiv J > 0$. This Hamiltonian has a non-degenerate ground state, that is, the Haldane state. The macroscopic degeneracy of the ground state of Eq. (4.4.6) is thus lifted by the leading fluctuations.

At this stage, it is interesting to compare the phases of the spin-1 chain (4.4.10) [264, 265, 67] with the phase diagram of the original 2D system. The two-component bosons (4.4.1) in two dimensions show a couple of phases when varying the interaction ratio δ (Fig. 4.2) [90]. When δ is small (numerically $\delta \lesssim 0.2$), the two components are nearly decoupled and form the Moore-Read states [266] independently. In the opposite limit, when δ is large (numerically $\delta \gtrsim 2.5$), the 2D ground state exhibits a phase separation. The BIQH state appears around $\delta = 1$ intervening the two limiting cases [88, 89, 90]. Our mapping to a spin chain (4.4.10) qualitatively reproduces these phases as summarized in Fig. 4.2. When L_y/ℓ is sufficiently small, the single-ion anisotropy D is the most dominant term in Eq. (4.4.10). For $\delta < 1$, we have $D > 0$, and the ground state is a large-D state, which is equivalent to the doubled Mott insulators in Eq. (4.4.7). For a single-component Bose gas at the filling factor $\nu = 1$, it was shown that the ground state in the thin-torus limit is given by a Bose Mott insulator $|\cdots\ n_j^{(\alpha)}\ \cdots\rangle = |\cdots\ 1\ 1\ 1\ 1\ \cdots\rangle$, and then two CDW states $|\cdots\ n_j^{(\alpha)}\ \cdots\rangle = |\cdots\ 2\ 0\ 2\ 0\ \cdots\rangle$ and $|\cdots\ 0\ 2\ 0\ 2\ \cdots\rangle$ become nearly degenerate with the ground state as we increase L_y/ℓ; these three states naturally evolve into the three-fold degenerate ground

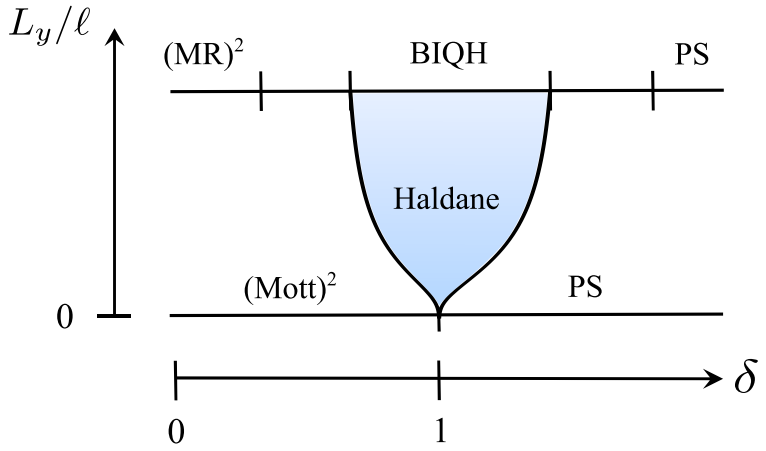

Figure 4.2: Schematic phase diagram of two-component bosons (4.4.1) at $\nu = 1 + 1$ in the space of the ratio of the intercomponent to intracomponent interactions, $\delta = g^{(12)}/g$, and the length L_y in the y direction. A quasi-1D limit $L_y/\ell \ll 1$ is described by the spin-1 chain (4.4.10) while the 2D phase diagram has been studied in Ref. [90]. The product of Bose Mott insulators [(Mott)^2] in the quasi-1D limit is expected to evolve into the the product of Moore-Read states [(MR)^2] for $\delta \lesssim 0.2$ in the 2D case. A phase separation (PS) occurs for $\delta > 1$ in the quasi-1D limit and for $\delta \gtrsim 2.5$ in the 2D case. A Haldane phase that intervenes between the regions of (Mott)^2 and PS in the quasi-1D limit is expected to evolve into the BIQH phase in the 2D system.

states of the bosonic Moore-Read state on a 2D torus [267]. Similarly, the doubled Mott insulators in Eq. (4.4.7) is expected to evolve into the doubled Moore-Read states found in the 2D system. For $\delta > 1$, we have $D < 0$ and $J_z < 0$, and the spin chain (4.4.10) exhibits ferromagnetic ground states as in Eq. (4.4.8); if the total magnetization of the system is fixed at zero, a phase separation occurs as found in the 2D system. As we increase L_y/ℓ, the Haldane phase appears between the large-D and ferromagnetic phases in the spin-chain model, and its range along the δ axis gradually increases. Owing to the uniqueness of the ground state and high entanglement between the two components, it is natural to speculate that this phase evolves into the BIQH phase in the 2D case.

Next, let us consider the thin-torus limit in the case when some fluxes ϕ_α are inserted through the torus. Since the Hamiltonian (4.4.3) depends on the fluxes only through $\phi_1 - \phi_2$, we set $\phi_1 \neq 2\pi n$ ($n \in \mathbb{Z}$) and $\phi_2 = 0$ without loss of generality. In this case, since the flux causes lattice mismatch between the two components, the only remaining interaction in the limit $L_y/\ell \to 0$ is the on-site intracomponent one V_{00}, and the intercomponent interactions completely disappear. The ground state is thus the doubled Mott insulators (4.4.7) at any δ. We note that this fact does not contradict the above identification of the BIQH state with the Haldane phase, since the flux insertion breaks the inversion symmetry of the system (except at $\phi_1 = \pi$) and thus there is no clear distinction between the Haldane phase and the Bose Mott insulator [268, 213, 237]. In the next section, we show that the change in the ground state during the adiabatic flux insertion is related to the Hall response of the BIQH state, leading to topological pumping in the quasi-1D system.

5 Off-diagonal topological pumping in the thin-torus limit

In this section, we describe the 1D topological pumping which mimics the BIQH effect, and thereby reinterpret the fact that the thin-torus counterpart of the BIQH state is the Haldane phase. We start from the two-component Bose system (4.4.1) on a 2D torus, and consider its Hall response. As discussed in Sec. 4, we introduce a magnetic flux ϕ_α ($\alpha = 1, 2$) through the torus, which results in the twisted boundary condition for the α-th component in the y direction. We also introduce a magnetic flux θ_α ($\alpha = 1, 2$) through the other direction of the torus, which results in the analogous twisted boundary condition in the x direction. Then the Hall response of the α-th component to the flux insertion for the β-th component ($\alpha, \beta = 1, 2$) can be expressed by the many-body Chern number [252]

$$C_{\alpha\beta} = \frac{1}{2\pi i}\int_0^{2\pi} d\theta_\alpha \int_0^{2\pi} d\phi_\beta (\langle \partial_{\theta_\alpha}\psi | \partial_{\phi_\beta}\psi\rangle - \langle \partial_{\phi_\beta}\psi | \partial_{\theta_\alpha}\psi\rangle), \tag{4.5.1}$$

where $|\psi(\theta_\alpha, \phi_\beta)\rangle$ is the many-body ground state for the twists θ_α and ϕ_β for the α- and β-th components in the x and y directions, respectively, while the other twisting angles are set to zero. The Chern-Simons theory (1.3.50) of the BIQH effect corresponds to $C_{11} = C_{22} = 0$ and $C_{12} = C_{21} = 1$. From this effective theory, we can read off that a probe electric field for *one* component induces the quantized Hall response in *the other*. These responses result in "off-diagonal" topological pumping in the thin-torus limit as we see below.

Hereafter we focus on the responses corresponding to C_{11} and C_{21}. These can be analyzed by setting $\phi_2 = 0$ and adiabatically changing the pumping parameter $t \equiv \frac{\phi_1}{2\pi} T$ from 0 to T. The Hall current in the x direction is identified as the pumped charge. For fixed t, it is useful to introduce the Berry phase

$$\gamma_\alpha(t) = -\int_0^{2\pi} d\theta_\alpha \, \langle \psi(\theta_\alpha, t)| \, \partial_{\theta_\alpha} \, |\psi(\theta_\alpha, t)\rangle \pmod{2\pi}, \tag{4.5.2}$$

which is associated with the change in the ground state $|\psi(\theta_\alpha, t)\rangle$ when θ_α is adiabatically changed from 0 to 2π. The Chern number (4.5.1) can then be rewritten as

$$C_{\alpha,\beta=1} = -\frac{1}{2\pi}\int_0^T dt \; \partial_t \gamma_\alpha(t). \tag{4.5.3}$$

In this expression, the quantized Hall response or equivalently the quantized charge pumping can be understood as $2\pi n$ ($n \in \mathbb{Z}$) change in the Berry phase $\gamma_\alpha(t)$ over the pumping process [269].

A more intuitive understanding of the quantized pumping can be gained by introducing the polarization. To introduce it, we define

$$z_\alpha(t) = \langle \psi(t)| \exp\left[\frac{2\pi i}{L_x}\int d\boldsymbol{r} \; x \Psi^{(\alpha)\dagger}(\boldsymbol{r})\Psi^{(\alpha)}(\boldsymbol{r})\right] |\psi(t)\rangle \,, \tag{4.5.4}$$

where $|\psi(t)\rangle = |\psi(\theta_\alpha = 0, t)\rangle$. This is convenient in describing the center-of-mass position of the particles in the α-th component in the x direction since the position x is defined modulo L_x under the periodic boundary condition. Within the LLL approximation, we can exploit the fact that j-th LLL orbital for the α-th component is localized around $x_\alpha(j) = (j + \frac{t}{T}\delta_{\alpha,1})a$ in the x direction

(with larger spacing a for smaller L_y/ℓ), and approximate $z_\alpha(t)$ as

$$z_\alpha(t) \approx \langle\psi(t)|\exp\Big[\frac{2\pi i}{N_\phi a}\sum_j x_\alpha(j)n_j^{(\alpha)}\Big]|\psi(t)\rangle$$
$$= \langle\psi(t)|\exp\Big[\frac{2\pi i}{N_\phi}\sum_j jn_j^{(\alpha)} + \frac{2\pi it}{T}\delta_{\alpha,1}\Big]|\psi(t)\rangle\,. \tag{4.5.5}$$

This resembles the expectation value of the Lieb-Schultz-Mattis twist operator [270, 271, 272, 273, 274, 275]. The phase of $z_\alpha(t)$ gives the polarization [276, 277]

$$P_\alpha(t) = \frac{1}{2\pi}\mathrm{Im}\ln z_\alpha(t) \pmod 1. \tag{4.5.6}$$

Importantly, the polarization is directly related to the Berry phase as [278, 279, 280, 276]

$$P_\alpha(t) = -\frac{1}{2\pi}\gamma_\alpha(t). \tag{4.5.7}$$

The Chern number can therefore be rewritten as the change in the polarization over the pumping cycle:

$$C_{\alpha,\beta=1} = \Delta P_\alpha = \int_0^T dt\ \partial_t P_\alpha(t). \tag{4.5.8}$$

The BIQH effect should thus correspond to the topological pumping with $\Delta P_1 = 0$ and $\Delta P_2 = 1$.

Let us now discuss in detail the topological pumping in the thin-torus limit of the BIQH state. The pumping protocol in the present case is not just the translation but involves the change of intercomponent interactions, in sharp contrast with the FQH cases discussed in Sec. 3. Since the Hamiltonian (4.4.3) in the LLL basis is invariant under the combined operations of the spatial inversion $j \to N_\phi - j$ and the interchange of two components $1 \leftrightarrow 2$, $z_\alpha(t)$ in Eq. (4.5.5) satisfies

$$z_1(t) = e^{2\pi it/T} z_2^*(t), \tag{4.5.9}$$

which indicates $P_1(t) + P_2(t) = t/T$. Thus, $\Delta P_1 = 0$ implies $\Delta P_2 = 1$ and vice versa. Furthermore, by exploiting the invariance of the pumping protocol under the combined operations of the spatial inversion and time reversal $t \to -t$. we find $P_\alpha(-t) = -P_\alpha(t)$, from which we obtain $\Delta P_\alpha = 2\int_0^{T/2} dt\ \partial_t P_\alpha(t)$. Thus, half of the expected changes $\Delta P_\alpha = \delta_{\alpha,2}$ in the polarizations over one cycle must occur during $t \in [0, T/2]$:

$$P_\alpha(T/2) - P_\alpha(0) = \frac{1}{2}\delta_{\alpha,2}. \tag{4.5.10}$$

To discuss the variation of the polarizations $P_\alpha(t)$ as functions of t, it is important to notice that the system possesses the spatial inversion symmetry at $t = 0$ and $t = T/2$. Therefore, the polarization P_α must be quantized to 0 or $1/2$ at these values of t. It is known that in the presence of the inversion symmetry, a change in the polarization between these quantized values in general signals a phase transition [273, 274]. The polarization can therefore be used as an order parameter for detecting 1D topological phases protected by the inversion symmetry [273, 274, 281, 220]. Similar results can also be obtained through the quantization of the Berry phase [282, 283, 284, 285, 286]. At $t = 0$, the thin-torus limit of the BIQH state is given by the Haldane state as discussed in

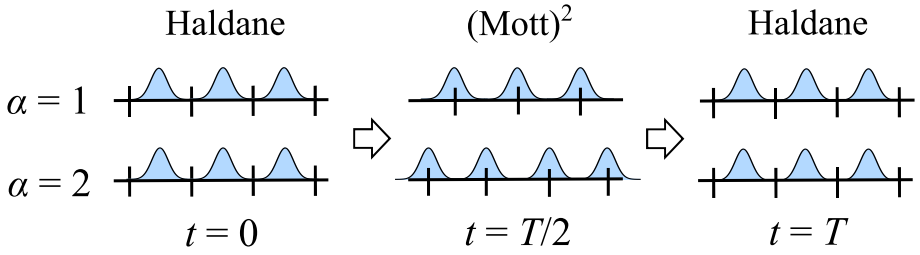

Figure 4.3: Schematic picture of of the off-diagonal topological pumping in the thin-torus limit of the BIQH state. The upper and lower chains describe the first and second components, respectively.

Sec. 4; the Haldane phase is known to be a topological phase protected by the inversion symmetry [246, 76, 77], and has the polarizations [273, 274]

$$P_1(0) = P_2(0) = N_\phi/2. \tag{4.5.11}$$

At $t = T/2$, the ground state in the thin-torus limit is given by the doubled Mott insulators; a direct calculation using Eq. (4.4.7) yields

$$P_1(T/2) = N_\phi/2, \quad P_2(T/2) = (N_\phi + 1)/2. \tag{4.5.12}$$

The Haldane phase and the doubled Mott insulators have the different polarizations (4.5.11) and (4.5.12), and thus are distinct phases as long as the system possesses the inversion symmetry. The topological pumping can be interpreted as a process of connecting between the two phases smoothly by breaking the inversion symmetry. The idea of utilizing symmetry-breaking perturbations to connect between otherwise distinct gapped phases has also been used in other examples of topological pumping such as those based on the Su-Schrieffer-Heeger model [234, 235, 287], the spin-Peierls phases [236] (equivalent to an interacting Su-Schrieffer-Heeger model via the Jordan-Wigner transformation), and the Haldane insulator phase of an extended Bose-Hubbard model [237]. We note that the polarizations in Eqs. (4.5.11) and (4.5.12) are consistent with the relations (4.5.10); conversely, the relations (4.5.10) require the appearance of topologically distinct phases (in an inversion-symmetry-protected sense) at $t = 0$ and $T/2$. This gives an explanation on why the Haldane phase, a typical example of a 1D SPT phase, should emerge in the thin-torus limit of the BIQH state.

Figure 4.3 summarizes the process of the off-diagonal topological pumping in the thin-torus limit. The Haldane phase at $t = 0$ can intuitively be described as localization of bosons at bonds of the lattice in a way similar to that of one-component bosons [213]. By shifting the lattice for the first component, the inversion symmetry is broken and the ground state is smoothly deformed into the doubled Mott insulators at $t = T/2$, and finally returns to the original ground state at $t = T$. During this process, the bosons in the second component are pumped by one lattice spacing while the bosons in the first component stay around the same positions.

Two remarks are in order. First, although the Haldane phase in the spin-1 chain can be protected not only by the inversion symmetry but also by the time-reversal or the spin rotation symmetry [246, 76, 77], the latter two symmetries do not protect the Haldane phase in the case of soft-core bosons as in the present case [268, 213, 237]. This is because the spin-1 degrees of freedom required for the symmetry protection argument are not perfectly formed in the presence of fluctuations in on-site particle numbers. The inversion symmetry is thus the only symmetry that protects the

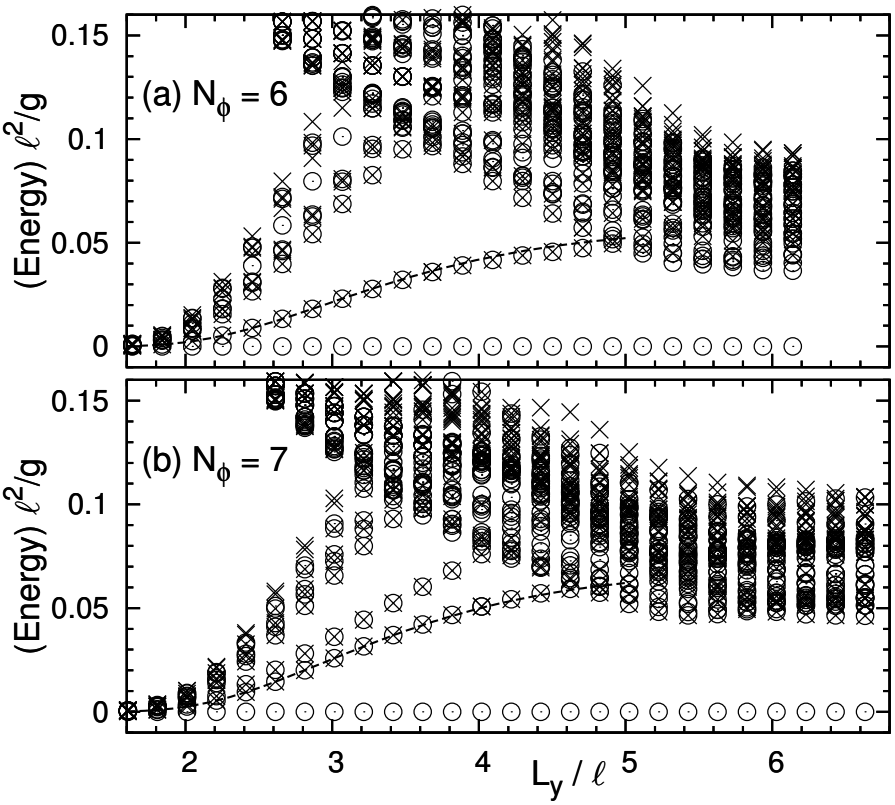

Figure 4.4: Energy spectrum of the Hamiltonian (4.4.3) as a function of L_y/ℓ for (a) $N_\phi = 6$ and (b) $N_\phi = 7$. The ground-state energy is subtracted from the spectrum. Circles indicate eigenenergies in the equal-population case $N_1 = N_2 = N_\phi$. Crosses indicates eigenenergies in the minimally imbalanced case $(N_1, N_2) = (N_\phi + 1, N_\phi - 1)$. The two lowest energies for each pseudomomentum are shown. The data for the largest L_y/ℓ correspond to the case of $L_x = L_y$. Dashed lines indicate the energy gaps $0.721J$ and $0.857J$ of the spin-1 Heisenberg chain (4.4.11) with $N_\phi = 6$ and 7 spins, respectively, where J is given by $V_{10} = 2V_{10}^{(12)}$ in Eq. (4.4.5) (we note that the gap in the thermodynamic limit [288, 289] is given by $0.410J$).

Haldane phase at $t = 0$ in the present case. The second remark is on the mapping to a spin-1 chain done in Sec. 4. In the mapping from the thin-torus Hamiltonian to a spin chain in the FQH cases, the inversion symmetry is sometimes broken since the mapping process involves grouping of several neighboring sites starting from CDW ground states [253, 254]. In the case of the BIQH state, in contrast, the mapping to a spin chain retains the inversion symmetry of the original system, since each spin-1 degree of freedom is composed of bosons at the same site.

To support the above picture of topological pumping, we have performed exact diagonalization calculations for the Hamiltonian (4.4.3) with the number of flux quanta up to $N_\phi = 7$. We consider contact interactions with $g^{(12)} = g$. Figure 4.4 presents the energy spectrum as a function of L_y/ℓ. The ground state is found to remain in the sector with zero pseudomomentum, indicating that the BIQH state in two dimension is smoothly deformed into the Haldane state in the thin-torus limit. For $L_y/\ell \lesssim 5$, the energy gap above the ground state agrees well with the finite-size energy gap of the spin-1 Heisenberg chain (4.4.11) (dashed lines) calculated by KOBEPACK [290]. Reflecting

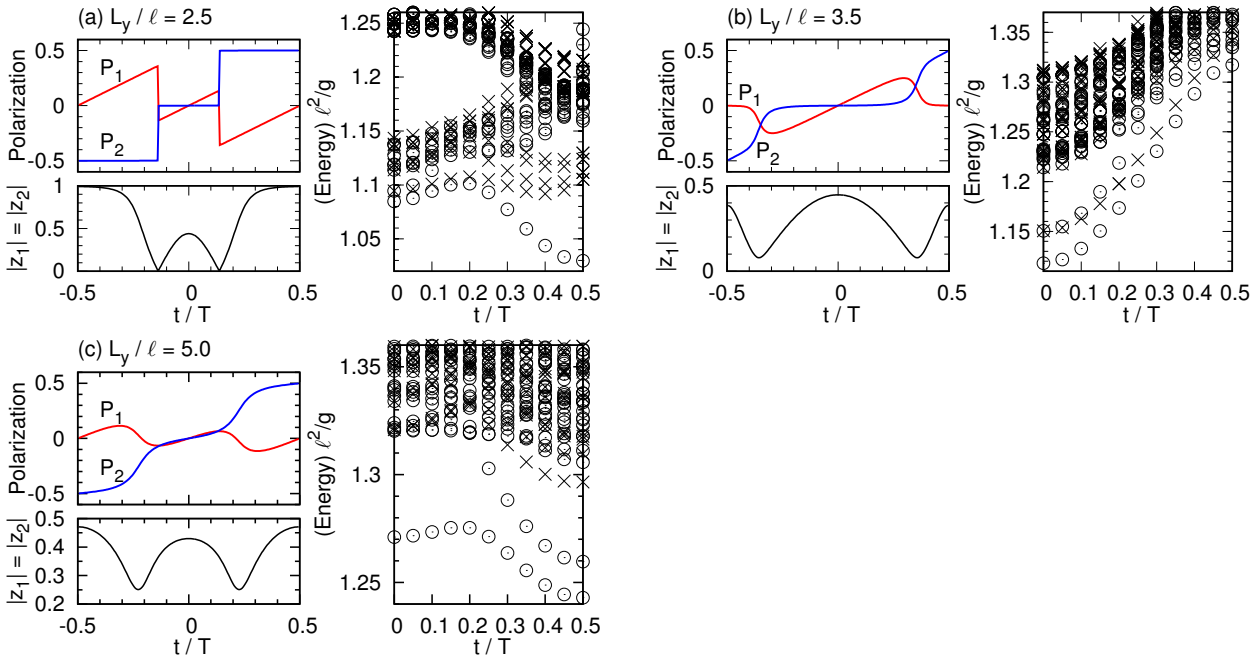

Figure 4.5: The polarizations P_α (left top), the amplitudes $|z_1| = |z_2|$ of the twist operators (left bottom), and the energy spectrum (right) as functions of the pumping parameter $t \in [-T/2, T/2)$, for $N_\phi = 6$ and (a) $L_y/\ell = 2.5$, (b) 3.5, and (c) 5.0. Circles and crosses indicates eigenenergies in the equal-population and minimally imbalanced cases, respectively, as in Fig. 4.4. Since the energy spectrum is symmetric around $t = 0$, it is shown only for $t \in [0, T/2]$.

the large ground-state degeneracy in the thin-torus limit, a large number of eigenenergies collapse onto the ground-state energy with decreasing L_y/ℓ. For $L_y/\ell \gtrsim 5$, the energy gap stay around a constant value, indicating the convergence to a 2D system. Figure 4.5 presents the polarizations P_α, the amplitudes $|z_1| = |z_2|$ of the twist operators, and the energy spectrum as functions of the pumping parameter t. The ground state is found to remain in the zero-pseudomomentum sector in this process also. The calculated polarizations smoothly connect between Eqs. (4.5.11) and (4.5.12) for the Haldane state ($t = 0$) and the doubled Mott insulators ($t = \pm T/2$). While the polarization of the first component stays around $P_1 = 0$, the second component shows $\Delta P_2 = 1$ over the cycle, clearly signaling the off-diagonal topological pumping. As we decrease L_y/ℓ, long-range interactions are suppressed and the system gradually acquires a 1D character. Correspondingly, the change in the polarization becomes shaper in the quasi-1D limit. A rapid change in the center-of-mass position (and thus the polarization) has also been observed in 1D topological pumping [139, 140, 239, 241]. When the rapid crossover from the Haldane state to the doubled Mott insulators occurs, the energy gap becomes small and the amplitudes $|z_1| = |z_2|$ of the twist operators decrease. This indicates the increase in the localization length of the many-body wavefunction in this regime—while $|z_\alpha|$ converges to unity in the thermodynamic limit in 1D gapped systems, its value can be suppressed when the system size is smaller than or comparable to the localization length [277, 274, 273]. This behavior can be explained by the suppression of on-site particle number fluctuations when decreasing L_y/ℓ: If such fluctuations are completely absent, the pumping cycle is described by the spin-1 chain model (4.4.10), in which the Haldane phase and the doubled Mott insulators cannot be connected without closing a gap.

6 Summary of this chapter

In summary, we have constructed strongly interacting models of topological pumping by using the thin-torus limit of 2D quantum Hall states. The thin-torus limit of the FQH states is given by CDW ground states; adiabatically connecting between degenerate CDW ground states gives the fractional Thouless pumping. As a more nontrivial example, we have constructed topological pumping which corresponds to the BIQH effect of two-component bosons. The quasi-1D counterpart of the BIQH state is identified as the Haldane phase, and adiabatically connecting between the topological Haldane phase and the trivial doubled Mott insulators constitute the off-diagonal topological pumping in which the translation of the lattice potential for one component induces a current in the other. We have elucidated the nature of the topological pumping via the change in the polarizations between inversion-symmetry-protected quantized values. Since the idea of connecting between the Haldane and trivial phases by inversion-symmetry-breaking perturbations does not depend on the details of the system, the obtained off-diagonal topological pumping should not be limited to the thin-torus model considered in this paper. While the time-reversal symmetry is broken in quantum Hall states and related topological pumping, it is an intriguing direction to construct a bosonic version of time-reversal-symmetric $\mathbb{Z}_2$ pumping [291] which may correspond to 2D bosonic topological insulators [292, 293].

Chapter 5

Conclusion

In this thesis, we have concentrated on two aspects of quantum many-body systems: the Kondo effect and topological phenomena. Motivated by recent development of experimental technique in ultracold atoms, we have proposed possible realizations of such phenomena and have investigated their properties.

In Chap. 2, we have proposed that intense laser application to alkaline-earth(-like) atoms induces a novel Kondo effect. The peculiar properties of this laser-induced Kondo effect consist of two kinds. The first point is that we can manipulate the Kondo effect with high controllability. While the Kondo interactions in ordinary solid state systems are intrinsic to materials and are difficult to control, here the Kondo coupling in this setup can be controlled by varying the laser strength and frequency. Also, since the laser can be manipulated in real time, the laser-induced Kondo effect provides a versatile platform to investigate the Kondo effect in nonequilibrium situations. In fact, we have demonstrated that the laser-induced Kondo effect indeed persists under the strong irradiation, overcoming the heating effect. The other peculiar feature of the laser-induced Kondo effect is the laser-spin coupling. Since the polarization of the laser field couples with the spin degrees of freedom of atoms, the laser-induced Kondo effect realizes an unusual fixed point where the Kondo "singlet" is different from the ordinary one. We have shown in Chap. 3 that this laser-induced Kondo effect is certainly distinguished from the ordinary Kondo state by comparing their symmetry eigenvalues in terms of the spin π rotation. Thus the ultracold alkaline-earth atoms offer a rare example of realization of the both types of the Kondo effect.

In Chap. 3, we have further extended the analysis of the Kondo lattice in ultracold atoms to 1D systems, and have shown that the 1D Kondo lattice hosts a SPT phase. Although the 1D Kondo lattice is rarely realized in solid state systems, ultracold atoms can realize the SPT phase and the associate topological phase transition in a controllable manner. We have demonstrated that the SPT phase of the 1D Kondo lattice is only protected by the inversion symmetry, in sharp contrast with its strong-coupling counterpart, the Haldane phase. This feature is due to the existence of the charge degrees of freedom to the Kondo lattice. We have elucidated that the charge mode plays a key role to understand the difference between the fermionic SPT phase and the bosonic SPT phase realized in the strong coupling limit.

In Chap. 4, we have focused on topological pumping, which was recently realized in cold-atom experiments. Here we have presented a systematic construction of topological pumping which corresponds to quantum Hall states created by strong interactions. By utilizing the thin-torus limit of fractional quantum Hall states, we have shown that the fractional charge pumping emerges

from the sliding of CDW states. Furthermore, we have constructed interaction-induced topological pumping which is obtained from the thin-torus limit of the bosonic integer quantum Hall state. This topological pumping is given by the Haldane phase, and conversely the condition of the off-diagonal topological pumping naturally explains why the Haldane phase appears in the thin-torus counterpart of the bosonic integer quantum Hall state. Since the mechanism of the topological pumping does not depend on details of the system and only relies on the picture of connecting between two topological distinct phases, our finding offers a systematic understanding of topological pumping in interacting systems.

Bibliography

[1] J. Kondo, Progress of Theoretical Physics **32**, 37 (1964).

[2] A. C. Hewson, *The Kondo Problem to Heavy Fermions* (Cambridge University Press, Cambridge, 1993).

[3] P. Coleman, *Handbook of Magnetism and Advanced Magnetic Materials* (John Wiley & Sons, New York, 2007), URL `https://arxiv.org/abs/cond-mat/0612006`.

[4] P. Coleman, *Introduction to Many-Body Physics* (Cambridge University Press, Cambridge, 2015).

[5] K. Yosida, Phys. Rev. **147**, 223 (1966).

[6] P. W. Anderson, G. Yuval, and D. R. Hamann, Phys. Rev. B **1**, 4464 (1970).

[7] P. W. Anderson, J. Phys. C: Solid State Phys. **3**, 2436 (1970).

[8] P. Nozières, Journal of Low Temperature Physics **17**, 31 (1974).

[9] K. Yosida and K. Yamada, Progress of Theoretical Physics Supplement **46**, 244 (1970).

[10] K. Yamada, Progress of Theoretical Physics **53**, 970 (1975).

[11] K. Yosida and K. Yamada, Progress of Theoretical Physics **53**, 1286 (1975).

[12] K. Yamada, Progress of Theoretical Physics **54**, 316 (1975).

[13] K. G. Wilson, Rev. Mod. Phys. **47**, 773 (1975).

[14] N. Andrei, Phys. Rev. Lett. **45**, 379 (1980).

[15] N. Andrei, K. Furuya, and J. H. Lowenstein, Rev. Mod. Phys. **55**, 331 (1983).

[16] P. B. Wiegmann, Journal of Physics C: Solid State Physics **14**, 1463 (1981).

[17] A. M. Tsvelick and P. B. Wiegmann, Advances in Physics **32**, 453 (1983).

[18] P. Wiegmann, Physics Letters A **80**, 163 (1980).

[19] N. Kawakami and A. Okiji, Physics Letters A **86**, 483 (1981).

[20] I. Affleck, Nuclear Physics B **336**, 517 (1990).

[21] I. Affleck and A. W. Ludwig, Nuclear Physics B **352**, 849 (1991).

[22] I. Affleck and A. W. Ludwig, Nuclear Physics B **360**, 641 (1991).

[23] I. Affleck, arXiv: cond-mat/9512099 (1995).

[24] P. W. Anderson, Phys. Rev. **124**, 41 (1961).

[25] J. R. Schrieffer and P. A. Wolff, Phys. Rev. **149**, 491 (1966).

[26] D. M. Newns and N. Read, Adv. Phys. **36**, 799 (1987).

[27] P. Coleman, Phys. Rev. B **29**, 3035 (1984).

[28] P. Coleman, Phys. Rev. B **35**, 5072 (1987).

[29] M. A. Ruderman and C. Kittel, Phys. Rev. **96**, 99 (1954).

[30] T. Kasuya, Progress of Theoretical Physics **16**, 45 (1956).

[31] K. Yosida, Phys. Rev. **106**, 893 (1957).

[32] S. Doniach, Physica B+C **91**, 231 (1977).

[33] L. D. Landau and E. M. Lifshitz, *Statistical Physics Part 1* (Butterworth-Heinemann, Oxford, 1980), 3rd ed.

[34] X.-G. Wen, Int. J. Mod. Phys. B **4**, 239 (1990).

[35] D. C. Tsui, H. L. Stormer, and A. C. Gossard, Phys. Rev. Lett. **48**, 1559 (1982).

[36] R. B. Laughlin, Phys. Rev. Lett. **50**, 1395 (1983).

[37] X. G. Wen, F. Wilczek, and A. Zee, Phys. Rev. B **39**, 11413 (1989).

[38] X. G. Wen, Phys. Rev. B **44**, 2664 (1991).

[39] A. Kitaev, Annals of Physics **303**, 2 (2003).

[40] X. G. Wen and Q. Niu, Phys. Rev. B **41**, 9377 (1990).

[41] A. Kitaev and J. Preskill, Phys. Rev. Lett. **96**, 110404 (2006).

[42] M. Levin and X.-G. Wen, Phys. Rev. Lett. **96**, 110405 (2006).

[43] F. Wilczek, Phys. Rev. Lett. **49**, 957 (1982).

[44] D. Arovas, J. R. Schrieffer, and F. Wilczek, Phys. Rev. Lett. **53**, 722 (1984).

[45] A. Kitaev, Annals of Physics **321**, 2 (2006).

[46] C. Nayak, S. H. Simon, A. Stern, M. Freedman, and S. Das Sarma, Rev. Mod. Phys. **80**, 1083 (2008).

[47] M. Oshikawa and T. Senthil, Phys. Rev. Lett. **96**, 060601 (2006).

[48] X. G. Wen, Phys. Rev. B **41**, 12838 (1990).

[49] X. Chen, Z.-C. Gu, Z.-X. Liu, and X.-G. Wen, Phys. Rev. B **87**, 155114 (2013).

[50] B. Zeng, X. Chen, D.-L. Zhou, and X.-G. Wen, *Quantum Information Meets Quantum Matter – From Quantum Entanglement to Topological Phase in Many-Body Systems* (arXiv: 1508.02595, 2015), URL `http://arxiv.org/abs/1508.02595`.

[51] F. D. M. Haldane, Phys. Rev. Lett. **61**, 2015 (1988).

[52] C. L. Kane and E. J. Mele, Phys. Rev. Lett. **95**, 226801 (2005).

[53] C. L. Kane and E. J. Mele, Phys. Rev. Lett. **95**, 146802 (2005).

[54] X.-L. Qi and S.-C. Zhang, Rev. Mod. Phys. **83**, 1057 (2011).

[55] F. D. M. Haldane, Physics Letters A **93**, 464 (1983).

[56] F. D. M. Haldane, Phys. Rev. Lett. **50**, 1153 (1983).

[57] Y. Fuji, F. Pollmann, and M. Oshikawa, Phys. Rev. Lett. **114**, 177204 (2015).

[58] A. Mesaros and Y. Ran, Phys. Rev. B **87**, 155115 (2013).

[59] Y.-M. Lu and A. Vishwanath, Phys. Rev. B **93**, 155121 (2016).

[60] K. v. Klitzing, G. Dorda, and M. Pepper, Phys. Rev. Lett. **45**, 494 (1980).

[61] S. M. Girvin and A. H. MacDonald, Phys. Rev. Lett. **58**, 1252 (1987).

[62] N. Read, Phys. Rev. Lett. **62**, 86 (1989).

[63] S. C. Zhang, T. H. Hansson, and S. Kivelson, Phys. Rev. Lett. **62**, 82 (1989).

[64] S. C. Zhang, International Journal of Modern Physics B **06**, 25 (1992).

[65] E. Witten, Communications in Mathematical Physics **121**, 351 (1989).

[66] X.-G. Wen, *Quantum Field Theory of Many-Body Systems* (Oxford University Press, Oxford, 2004).

[67] W. Chen, K. Hida, and B. C. Sanctuary, Phys. Rev. B **67**, 104401 (2003).

[68] I. Affleck, T. Kennedy, E. H. Lieb, and H. Tasaki, Phys. Rev. Lett. **59**, 799 (1987).

[69] I. Affleck, T. Kennedy, E. H. Lieb, and H. Tasaki, Communications in Mathematical Physics **115**, 477 (1988).

[70] M. Fannes, B. Nachtergaele, and R. F. Werner, Communications in Mathematical Physics **144**, 443 (1992).

[71] D. Perez-Garcia, F. Verstraete, M. M. Wolf, and J. I. Cirac, Quant. Inf. Comput. **7**, 401 (2007).

[72] X. Chen, Z.-C. Gu, and X.-G. Wen, Phys. Rev. B **83**, 035107 (2011).

[73] X. Chen, Z.-C. Gu, and X.-G. Wen, Phys. Rev. B **84**, 235128 (2011).

[74] D. Pérez-García, M. M. Wolf, M. Sanz, F. Verstraete, and J. I. Cirac, Phys. Rev. Lett. **100**, 167202 (2008).

[75] L. Fidkowski and A. Kitaev, Phys. Rev. B **83**, 075103 (2011).

[76] F. Pollmann, A. M. Turner, E. Berg, and M. Oshikawa, Phys. Rev. B **81**, 064439 (2010).

[77] F. Pollmann, E. Berg, A. M. Turner, and M. Oshikawa, Phys. Rev. B **85**, 075125 (2012).

[78] T. Morimoto, H. Ueda, T. Momoi, and A. Furusaki, Phys. Rev. B **90**, 235111 (2014).

[79] X. Chen, Z.-C. Gu, Z.-X. Liu, and X.-G. Wen, Science **338**, 1604 (2012).

[80] A. Vishwanath and T. Senthil, Phys. Rev. X **3**, 011016 (2013).

[81] L. Fidkowski, X. Chen, and A. Vishwanath, Phys. Rev. X **3**, 041016 (2013).

[82] A. Kapustin, arXiv: 1403.1467 (2014).

[83] A. Kapustin, arXiv: 1404.6659 (2014).

[84] N. Bultinck, D. J. Williamson, J. Haegeman, and F. Verstraete, arXiv: 1610.07849 (2016).

[85] A. Kapustin, A. Turzillo, and M. You, arXiv: 1610.10075 (2016).

[86] T. Senthil and M. Levin, Phys. Rev. Lett. **110**, 046801 (2013).

[87] Y.-M. Lu and A. Vishwanath, Phys. Rev. B **86**, 125119 (2012).

[88] S. Furukawa and M. Ueda, Phys. Rev. Lett. **111**, 090401 (2013).

[89] Y.-H. Wu and J. K. Jain, Phys. Rev. B **87**, 245123 (2013).

[90] N. Regnault and T. Senthil, Phys. Rev. B **88**, 161106 (2013).

[91] Y.-C. He, S. Bhattacharjee, R. Moessner, and F. Pollmann, Phys. Rev. Lett. **115**, 116803 (2015).

[92] A. Sterdyniak, N. R. Cooper, and N. Regnault, Phys. Rev. Lett. **115**, 116802 (2015).

[93] T.-S. Zeng, W. Zhu, and D. N. Sheng, Phys. Rev. B **93**, 195121 (2016).

[94] Y. Fuji, Y.-C. He, S. Bhattacharjee, and F. Pollmann, Phys. Rev. B **93**, 195143 (2016).

[95] A. Y. Kitaev, Physics-Uspekhi **44**, 131 (2001).

[96] N. Read and D. Green, Phys. Rev. B **61**, 10267 (2000).

[97] A. P. Schnyder, S. Ryu, A. Furusaki, and A. W. W. Ludwig, Phys. Rev. B **78**, 195125 (2008).

[98] S. Ryu, A. P. Schnyder, A. Furusaki, and A. W. W. Ludwig, New Journal of Physics **12**, 065010 (2010).

[99] A. Kitaev, AIP Conference Proceedings **1134**, 22 (2009).

[100] L. Fu, Phys. Rev. Lett. **106**, 106802 (2011).

[101] T. Morimoto and A. Furusaki, Phys. Rev. B **88**, 125129 (2013).

[102] K. Shiozaki and M. Sato, Phys. Rev. B **90**, 165114 (2014).

[103] Y.-M. Lu and D.-H. Lee, arXiv: 1403.5558 (2014).

[104] K. Shiozaki, M. Sato, and K. Gomi, Phys. Rev. B **93**, 195413 (2016).

[105] L. Fidkowski and A. Kitaev, Phys. Rev. B **81**, 134509 (2010).

[106] H. Yao and S. Ryu, Phys. Rev. B **88**, 064507 (2013).

[107] Z.-C. Gu and M. Levin, Phys. Rev. B **89**, 201113 (2014).

[108] C. Wang and T. Senthil, Phys. Rev. B **89**, 195124 (2014).

[109] H. Isobe and L. Fu, Phys. Rev. B **92**, 081304 (2015).

[110] T. Yoshida and A. Furusaki, Phys. Rev. B **92**, 085114 (2015).

[111] T. Morimoto, A. Furusaki, and C. Mudry, Phys. Rev. B **92**, 125104 (2015).

[112] A. Kapustin, R. Thorngren, A. Turzillo, and Z. Wang, Journal of High Energy Physics **2015**, 52 (2015).

[113] A. Bernevig and T. Neupert, arXiv: 1506.05805 (2015).

[114] C. Wang, A. C. Potter, and T. Senthil, Science **343**, 629 (2014).

[115] Z.-C. Gu and X.-G. Wen, Phys. Rev. B **90**, 115141 (2014).

[116] C. Wang, C.-H. Lin, and Z.-C. Gu, arXiv: 1610.08478 (2016).

[117] M. H. Anderson, J. R. Ensher, M. R. Matthews, C. E. Wieman, and E. A. Cornell, Science **269**, 198 (1995).

[118] K. B. Davis, M. O. Mewes, M. R. Andrews, N. J. van Druten, D. S. Durfee, D. M. Kurn, and W. Ketterle, Phys. Rev. Lett. **75**, 3969 (1995).

[119] D. S. Jin, J. R. Ensher, M. R. Matthews, C. E. Wieman, and E. A. Cornell, Phys. Rev. Lett. **77**, 420 (1996).

[120] I. Bloch, J. Dalibard, and W. Zwerger, Rev. Mod. Phys. **80**, 885 (2008).

[121] D. Jaksch, C. Bruder, J. I. Cirac, C. W. Gardiner, and P. Zoller, Phys. Rev. Lett. **81**, 3108 (1998).

[122] J. Dalibard, F. Gerbier, G. Juzeliūnas, and P. Öhberg, Rev. Mod. Phys. **83**, 1523 (2011).

[123] Y.-J. Lin, R. L. Compton, K. Jimnez-Garca, J. V. Porto1, and I. B. Spielman, Nature **462**, 628 (2009).

[124] Y.-J. Lin, R. L. Compton, K. Jimnez-Garca, W. D. Phillips, J. V. Porto, and I. B. Spielman, Nat. Phys. **7**, 531 (2011).

[125] Y.-J. Lin, K. Jimnez-Garca, and I. B. Spielman, Nature **471**, 83 (2011).

[126] L. W. Cheuk, A. T. Sommer, Z. Hadzibabic, T. Yefsah, W. S. Bakr, and M. W. Zwierlein, Phys. Rev. Lett. **109**, 095302 (2012).

[127] P. Wang, Z.-Q. Yu, Z. Fu, J. Miao, L. Huang, S. Chai, H. Zhai, and J. Zhang, Phys. Rev. Lett. **109**, 095301 (2012).

[128] M. Aidelsburger, M. Atala, S. Nascimbène, S. Trotzky, Y.-A. Chen, and I. Bloch, Phys. Rev. Lett. **107**, 255301 (2011).

[129] M. Aidelsburger, M. Atala, M. Lohse, J. T. Barreiro, B. Paredes, and I. Bloch, Phys. Rev. Lett. **111**, 185301 (2013).

[130] H. Miyake, G. A. Siviloglou, C. J. Kennedy, W. C. Burton, and W. Ketterle, Phys. Rev. Lett. **111**, 185302 (2013).

[131] M. Aidelsburger, M. Lohse, C. Schweizer, M. Atala, J. T. Barreiro, S. Nascimbène, N. R. Cooper, I. Bloch, and N. Goldman, Nat. Phys. **11**, 162 (2014).

[132] K. Jiménez-García, L. J. LeBlanc, R. A. Williams, M. C. Beeler, A. R. Perry, and I. B. Spielman, Phys. Rev. Lett. **108**, 225303 (2012).

[133] J. Struck, C. Ölschläger, M. Weinberg, P. Hauke, J. Simonet, A. Eckardt, M. Lewenstein, K. Sengstock, and P. Windpassinger, Phys. Rev. Lett. **108**, 225304 (2012).

[134] G. Jotzu, M. Messer, R. Desbuquois, M. Lebrat, T. Uehlinger, D. Greif, and T. Esslinger, Nature **515**, 237 (2014).

[135] A. Celi, P. Massignan, J. Ruseckas, N. Goldman, I. B. Spielman, G. Juzeliūnas, and M. Lewenstein, Phys. Rev. Lett. **112**, 043001 (2014).

[136] M. Mancini, G. Pagano, G. Cappellini, L. Livi, M. Rider, J. Catani, C. Sias, P. Zoller, M. Inguscio, M. Dalmonte, et al., Science **349**, 1510 (2015).

[137] B. K. Stuhl, H.-I. Lu, L. M. Aycock, D. Genkina, and I. B. Spielman, Science **349**, 1514 (2015).

[138] M. Leder, C. Grossert, L. Sitta, M. Genske, A. Rosch, and M. Weitz, Nat. Commun. **7**, 13112 (2016).

[139] S. Nakajima, T. Tomita, S. Taie, T. Ichinose, H. Ozawa, L. W. andMatthias Troyer, and Y. Takahashi, Nat. Phys. **12**, 296 (2016).

[140] M. Lohse, C. Schweizer, O. Zilberberg, M. Aidelsburger, and I. Bloch, Nat. Phys. **12**, 350 (2016).

[141] C. Schweizer, M. Lohse, R. Citro, and I. Bloch, Phys. Rev. Lett. **117**, 170405 (2016).

[142] Y. Takasu, K. Maki, K. Komori, T. Takano, K. Honda, M. Kumakura, T. Yabuzaki, and Y. Takahashi, Phys. Rev. Lett. **91**, 040404 (2003).

[143] T. Fukuhara, Y. Takasu, M. Kumakura, and Y. Takahashi, Phys. Rev. Lett. **98**, 030401 (2007).

[144] Y. N. M. de Escobar, P. G. Mickelson, M. Yan, B. J. DeSalvo, S. B. Nagel, and T. C. Killian, Phys. Rev. Lett. **103**, 200402 (2009).

[145] S. Stellmer, M. K. Tey, B. Huang, R. Grimm, and F. Schreck, Phys. Rev. Lett. **103**, 200401 (2009).

[146] S. Kraft, F. Vogt, O. Appel, F. Riehle, and U. Sterr, Phys. Rev. Lett. **103**, 130401 (2009).

[147] Y. Takasu and Y. Takahashi, Journal of the Physical Society of Japan **78**, 012001 (2009).

[148] S. Stellmer, F. Schreck, and T. C. Killian, arXiv: 1307.0601 (2013).

[149] A. Derevianko and H. Katori, Rev. Mod. Phys. **83**, 331 (2011).

[150] A. V. Gorshkov, M. Hermele, V. Gurarie, C. Xu, P. S. Julienne, J. Ye, P. Zoller, E. Demler, M. D. Lukin, and A. M. Rey, Nat. Phys. **6**, 289 (2010).

[151] M. A. Cazalilla and A. M. Rey, Reports on Progress in Physics **77**, 124401 (2014).

[152] T. Fukuhara, S. Sugawa, M. Sugimoto, S. Taie, and Y. Takahashi, Phys. Rev. A **79**, 041604 (2009).

[153] S. Taie, Y. Takasu, S. Sugawa, R. Yamazaki, T. Tsujimoto, R. Murakami, and Y. Takahashi, Phys. Rev. Lett. **105**, 190401 (2010).

[154] S. Taie, R. Yamazaki, S. Sugawa, and Y. Takahashi, Nat. Phys. **8**, 825 (2012).

[155] C. Hofrichter, L. Riegger, F. Scazza, M. Höfer, D. R. Fernandes, I. Bloch, and S. Fölling, Phys. Rev. X **6**, 021030 (2016).

[156] G. Pagano, M. Mancini, G. Cappellini, P. Lombardi, F. Schäfer, H. Hu, X.-J. Liu, J. Catani, C. Sias, M. Inguscio, et al., Nat. Phys. **10**, 198 (2014).

[157] G. Cappellini, M. Mancini, G. Pagano, P. Lombardi, L. Livi, M. Siciliani de Cumis, P. Cancio, M. Pizzocaro, D. Calonico, F. Levi, et al., Phys. Rev. Lett. **113**, 120402 (2014).

[158] F. Scazza, C. Hofrichter, M. Höfer, P. C. D. Groot, I. Bloch, and S. Fölling, Nat. Phys. **10**, 779 (2014).

[159] L. F. Livi, G. Cappellini, M. Diem, L. Franchi, C. Clivati, M. Frittelli, F. Levi, D. Calonico, J. Catani, M. Inguscio, et al., Phys. Rev. Lett. **117**, 220401 (2016).

[160] P. G. Mickelson, Y. N. Martinez de Escobar, M. Yan, B. J. DeSalvo, and T. C. Killian, Phys. Rev. A **81**, 051601 (2010).

[161] S. Stellmer, R. Grimm, and F. Schreck, Phys. Rev. A **87**, 013611 (2013).

[162] B. J. DeSalvo, M. Yan, P. G. Mickelson, Y. N. Martinez de Escobar, and T. C. Killian, Phys. Rev. Lett. **105**, 030402 (2010).

[163] X. Zhang, M. Bishof, S. L. Bromley, C. V. Kraus, M. S. Safronova, P. Zoller, A. M. Rey, and J. Ye, Science **345**, 1467 (2014).

[164] C. Chin, R. Grimm, P. Julienne, and E. Tiesinga, Rev. Mod. Phys. **82**, 1225 (2010).

[165] K. Enomoto, K. Kasa, M. Kitagawa, and Y. Takahashi, Phys. Rev. Lett. **101**, 203201 (2008).

[166] S. Kato, S. Sugawa, K. Shibata, R. Yamamoto, and Y. Takahashi, Phys. Rev. Lett. **110**, 173201 (2013).

[167] S. Taie, S. Watanabe, T. Ichinose, and Y. Takahashi, Phys. Rev. Lett. **116**, 043202 (2016).

[168] R. Zhang, Y. Cheng, H. Zhai, and P. Zhang, Phys. Rev. Lett. **115**, 135301 (2015).

[169] M. Höfer, L. Riegger, F. Scazza, C. Hofrichter, D. R. Fernandes, M. M. Parish, J. Levinsen, I. Bloch, and S. Fölling, Phys. Rev. Lett. **115**, 265302 (2015).

[170] G. Pagano, M. Mancini, G. Cappellini, L. Livi, C. Sias, J. Catani, M. Inguscio, and L. Fallani, Phys. Rev. Lett. **115**, 265301 (2015).

[171] L. D. Landau and E. M. Lifshitz, *Quantum Mechanics (Non-relativistic Theory)* (Butterworth-Heinemann, Oxford, 1981), 3rd ed.

[172] A. Kamenev, *Field Theory of Non-equilibrium Systems* (Cambridge University Press, Cambridge, 2011).

[173] Z. Ratiani and A. Mitra, Phys. Rev. B **79**, 245111 (2009).

[174] A. J. Millis and P. A. Lee, Phys. Rev. B **35**, 3394 (1987).

[175] S. Burdin, A. Georges, and D. R. Grempel, Phys. Rev. Lett. **85**, 1048 (2000).

[176] B. Paredes, C. Tejedor, and J. I. Cirac, Phys. Rev. A **71**, 063608 (2005).

[177] M. Foss-Feig, M. Hermele, and A. M. Rey, Phys. Rev. A **81**, 051603 (2010).

[178] M. Foss-Feig, M. Hermele, V. Gurarie, and A. M. Rey, Phys. Rev. A **82**, 053624 (2010).

[179] J. Bauer, C. Salomon, and E. Demler, Phys. Rev. Lett. **111**, 215304 (2013).

[180] Y. Nishida, Phys. Rev. Lett. **111**, 135301 (2013).

[181] M. Nakagawa and N. Kawakami, Phys. Rev. Lett. **115**, 165303 (2015).

[182] R. Zhang, D. Zhang, Y. Cheng, W. Chen, P. Zhang, and H. Zhai, Phys. Rev. A **93**, 043601 (2016).

[183] D.-H. Lee and J. Toner, Phys. Rev. Lett. **69**, 3378 (1992).

[184] A. Furusaki and N. Nagaosa, Phys. Rev. Lett. **72**, 892 (1994).

[185] H. Tsunetsugu, M. Sigrist, and K. Ueda, Rev. Mod. Phys. **69**, 809 (1997).

[186] A. M. Tsvelik, Phys. Rev. Lett. **72**, 1048 (1994).

[187] S. Fujimoto and N. Kawakami, Journal of the Physical Society of Japan **63**, 4322 (1994).

[188] S. Fujimoto and N. Kawakami, Journal of the Physical Society of Japan **66**, 2157 (1997).

[189] O. Zachar, S. A. Kivelson, and V. J. Emery, Phys. Rev. Lett. **77**, 1342 (1996).

[190] K. Le Hur, Phys. Rev. B **58**, 10261 (1998).

[191] O. Zachar, Phys. Rev. B **63**, 205104 (2001).

[192] D. J. Garcia, K. Hallberg, B. Alascio, and M. Avignon, Phys. Rev. Lett. **93**, 177204 (2004).

[193] E. Pivovarov and Q. Si, Phys. Rev. B **69**, 115104 (2004).

[194] R. M. Fye and D. J. Scalapino, Phys. Rev. Lett. **65**, 3177 (1990).

[195] H. Tsunetsugu, Y. Hatsugai, K. Ueda, and M. Sigrist, Phys. Rev. B **46**, 3175 (1992).

[196] C. C. Yu and S. R. White, Phys. Rev. Lett. **71**, 3866 (1993).

[197] N. Shibata, C. Ishii, and K. Ueda, Phys. Rev. B **51**, 3626 (1995).

[198] N. Shibata, K. Ueda, T. Nishino, and C. Ishii, Phys. Rev. B **54**, 13495 (1996).

[199] N. Shibata, T. Nishino, K. Ueda, and C. Ishii, Phys. Rev. B **53**, R8828 (1996).

[200] N. Shibata, A. Tsvelik, and K. Ueda, Phys. Rev. B **56**, 330 (1997).

[201] R. Peters and N. Kawakami, Phys. Rev. B **86**, 165107 (2012).

[202] J. Silva-Valencia and A. M. C. Souza, The European Physical Journal B **85**, 5 (2012).

[203] T. Giamarchi, *Quantum Physics in One Dimension* (Oxford University Press, Oxford, 2003).

[204] E. Fradkin, *Field Theories of Condensed Matter Physics* (Cambridge University Press, Cambridge, 2013), 2nd ed.

[205] S. P. Strong and A. J. Millis, Phys. Rev. Lett. **69**, 2419 (1992).

[206] S. P. Strong and A. J. Millis, Phys. Rev. B **50**, 9911 (1994).

[207] D. G. Shelton, A. A. Nersesyan, and A. M. Tsvelik, Phys. Rev. B **53**, 8521 (1996).

[208] P. Lecheminant and E. Orignac, Phys. Rev. B **65**, 174406 (2002).

[209] V. Alexandrov and P. Coleman, Phys. Rev. B **90**, 115147 (2014).

[210] A. M. Lobos, A. O. Dobry, and V. Galitski, Phys. Rev. X **5**, 021017 (2015).

[211] A. Mezio, A. M. Lobos, A. O. Dobry, and C. J. Gazza, Phys. Rev. B **92**, 205128 (2015).

[212] I. Hagymási and O. Legeza, Phys. Rev. B **93**, 165104 (2016).

[213] E. Berg, E. G. Dalla Torre, T. Giamarchi, and E. Altman, Phys. Rev. B **77**, 245119 (2008).

[214] Y. Fuji, Phys. Rev. B **93**, 104425 (2016).

[215] I. Maruyama and Y. Hatsugai, Journal of Physics: Conference Series **150**, 042116 (2009).

[216] F. Anfuso and A. Rosch, Phys. Rev. B **75**, 144420 (2007).

[217] S. Moudgalya and F. Pollmann, Phys. Rev. B **91**, 155128 (2015).

[218] I. Hagymási, J. Sólyom, and O. Legeza, Phys. Rev. B **92**, 035108 (2015).

[219] H. L. Nourse, I. P. McCulloch, C. Janani, and B. J. Powell, Phys. Rev. B **94**, 214418 (2016).

[220] T. L. Hughes, E. Prodan, and B. A. Bernevig, Phys. Rev. B **83**, 245132 (2011).

[221] A. M. Turner, F. Pollmann, and E. Berg, Phys. Rev. B **83**, 075102 (2011).

[222] Y.-Z. You and C. Xu, Phys. Rev. B **90**, 245120 (2014).

[223] H. Shapourian, K. Shiozaki, and S. Ryu, arXiv: 1607.03896 (2016).

[224] K. Shiozaki, H. Shapourian, and S. Ryu, arXiv: 1609.05970 (2016).

[225] M. Hagiwara, K. Katsumata, I. Affleck, B. I. Halperin, and J. P. Renard, Phys. Rev. Lett. **65**, 3181 (1990).

[226] S. H. Glarum, S. Geschwind, K. M. Lee, M. L. Kaplan, and J. Michel, Phys. Rev. Lett. **67**, 1614 (1991).

[227] N. Goldman, G. Jotzu, M. Messer, F. Görg, R. Desbuquois, and T. Esslinger, Phys. Rev. A **94**, 043611 (2016).

[228] M. F. Parsons, A. Mazurenko, C. S. Chiu, G. Ji, D. Greif, and M. Greiner, Science **353**, 1253 (2016).

[229] M. Boll, T. A. Hilker, G. Salomon, A. Omran, J. Nespolo, L. Pollet, I. Bloch, and C. Gross, Science **353**, 1257 (2016).

[230] L. W. Cheuk, M. A. Nichols, K. R. Lawrence, M. Okan, H. Zhang, E. Khatami, N. Trivedi, T. Paiva, M. Rigol, and M. W. Zwierlein, Science **353**, 1260 (2016).

[231] D. J. Thouless, Phys. Rev. B **27**, 6083 (1983).

[232] D. J. Thouless, M. Kohmoto, M. P. Nightingale, and M. den Nijs, Phys. Rev. Lett. **49**, 405 (1982).

[233] M. Kohmoto, Annals of Physics **160**, 343 (1985).

[234] M. J. Rice and E. J. Mele, Phys. Rev. Lett. **49**, 1455 (1982).

[235] D. Xiao, M.-C. Chang, and Q. Niu, Rev. Mod. Phys. **82**, 1959 (2010).

[236] R. Shindou, Journal of the Physical Society of Japan **74**, 1214 (2005).

[237] E. Berg, M. Levin, and E. Altman, Phys. Rev. Lett. **106**, 110405 (2011).

[238] J.-T. A. Chiang and Q. Niu, Phys. Rev. A **57**, R2278 (1998).

[239] L. Wang, M. Troyer, and X. Dai, Phys. Rev. Lett. **111**, 026802 (2013).

[240] P. Marra, R. Citro, and C. Ortix, Phys. Rev. B **91**, 125411 (2015).

[241] R. Wei and E. J. Mueller, Phys. Rev. A **92**, 013609 (2015).

[242] R. Tao and D. J. Thouless, Phys. Rev. B **28**, 1142 (1983).

[243] A. Seidel, H. Fu, D.-H. Lee, J. M. Leinaas, and J. Moore, Phys. Rev. Lett. **95**, 266405 (2005).

[244] E. J. Bergholtz and A. Karlhede, Phys. Rev. Lett. **94**, 026802 (2005).

[245] E. J. Bergholtz and A. Karlhede, Phys. Rev. B **77**, 155308 (2008).

[246] Z.-C. Gu and X.-G. Wen, Phys. Rev. B **80**, 155131 (2009).

[247] D. Yoshioka, Phys. Rev. B **29**, 6833 (1984).

[248] F. D. M. Haldane, Phys. Rev. Lett. **55**, 2095 (1985).

[249] R. B. Laughlin, Phys. Rev. B **23**, 5632 (1981).

[250] R. Tao and Y.-S. Wu, Phys. Rev. B **30**, 1097 (1984).

[251] Q. Niu and D. J. Thouless, Journal of Physics A: Mathematical and General **17**, 2453 (1984).

[252] Q. Niu, D. J. Thouless, and Y.-S. Wu, Phys. Rev. B **31**, 3372 (1985).

[253] M. Nakamura, E. J. Bergholtz, and J. Suorsa, Phys. Rev. B **81**, 165102 (2010).

[254] Z.-Y. Wang, S. Takayoshi, and M. Nakamura, Phys. Rev. B **86**, 155104 (2012).

[255] P. Rotondo, L. G. Molinari, P. Ratti, and M. Gherardi, Phys. Rev. Lett. **116**, 256803 (2016).

[256] D. Meidan, T. Micklitz, and P. W. Brouwer, Phys. Rev. B **84**, 075325 (2011).

[257] F. Grusdt and M. Höning, Phys. Rev. A **90**, 053623 (2014).

[258] T.-S. Zeng, C. Wang, and H. Zhai, Phys. Rev. Lett. **115**, 095302 (2015).

[259] T.-S. Zeng, W. Zhu, and D. N. Sheng, Phys. Rev. B **94**, 235139 (2016).

[260] L. Taddia, E. Cornfeld, D. Rossini, L. Mazza, E. Sela, and R. Fazio, arXiv: 1607.07842 (2016).

[261] S. Barbarino, L. Taddia, D. Rossini, L. Mazza, and R. Fazio, Nat. Commun. **6**, 8134 (2015).

[262] T. Y. Saito and S. Furukawa, arXiv: 1612.00233 (2016).

[263] A. Auerbach and D. P. Arovas, Phys. Rev. Lett. **61**, 617 (1988).

[264] M. den Nijs and K. Rommelse, Phys. Rev. B **40**, 4709 (1989).

[265] T. Kennedy and H. Tasaki, Phys. Rev. B **45**, 304 (1992).

[266] N. R. Cooper, Phys. Rev. Lett. **106**, 175301 (2011).

[267] E. Wikberg, E. J. Bergholtz, and A. Karlhede, Journal of Statistical Mechanics: Theory and Experiment **2009**, P07038 (2009).

[268] E. G. Dalla Torre, E. Berg, and E. Altman, Phys. Rev. Lett. **97**, 260401 (2006).

[269] M. P. Zaletel, R. S. K. Mong, and F. Pollmann, Journal of Statistical Mechanics: Theory and Experiment **2014**, P10007 (2014).

[270] E. Lieb, T. Schultz, and D. Mattis, Annals of Physics **16**, 407 (1961).

[271] I. Affleck and E. H. Lieb, Letters in Mathematical Physics **12**, 57 (1986).

[272] M. Oshikawa, M. Yamanaka, and I. Affleck, Phys. Rev. Lett. **78**, 1984 (1997).

[273] M. Nakamura and S. Todo, Phys. Rev. Lett. **89**, 077204 (2002).

[274] M. Nakamura and J. Voit, Phys. Rev. B **65**, 153110 (2002).

[275] M. Oshikawa, Phys. Rev. Lett. **84**, 1535 (2000).

[276] R. Resta, Phys. Rev. Lett. **80**, 1800 (1998).

[277] R. Resta and S. Sorella, Phys. Rev. Lett. **82**, 370 (1999).

[278] R. Resta, Rev. Mod. Phys. **66**, 899 (1994).

[279] R. D. King-Smith and D. Vanderbilt, Phys. Rev. B **47**, 1651 (1993).

[280] G. Ortiz and R. M. Martin, Phys. Rev. B **49**, 14202 (1994).

[281] X.-L. Qi, T. L. Hughes, and S.-C. Zhang, Phys. Rev. B **78**, 195424 (2008).

[282] J. Zak, Phys. Rev. Lett. **62**, 2747 (1989).

[283] Y. Hatsugai, Journal of the Physical Society of Japan **75**, 123601 (2006).

[284] T. Hirano, H. Katsura, and Y. Hatsugai, Phys. Rev. B **77**, 094431 (2008).

[285] T. Kariyado and Y. Hatsugai, Phys. Rev. B **88**, 245126 (2013).

[286] T. Kariyado and Y. Hatsugai, Phys. Rev. B **91**, 214410 (2015).

[287] W. P. Su, J. R. Schrieffer, and A. J. Heeger, Phys. Rev. Lett. **42**, 1698 (1979).

[288] S. R. White and D. A. Huse, Phys. Rev. B **48**, 3844 (1993).

[289] O. Golinelli, T. Jolicoeur, and R. Lacaze, Phys. Rev. B **50**, 3037 (1994).

[290] M. Kaburagi, T. Nishino, and T. Tonegawa, KOBEPACK, URL: http://quattro.phys.sci.kobe-u.ac.jp/Kobe_Pack/Kobe_Pack.html (1992).

[291] L. Fu and C. L. Kane, Phys. Rev. B **74**, 195312 (2006).

[292] Z.-X. Liu and X.-G. Wen, Phys. Rev. Lett. **110**, 067205 (2013).

[293] Z.-X. Liu, Z.-C. Gu, and X.-G. Wen, Phys. Rev. Lett. **113**, 267206 (2014).

Acknowledgment

First of all, I would like to express my sincerest gratitude to Prof. Norio Kawakami for his kind support, encouragement, and fruitful discussions during my graduate course. His broad knowledge of condensed matter physics and insightful suggestions have always inspired me, and I have learned a lot of things from him, which are not limited to physics. I am proud that I have studied quantum many-body physics (including the Kondo effect, the exact solution of which was discovered by him) under his supervision and guidance in this five years.

I would also like to thank Prof. Shunsuke Furukawa for the collaboration and valuable discussions. I have been impressed by his deep understanding of topological phases and other topics, and I have enjoyed many stimulating discussions with him. I would like to express my deep appreciation to him for spending his time to include the results of the collaboration in this thesis. Without his support, this thesis would not be completed.

Furthermore, I am grateful to Prof. Yoshiro Takahashi and members in the Quantum Optics Group at Kyoto university, especially Prof. Shuta Nakajima and Mr. Takafumi Tomita, for helpful discussions about ultracold atoms. All my studies included in this thesis have been motivated by the beautiful experiments performed by the Quantum Optics Group. Their comments and opinions as experimentalists have much benefited my work.

I would like to express my gratitude to current and former staff members in the Condensed Matter Theory Group, Prof. Satoshi Fujimoto, Prof. Ryusuke Ikeda, Prof. Youichi Yanase, Prof. Hiroaki Ikeda, Prof. Robert Peters, Prof. Masaki Tezuka, and Prof. Kazushi Aoyama, for helpful advices and comments in various opportunities. Also, I would like to thank my colleagues, Mr. Kyosuke Adachi, Mr. Akito Daido, Mr. Yuichiro Dan, Mr. Kazuki Hashimoto, Mr. Yohei Ibe, Mr. Koudai Iwahori, Dr. Masaru Sakaida, Dr. Atsuo Shitade, Mr. Shuntaro Sumita, Mr. Kazuaki Takasan, Ms. Rina Takashima, and Dr. Suguru Ueda. My daily life in the group has been comfortable and enjoyable thanks to the communications with them. Especially, I would like to thank Dr. Ken Shiozaki and Dr. Tsuneya Yoshida for many helpful discussions, from which I have learned useful knowledge of topological phases.

I would like to thank my friends, Mr. Takahiro Doi, Mr. Fuyuki Matsuda, Mr. Kenta Moriyama, Mr. Yasuharu Nakamura, Mr. Takuya Nomoto, Mr. Tokiro Numasawa, Mr. Hiroaki Sumiyoshi, and Mr. Shoichiro Tsutsui for countless enjoyable conversations in everyday life and also for discussions about physics. I have learned some parts of methods and knowledge used in this thesis through reading textbooks with them.

I would like to acknowledge the financial support from Japan Society for the Promotion of Science (JSPS) KAKENHI (Grant No. JP14J01328) and JSPS Research Fellowship for Young Scientists.

At last, I would like to express my deepest gratitude to my parents, Hitoshi Nakagawa and Tatsuko Nakagawa, for their continuous support and encouragement.